THIN-FILM NEURAL INTERFACES FOR BRAIN-COMPUTER INTERFACE AND ELECTRORETINOGRAPHY APPLICATIONS

by

Sanitta Thongpang

A dissertation submitted in partial fulfillment of

the requirements for the degree of

Doctor of Philosophy

(Biomedical Engineering)

at the

UNIVERSITY OF WISCONSIN–MADISON

2012

Date of final oral examination: 05/30/12

The dissertation is approved by the following members of the Final Oral Committee:

Justin C. Williams, Associate Professor, Biomedical Engineering
Walter F. Block, Professor, Biomedical Engineering
Karl A. Sillay, Assistant Professor, Affiliated Biomedical Engineering
Zhenqiang Ma, Professor, Electrical and Computer Engineering
John R. Hetling, Associate Professor, Bioengineering, University of Illinois at Chicago
M. Elizabeth Meyerand, Professor, Biomedical Engineering

To Erwin, his unconditional support and patience

ACKNOWLEDGMENTS

I would like to thank Prof. Justin Williams for giving me opportunity to work in his lab and for his valuable guidance that has lead me towards many unexpected and exciting research areas. I would like to also thank to my committee for their assistance and guidance over the years. Thanks to Prof. Lisa Krugner-Higby for her guidance and supports for all the works related to animal care and surgeries. Special thanks to my colleagues and friends Thomas Richner, Sarah Broadnick, Amelia Schendel, Kevin Cheng, Leo Walton, Andrew Woolley and all the students of the Williams lab for incredible collaborations and their encouragement. I would like to also thank Prof. John Hetling for introducing me to the ERG project and his guidance and intellectual input. Thanks also extended to the Hetling lab members for their incredible works using the ERG electrode arrays we developed together. Thanks to Prof. Daniel Moran and all his lab members, especially Jordan Williams and Jesse Wheeler for their collaboration in non-human primate micro-ECoG project.

I would like to express my gratitude to the Wisconsin Center for Applied Microelectronics staff for always being willing to help and make my experience in the cleanroom pleasurable and productive. Thanks to Prof. Ma and his students for their valuable input and great collaboration. I would like to also thank the staff at the Harlow and LAR for the animal care. I also appreciate the help and support from LOCI staff and for their outstanding imaging facilities. And finally, thanks to Prof. Ramin Pashaie and Ryan for the incredible LASER system, their support and their valuable input that

made the optogenetics project possible.

This project was funded in part by the Whitaker Foundation, the Defense Advanced Research Projects Association, the National Institute of Health, and the University of Wisconsin-Madison. I also would like to thank the Thai government for sponsoring my studies and research in the University of Wisconsin-Madison.

Finally, I would like to thank my family and friends for giving me unconditional support and perspective from outside the university. Without the continued support from all these people, this research would not be possible.

TABLE OF CONTENTS

Page

LIST OF TABLES vii

LIST OF FIGURES viii

Abstract xi

1 Neural Interfacing 1

1.1 Neural activity in central nervous system 3
1.2 Neural activity in human eye 10

2 Thin-film Neural Interface Devices Fabrication Methods and Techniques 18

2.1 Polyimide device fabrication 19
2.2 Parylene C devices 21
2.3 Connection scheme 24

3 Material Considerations for Thin-film Neural Interfaces 29

3.1 Property changes of polyimide and parylene C after accelerated soak test 30
3.2 Chronic implant studies in rats 34
3.3 Results 39
3.4 Conclusions 57

4 Chronic Implant Studies in Non-human Primate [1] 59

4.1 Electrode and chamber development 62
4.2 Pre-Implant Impedance Testing 67
4.3 Surgical techniques 67

4.4 Long-term signal recording 70
4.5 Biological Response 74
4.6 Conclusions 78

5 Micro-ECoG Electrode Optimization with Optogenetic Stimulation [1,2] 80

5.1 Methods and materials 83
5.2 Cranial window implantation 86
5.3 Electrophysiology 89
5.4 Results 92
5.5 Discussion and conclusions 103

6 Thin-film multi-electrode Electroretinography [1] 105

6.1 Planar CLEAr lens 107
6.2 Image-forming ERG electrode arrays 113
6.3 Conclusions 121

7 Conclusions and Future Directions 123

7.1 Future directions for micro-Electrocorticographic electrode array 126
7.2 Future directions for electroretinographic electrode 134
7.3 Conclusions 137

A Polymide electrode fabrication protocols 139
A.1 General Information 139
A.2 Materials 139
A.3 Fabrication Protocols 140

B Parylene electrode fabrication protocol 143
B.1 General Information 143
B.2 Materials 143
B.3 Fabrication Protocols 144

Page

C 3D CAD design of Phase II head chamber 148

D Immunohistochemical Protocols 149
D.1 Materials 149
D.2 Procedures 150

References 152

LIST OF TABLES

Table Page

3.1 Summary: Polyimide versus Parylene C Device 58

D.1 Table of Immunohistochemical Antibodies 149

LIST OF FIGURES

Figure Page

1.1 Brain structure and sensorimotor cortex 7
1.2 Human eye and retina structure 15

2.1 Polyimide device fabrication process 20
2.2 Parylene C deposition and fabrication process 23
2.3 Mechanically connecting of electrical connection: DIP interconnect socket 26
2.4 Zero Insertion Force (ZIF) connecter 27

3.1 Tensile strength and electrical impedance of the polyimide and parylene C devices correspond to accelerated soak test time . . . 32
3.2 Bilateral chronic implant in Sprauge-Dawley rats for polyimide and parylene device in comparison 35
3.3 Post-implant impedance spectra of M25 40
3.4 Weekly impedance data at 1 kHz post-implant 42
3.5 Power spectrum and evoked potential response of polyimide and parylene C devices comparison from an example rat 43
3.6 In-vivo Window Imaging for vasculature response: Bright-field images at day 4 46
3.7 In-vivo Window Imaging for vasculature response: Fluoresce Images at day 4 48
3.8 In-vivo Window Imaging for vasculature response: 6 and 10 day post implantation 50
3.9 In-vivo Window Imaging for vasculature response: 3 weeks implantation 51
3.10 General biological response: Bone growth 52
3.11 Astrocytes distribution from an example of 3 weeks chronic implant rat 54
3.12 Astrocytes distribution from an example of 6 and 12 weeks chronic implant rat 55

3.13 Microglia distribution from examples of 3, 6 and 12 week chronic implant rats 56

4.1 Monkey electrode layout 64
4.2 Head chamber development for Chronic Implant in non-human primate 65
4.3 Surgical and implant technique 68
4.4 Long-term chronic implant signal recording 71
4.5 Wavelet Spectrogram and evoked potential at week 2 73
4.6 Histological Results:Astrocyte activity 76
4.7 Histological Results:Microglia response 77

5.1 Mice electrode design and fabrication 84
5.2 Cranial window implantation 89
5.3 Baseline recording and power spectrum of different electrode size array 93
5.4 Broad surface stimulation on different electrode size with LED . 94
5.5 Focal stimulation on brain surface with LED source 97
5.6 Focal stimulation on brain surface with laser source through optical fiber 98
5.7 Focal stimulation at various depth with optical fiber coupled blue laser 99
5.8 Control experiments 101
5.9 Post mortem control 102

6.1 Custom-made PMMA meERG lens 108
6.2 Custom-made PMMA lens human CLEAr lens and example signals 112
6.3 Image-forming ERG lens design and Matlab algorithm for electrode site interpolation 115
6.4 PDMS mold making for electrode bonding process 117
6.5 Rigid clear contact lens meERG Assembly 118
6.6 ERG signal recording and visual test 120

7.1 All-polymer micro-ECoG 129
7.2 Integrated Optogenetic micro-ECoG 132
7.3 Scleral Lens ERG 137

C.1 3D CAD design of phase II head chamber 148

Chapter	Adapted / taken from papers
Chapter 3	Manuscript in preparation
Chapter 4	"A micro- electrocorticography platform and deployment strategies for chronic bci applications", S. Thongpang, T. J. Richner, S. K. Brodnick, A. Schendel, J. Kim, J. A. Wilson, J. Hippensteel, L. Krugner-Higby, D. Moran, A. S. Ahmed, D. Neimann, K. Sillay, and J. C. Williams. *Clin EEG Neurosci*, 42(4):259 - 65, Oct 2011. " Minimal invasive chronic micro-electrocorticography for Brain-Computer Interface", Sanitta Thongpang, Thomas Richner, Sarah Brodnick, Kevin Cheng, Jordan Williams, Amy Schendel, Leo Walton, Danial Moran, Lisa Krugner-Higby and Justin C Williams, in preparation for *Journal of Neural Engineering* submission.
Chapter 5	"An optogenetic micro-ECoG neural interface" , Thomas Richner, Sanitta Thongpang, Sarah Brodnick, Ryan Falk, Amelia Schendel, Lisa Krugner-Higby, Ramin Pashaie, and Justin C Williams., submitting to *Journal of Neuroscience*. "Micro-electrocorticography Electrode Site Size Optimization with Optogenetic Stimulation" , Sanitta Thongpang, Thomas Richner, Sarah Brodnick, Ryan Falk, Amelia Schendel, Lisa Krugner-Higby, Ramin Pashaie and Justin C Williams., in preparation for *Journal of Neural Engineering* submission.
Chapter 6	"A novel multi-electrode Electroretinographic contact lens" , Sanitta Thongpang, Ashley Selner, Tomas Ban, Thomas Richner, John Hetling and Justin C Williams., in preparation for *Journal of Neural Engineering* submission.

ABSTRACT

The brain, and more precisely the central nervous system (CNS), is an extremely complex organ responsible for controlling essential sensorimotor functions of the human body. These functions rely on nerves running all-throughout the organism, transporting the sensory information from the body towards the CNS and the motor information from the CNS to the muscles. However, when severed, these functions can be durably lost, provoking paralysis and significant loss of quality of life. Neuroprosthesis is a promising approach to allow the patient to regain some of the quality of life lost through the control of a computer directly from measuring brain activity. Unfortunately, current methods are either too invasive, risk a decrease of performance over time and require extreme precision to place (i.e. single-unit electrode) or non-invasive but imprecise and limited (e.g. electroencephalogram).

Electrocorticogram interfaces (ECoG and micro-ECoG) have been developed to measure brain activity as close as possible to the neurons while minimizing invasivity and long-term effects. These are placed on between the cortex and the cranium and allow good improvements in signal quality and spatial resolution. Here, I present the improved electrode designs and fabrication methods for reliable micro-ECoG electrode arrays using flexible insulating materials such as polyimide and parylene C. Furthermore, we characterize the long-term effect of chronic implantation of the device both

on the electrical and material properties as well as the biological response of the brain of the micro-ECoG arrays. In addition, leveraging recent developments in optogenetics, two-way neural interface devices were developed. By integrating these methods with cranial window imaging techniques, I demonstrated that very powerful tools for optimizing micro-ECoG electrode arrays, as well as answering fundamental biological question on the function of the brain, can be developed. Finally, the flexible thin-film bio-MEMS fabrication methods demonstrated were readily expanded to many other applications such as electroretinogram (ERG) recording.

1 NEURAL INTERFACING

The Central Nervous System (CNS) is a vast and complex organ that centralizes, analyzes and controls a multitude of stimuli, related to sensing, muscle motion, emotions and thoughts. This organ is composed of billions of neurons, each able to create a multitude of connections with neighboring neurons and transmit information by changing their electrical state. The electrical nature of these stimuli generates measurable electrical fields which can provide snapshots of the state of the brain. Measuring these signals has been a goal for developing research (and now also commercial) brain-interfacing tools, such as the well known electroencephalogram (EEG) which can record the brain activity along the scalp [Jasper and Kershman (1946)], [Schalk et al. (2000)]. However, as the electrical fields produced are very small, decay rapidly and contain important spatial information, more accurate interfacing devices have been developed such as the electrocorticogram (ECoG) which can record brain activity directly from cerebral cortex [Leuthardt et al. (2004)]. More recently, this approach has been improved using flexible thin-film micro-fabrication techniques to create a less invasive high-resolution electrode array called micro-ECoG [Stieglitz and Meyer (1999)], [Hollenberg et al. (2006)], [Kim et al. (2007)].

Micro-ECoG technology is still in its infancy, and while significant improvements have been accomplished in the fabrication of flexible electrodes for this application, a lot remains to be understood about the material interaction with the brain, particularly in the context of chronic implantation. In this document, I will present the work that has been accomplished to

bring insight into the effect of long-term implantation both on the device itself and on the response of the brain. First, I will present in more detail the function of the brain focusing particularly on the parts of the CNS that are most relevant to sensorimotor functions. Additionally, the approaches that have been developed to interface and measure the electrical stimuli at these locations for creating Brain-Computer Interfaces (BCI) will be reviewed. Chapter 2 will present the fabrication methods that have been used, ameliorated or developed for the creation of thin-film micro-ECoG devices used in the work presented here. Chapter 3 describes preliminary characterization studies, aiming at better understanding the effect of chronic implantation on the device performance and the importance of specific materials, particularly polyimide and parylene C. Chapter 4 describes results of chronic implantation studies on primates and delves into the reaction of the brain to long-term exposure to foreign materials. Although optimal for implanting into the skull, the fabrication techniques developed here allow the measure of other types of electrical signals, such as those produced by the retina. In Chapter 5, I demonstrate how optogenetics can be applied for micro-ECoG electrode optimization. In Chapter 6, I present a novel multi-electrode electroretinogram (meERG), that was made possible by leveraging the flexible thin-film fabrication methods developed for the micro-ECoG. Finally, I will identify in Chapter 7 areas that require further investigation and/or development and propose experiments in these directions.

1.1 Neural activity in central nervous system

The CNS receives information from sensory nerve extremities and in return controls the function of muscles throughout the body. The nerves conducting this information are made of bundles of tightly packed axons, each leading to a different neuron in the peripheral nervous system (PNS) or the CNS. In case of traumatic injury, however, the axons in motor pathway hardly regenerate and partial or total paralysis can occur. One of the leading applications for BCI devices is the development of neuroprosthetics to allow direct connection of sensory and motor brain function to a computer. Most of the neurons of the CNS are located in the cerebral cortex, a thin convoluted neural layer at the surface of the forebrain [Nicholls et al. (2001)], making them readily accessible by surface interfacing devices. The cerebral cortex has specialized areas that control sensory, motor function, visual, auditory, language, comprehension, speech, memory, awareness and consciousness (Figure 1.1A). It is the electrical characteristics of the central nervous system and its connectivity that interests the researchers and allows us to design the innovative devices and methods to interface with this complex system. Neural connections and activity in central nervous system will be described briefly in this section. In addition, different neural interfacing technologies according to level of invasiveness will be presented.

Central nervous system structure

The CNS is composed of billions neurons, each able to create more than ten thousand synaptic connections to other neighboring neurons via elongated

protrusions called dendrites and able to carry information over long distances to other regions of the brain and body via a single long fiber called "axon". Information is sent to the connecting neurons via the dendrites and axons by the depolarization of the trans-membrane potential creating brief electrical pulses termed "action potentials". The neuron integrates action potentials received from all upstream neurons and its axon and conditionally triggers an new action potential, participating in the processing and relay of information.

Together with PNS, the CNS can control our behavior via complex connections. To be specific for this context, I will only emphasize parts of the cerebral cortex in the brain which neural interface devices for BCI applications are targeting. The cerebral cortex is the outermost layer of cerebrum in the mammalian brain and it plays important roles in motor function, perception, attention, thought, language and memory. Each of these functions are segregated in different areas that are the primary motor cortex, the primary sensory cortex, the primary auditory cortex, the sensory associated cortex, and the visual cortex and prefrontal cortex (Figure 1.1A). In humans, the cerebral cortex is also called the "gray matter" and is approximately 2 to 4 mm thick. The neurons in the gray matter are connected to different parts of cerebral cortex and other parts of the CNS by myelinated axons that form the white matter. The cerebral cortex is constituted of multiple highly inter-connected layers containing different types of neurons which are grouped into six main layers arranged from outermost (pial surface) and innermost (white matter) layers. Layer I, II and III contain a high number of scattered pyramidal cells, small pyramidal cells and medium pyramidal cells that are the main target of interhemispheric cortical afferents as the

brain has two hemispheres that control the contralateral (opposite side) sensory and motor functions. Layer III in particular is the main source of cortical efferents. Layer IV contains stellate and pyramidal neurons, and is the main target of thalamocortical afferents from thalamus as well as intra-hemispheric corticocortical afferents. However, the main population of pyramidal cells (Betz cells) in the primary motor cortex and the principal source of subcortical efferents lie in layer V. Layer VI consists of few large pyramidal neurons and many small spindle-like pyramidal and multiform neurons. This layer sends efferent fibers to the thalamus, establishing a reciprocal interconnection between the cortex and the thalamus. These cortical micro-connections form cortical columns and minicolumns, the latter of which have been proposed to be the basic functional units of cortex [Mountcastle (1997)]. These columns and their activity are important for neural interfacing device design.

Within the brain, there are many different types of neurons and neuroglia, which are supporting cells devoid of neural activity that connect neurons together. The main classes of these neuroglial cells are oligodendrocytes, astrocytes and microglia. Oligodendrocytes form a myelin sheath that wraps around neuronal axons to increase the action potential conducting velocity. Astrocytes and microglia are more interesting from the neural interfacing aspect. Astrocytes are the star-shaped cells that play important roles in CNS homeostasis. These cells constitute the bulk of the cellular composition of the CNS (20 to 50 %) and provide the major source of extracellular matrix protein, adhesion molecules and a large number of growth factors [Squire et al. (2008)]. Finally, astrocytes play an important role in the development, repair and

immune defense of the CNS, and as such are key responders to foreign intrusion in the brain. They perform their immunologic function by migrating towards the injury or inflammation site and form glial scars [Voskuhl et al. (2009)], [Pan et al. (2011)], [Sun et al. (2010)], [Frontczak-Baniewicz and Walski (2006)]. Glial scaring is one of the most problematic issues occurring for some of the most invasive neural interfaces, and leads to rapid deterioration of the recorded signal, which will be discussed in the next section. These cells can be visualized by immunostaining the glia-specific protein GFAP (glial fibrillary acidic protein). Another important glial cell, the microglia, are known as the "tissue macrophage of the CNS" and are another resident representative of immune system in the brain [del Rio-Hortega (1932)], [Wirenfeldt et al. (2011)]. Microglia usually have small rod-shaped somas from which numerous processes extend in symmetrical fashion, however each microglia cell occupies its own territory and collectively forms a network that covers much of the CNS. Microglia respond to pathological conditions involving immune activation and neurodegenerative conditions. The reactive microglia can be detected by two criteria, (1) change in morphology and (2) upregulation of macrophage markers. Microglia change their morphology and antigen expression in response to almost any form of CNS injury and their activated population is detected by immunohistochemistry staining of the calcium binding protein called IBA1 (ionized calcium binding adaptor molecule 1) [Ito et al. (1998)]. For the chronic implant studies of neural interface devices, these two glial cell types are often used as the indicator of biological reaction due to the presence of the device.

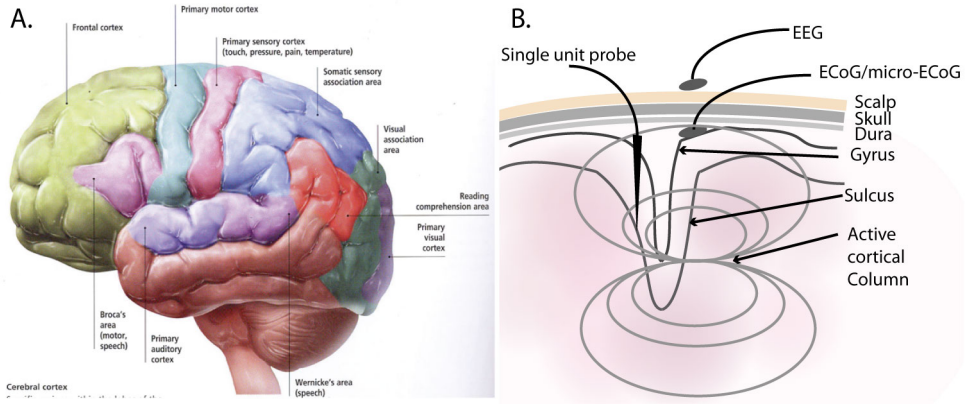

Figure 1.1: A.Brain structure and cerebral cortex distribution (from www.nlphelpsite.com) and B. neural activity and interfacing technologies

Neural interfacing with the CNS

BCI and neuroprosthetic devices rely on recording CNS activity through the associated electric field, either remotely from outside the scalp (e.g. EEG interface) or cortically implanted electrodes (e.g. ECoG devices). These devices have multiple applications, from providing a communication interface for paralyzed patients, monitoring or predicting epileptic seizures, or controlling computer interfaces. In addition, some brain interface devices rely on recording of an evoked activity in CNS after stimulation of sensory function to evaluate their proper function.

The two main categories of neural interfaces for the CNS are near-field CNS measurements and far-field CNS measurements. The near-field extracellular CNS measurements are performed by amplifying the potential difference between a microelectrode tip implanted in the cortex and a reference electrode located within a few millimeters. The far-field CNS measurements

record the electric potential sub-durally, epi-durally or on the scalp.

The recorded signals can be divided in two components, one is the local field potential (LFP) which measures coherent low frequency changes in the membrane potential (<300 Hz) associated with synaptic current of many neurons and the other is higher frequency signal (300 Hz-10 kHz) consisted of multi-unit activity resulting from action potential of nearby neurons. The different frequency components represent the different spatial ranges, up to 100 μm for single-unit signals, hundreds of microns for multi-unit signals and a few millimeters for local field potential (LFP). Devices such as the electrocorticogram (ECoG), the micro-electrocorticogram (micro-ECoG), the electroencephalogram (EEG) as shown in Figure 1.1B are typically used for measuring these signals, with varying efficacies.

Near-field: Single-unit and multi-unit penetrating electrodes

The invasive single-unit and multi-unit extracellular recording or microelectrode penetrating probe made of either micro wires or silicon-based microelectrode are commonly used for recording action potential activity from a single or several pyramidal neurons. These recordings are typically performed in layer V for the primary motor cortex for example, and are used to study cortex functioning for gaining a better understanding of behavior Blum et al. (1991),[Rousche and Normann (1998)], [Baker et al. (1999)], [Williams et al. (1999)], [Kipke et al. (2003)] and to develop neuroprosthetics [Agnew et al. (1986)], [Schmied et al. (1993)], [Maynard et al. (1997)], [Jackson et al. (2006)]. During an action potential, different parts of a neuron's membrane become depolarized leading to the flow of current both inside and outside the neurons. Since the extracellular matrix is conducting as well,

the time-varying potential gradient is formed in the extracellular volume and a changing potential difference can be measured between a point near the cell and a distant reference location. This invasive microelectrode can detect and record a spike or action potential of a single neuron or multiple neurons. The source of the spikes can be determined using spike sorting in an attempt to reconstruct the underlying neural activity [Lewicki (1998)], [Takahashi et al. (2003b)], [Quiroga et al. (2004)],[Nenadic and Burdick (2005)]. However, the invasive penetrating electrode increase the astrocyte response and glial scaring leading to a deterioration in signal quality over time caused by an increase in the electrode/tissue interface impedance only a few weeks after the implant. Currently the signal reliability due to the scar tissue and biocompatibility of the microelectrodes, especially for silicon-based probing electrodes, is a major drawback.

Far-field: EEG, ECoG and micro-ECoG

Initially, far-field recording was performed using non-invasive devices such the EEG for epilepsy monitoring [Uhlhaas and Singer (2006)], [Schevon et al. (2007)] or BCI development. BCI applications (e.g. the commercially available BCI2000 [Schalk et al. (2004)] allow the subject to control the computer cursor or spelling program [Vaughan et al. (2006)], [Allison et al. (2008)], [Felton et al. (2009)], [Wilson et al. (2009)]. However, due to signal attenuation through the skull and scalp and the spatial filtering of the volume-conduction of the brain, the spatial resolution of EEG electrodes are significantly poorer than more-invasive ECoG electrodes. To improve the spatial resolution and signal quality, the invasive sub-durally implanted macro ECoG platform was developed with electrodes approximately 1-

3 mm in size and interelectrode spacing of approximately 1 cm. This technique was originally used for cortical mapping [Leuthardt et al. (2007)], monitoring epileptic activity and BCI applications [Leuthardt et al. (2004)], [Leuthardt et al. (2006)], [Leuthardt et al. (2009)], [Brunner et al. (2011)]. However, the spatial resolution of macro-ECoG does not provide higher resolution needed for more specific connection interface, such as the motor task of fingers, speech, etc. With advances in microfabrication, a smaller microelectrode array, the micro-ECoG platform, was designed to improve the spatial resolution of the traditional ECoG with an array of electrode sites of less than 1 mm in diameter of electrode size with up to 2-3 mm interelectrode spacing, using polyimde film [Takahashi et al. (2003a)], [Kim et al. (2007)], polyimide foil [Hollenberg et al. (2006)] and parylene C film [Hsu et al. (2009)], [Toda et al. (2011)]. The recorded signals from a single micro-ECoG electrode are the aggregation of the action potential from hundreds of neurons in the underlying area around the electrode. This micro-ECoG device provides a signal with superior spatial resolution and quality over the ECoG since the electrode array has higher number of channels on smaller area, as well as being a far less invasive approach than the near-field neural interfaces, resulting in easier implantation, lower glial scaring and longer signal stability over time.

1.2 Neural activity in human eye

In a different context from the neural activity of the brain and the CNS, another variation of neural interface and neural activity recording have been

demonstrated: recording neural activity from the eye, specifically from the retina. The development of flexible thin-film electrode arrays has provided ideal fabrication methods to develop retina activity measurement devices such as the multi-electrode contact lens. In this section I will focus on visual stimuli and their pathways, background on the human eye structure and its neural activity, especially at the retina. This section also covers the basic principle of the electroretinogram, its significance and current ERG technologies.

Human eye structure and neural activity

The human eye is bounded by a tough fibrous outer layer, the sclera, and filled with vitreous humor. On the anterior side is located the cornea, the iris and a lens allowing to focus an image on the retina. Contraction and relaxation of the muscles that link the lens to ciliary body allow its deformation, thus adjusting the focal distance of the eye. The visual information is encoded by the retina and transmitted to the CNS via the optic nerve. The retina-geniculo-cortical pathway in human as shown in Figure 1.2A illustrates the connection of the retina to the visual cortex via optic nerve axons from the nasal retina that cross at the optic chiasm and join axons from the temporal retina of the other eye. These contralateral and ipsilateral axons join to form the optic tract allowing the transmission of information from the retina to the visual area of the thalamus. Subsequently, the axons from the thalamus project to the visual cortex.

The retina itself is constituted of five principal layers, three layers of cell bodies and two layers of neural processes, dendrites and axons (Figure

1.2B) [Bairati and Orzalesi (1963)],[Hee et al. (1995)]. The vertebrate retina is oriented within the eye to maximize the light transmission through the inner layers to the photoreceptors which comprise the outer-most layer [Curcio et al. (1990)]. The inner nuclear layer contains cell bodies of interneurons of the retina including bipolar cells, horizontal cells and amacrine cells. The final cell layer is ganglion cell layer which is home to the retina neurons whose axons form the optic nerve [Curcio and Allen (1990)]. There are two types of photoreceptors; rods and cones that are hyperpolarized upon reception of light [Bowmaker and Dartnall (1980)]. Rods and cones have outer segments that contains the molecular machinery for phototransduction, an inner segment that contains densely packed mitrocondria, a cell body that contains the nucleus and other important organelles, and a terminal process that releases neurotransmitter [Ebrey and Koutalos (2001)], allowing the transmission of visual information. Phototransduction occurs when photons are absorbed by pigments located in the outer segments of photoreceptors. Rods contains rhodopsin and are sensitive to blue-green light; they are used for dark/dim conditions at night. Cones on the other hand contain opsins which are sensitive to either long wavelength (red light), medium wavelength (green light) or short wavelength (blue light) depending on their specific structure [Gouras (1984)]. Increments in light reception lead to a hyperpolarization and a reduction in neurotransmitter release, whereas decrements in light reception lead to a depolarization and an increase in neurotransmitter release. Subsequently, the graded potential is transmitted eventually to ganglion cells that provide the output of the retina to the CNS.

Photoreceptors play an important role in the visual system and abnor-

malities in photoreceptors can cause some disabilities, such as visual loss in diseases such as retinitis pigmentosa [Marmor (1980)], [Pruett (1983)], [Kaplan et al. (1990)], and other retina dysfunction-diseases [Usui et al. (2004)], [Terai et al. (2011)]. The electroretinogram (ERG) allows the measure of the electrical response of the different cell types in the retina and the electrooculogram (EOG) allows to test the resting potential of the retina. Both of these devices are useful tools to assess retina function and help diagnose the presence of these diseases, such as glaucoma [Viswanathan et al. (2001)].

Neural interfacing in the human eye with ERG

In the late 1860s', Holmgren found that light stimulus causes electrical potential in the amphibian eye. The positive electrical difference in the cornea relative to the back of the eye was discovered by introducing the light through the pupil [Armington (1974)]. The measurement of the light-induced electrical activity of the eye was called electroretinogram (ERG). The response of the retina to a light flash stimuli consisted of three phases; first the photoreceptors hyperpolarize (negative a-wave) followed by larger positive amplitude wave (Figure 1.2C) and finally, a longer-lasting positive wave (c-wave). In addition, in some cases a corneal-positive wave can be recorded at the end of the light flash, also called d-wave. These a-, b-, c- and d-waves are the primary ERG component phases.

Extracellular local current originating from rods and cones (negative potential a-wave) [Brown and Murakami (1964)], [Sillman et al. (1969)], ON-bipolar cell (b-wave) [Sillman et al. (1969)], [Nilsson (1971)], pigment

epithelium cell (c-wave) [Noell (1954)], [Pepperberg and Masland (1978)] and OFF-bipolar cell (d-wave) [Xu and Karwoski (1995)] can flow within the retina (pathway A) while pathway B represents current flow through vitreous cornea and extraocular tissues (Figure 1.2B,C). This current returns to the retina via the choroid and pigment epithelium (Figure 1.2C). ERG responses in human are recorded with an active extracellular electrode positioned either on the cornea, in the vitreous humor or at different levels inside the retina [Marmor et al. (2009)]. The extracellular recording of the electrical activity is possible when field potential transmit through the vitreous humor, pupil and cornea. In this context, I will only focus on the extracellular ERG recorded from the corneal surface. Since there is some distance between the retina and the ERG electrode, the electrical potential will be attenuated as it is conducted through the vitreous.

Factors effecting the ERG

There are four factors that can affect the ERG; first is the state of adaptation to light of the retina, second is stimulus strength, third is the color of the light stimuli and forth is the frequency of the light flashes. For simplicity, I will focus on only two of these which are the state of adaptation and the light intensity. The state of adaptation plays different roles for night vision (rod system) and day vision (cone system) since they operate independently. However, in human both systems are found [Curcio et al. (1990)]. The rods are sensitive to the dim light stimuli in the dark-adapted state while under background illumination, these saturate and produce no response to the variation of the light intensity [Hood and Finkelstein (1979)]. On

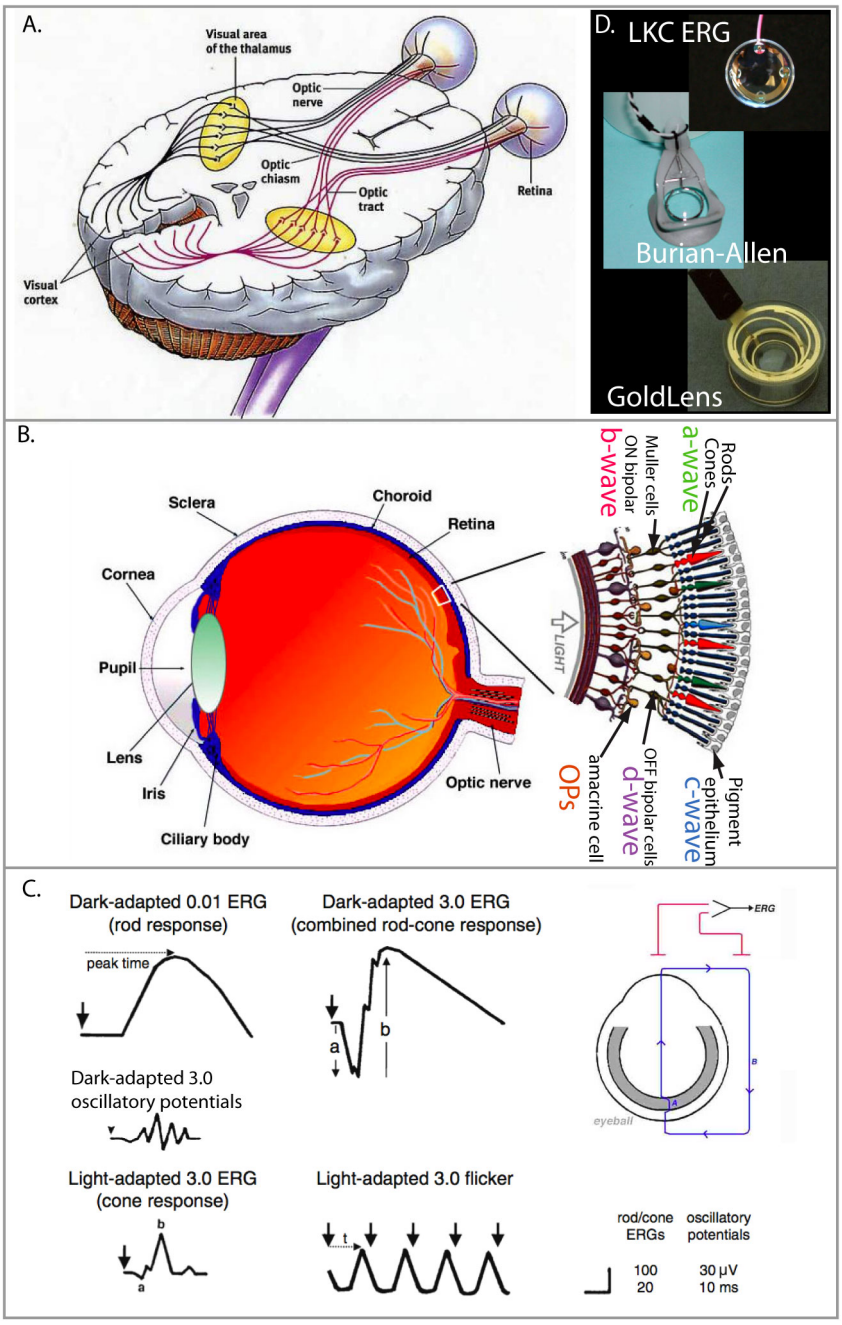

Figure 1.2: A. Visual pathway from retina to the visual cortex. B. Human eye and retina structure. C. International Society for Clinical Electrophysiology of Vision (ISCEV) standard for ERG stimulating paradigm and electrical circuit pathway between the retina and ERG. D. Current ERG electrodes available on the market. (Adapted from webvision.med.utah.edu)

the other hand, the cone system is less sensitive than the rod system but it is characterized by the ability to adapt to bright lights allowing our vision to adapt to background illumination over a broad range of intensities. Recording cone and rod function can be made separately by modulating the state of their adaptation to light. Applying a stimulus while providing background illumination, causes saturation of the rod system, which reflects cone response in the ERG measure. The second factor, light intensity, is also important for clinical ERG measurements. With a dim light stimulus, the ERG shows a long-lasting positive wave of small amplitude (b-wave) whereas increasing intensity of the stimulus shows on the ERG as a negative a-wave preceeding the positive b-wave [Armington (1974)].

Analysis of ERG

The two components that are most often analyzed are the a- and b-waves. The a-wave is the first large negative peak, followed by the b-wave which is corneal positive and usually larger in amplitude. In clinical ERG for retina function testing, many aspects including amplitude and implicit time, and the ratio of b-wave to a-wave amplitude are commonly considered. The standard light stimulation for different adaptation states used for ERG measurement is set by the International Society for Clinical Electrophysiology of Vision (ISCEV) [Marmor et al. (2009)] as shown in Figure 1.2C. The a-wave amplitude is measured from baseline. Temporal properties of the ERG response are defined by the time-to-peak (implicit time). With increasing stimulus strength, the b-wave amplitude increases until a plateau is reached and at higher stimulus strength, the largest recordable b-wave is obtained. At this stimulus strength, an a-wave becomes evident. The relationship

between the amplitude and intensities provides quantitative assessment of retinal function during the progress of retinal diseases and suggests a choice of treatment [van Lith (1981)], [Stodtmeister et al. (1988)]. It is worth noting that the amplitude and implicit time relationship is only suitable if the experiment setup is constant, therefore it is more difficult to use as a diagnostics tool as comparison between different laboratories is often difficult. Consequently, the ratio of b-wave and a-wave is used in this situation.

Current ERG technologies

Currently, there are several ways to record ERG. After the pupil is dilated, different types of corneal contact ERG electrode can be used to record ERG electrical signal (Figure 1.2D). One of the most commonly used by the clinician is the Burian-Allen® electrode that can hold the eyelid open with a gold or carbon wire ring that floats in the cornea [Lawwill and Burian (1966)]. The simple gold Mylar tape electrode is also used for recording the ERG when the eye is very small [Arden et al. (1979)]. For different eye size and condition, the electrode is selected accordingly. A monopolar gold coil fitted inside the eyecup as shown in Figure 1.2D is another option to achieve the same type of ERG measure. The later developed ERG-jet contact lens type (Figure 1.2D: LKC ERG) is commonly used nowadays because of its simplicity and comfort, however a report has shown possible stimulus artifacts [Gehlbach and Purple (1993)]. To date, there is little report of thin-film multi-electrode ERG in which multiple ERG waveforms can be measured simultaneously. For higher spatial information from the ERG electrodes, image forming ERG lens is desirable. Chapter 6 will delve on the development of a novel multi-electrode ERG in more detail.

2 THIN-FILM NEURAL INTERFACE DEVICES FABRICATION METHODS AND TECHNIQUES

The development of thin film neural devices has been largely based on the innovations made in microfabrication techniques, used in many other applications including electronics devices. Amongst the various materials available, two are of particular interest in the context of thin film neural devies, polyimide and parylene C. To be considered as a thin-film neural interface device substrate, the polymer has to possess good dielectric property, moisture uptake resistance, chemical resistance, biocompatible and excellent mechanical properties. These two materials have distinctive properties that make them suitable for different applications. Polyimide is one of the most commonly available polymers that has excellent moisture and electrical insulation properties and if flexible (Figure 2.1C). Currently there are different types of polyimide polymers available in the market, but the photodefinable polyimide is the preferred choice due to its simplicity in microfabrication that does not require hazardous chemicals, such as Hydrofuric Acid (HF) for the etching process. Parylene C is one of the first and few materials that have been approved by the FDA for chronic implant devices. It also has higher light transmission property than polyimide and looks transparent. This latter advantage, has been leveraged for optical pertinent applications, such as optogenetic-enabled devices, electroretinogram, artificial retina de-

vice and traditional surface electrodes. In this chapter, I will present and discuss the fabrication processes of polyimide and parylene C for thin film neural interface development, and methods used to interface with them. The fabrication process of polyimide and parylene C present here are the fundamental background for the devices used in the following chapters.

2.1 Polyimide device fabrication

The fabrication of micro-ECoG devices is largely based on a traditional photolithography techniques. For this device, polyimide serves both as a base that provides mechanical strength, on which the electrodes are deposited, and an electrically insulting layer for the conductive metal traces linking the electrodes. A photodefindable polyimide substrate was chosen over ready made polyimide sheet as they do not require the use of Hydrofluoric acid (HF) as an etchant for patterning. Additionally, photodefinable polymide reduces the number of overall steps in the lithographic process. Platinum was used to cover the traces and electrode sites to improve electrical characteristics, including decreasing the electrode impedance and reducing a possibility of gold corrosion that could cause immunological response. The shapes and sizes of electrodes were systematically varied, yielding a wide array of electrode designs (Figure 2.1B). Each electrode array consisted of 16 or 32 electrode sites corresponds to the channel available with the 32-channel headstage pre-amplifier unit.

The electrode fabrication process (Figure 2.1A) is described in the following (see more details in Appendix A). After cleaning the 4-inch silicon wafer

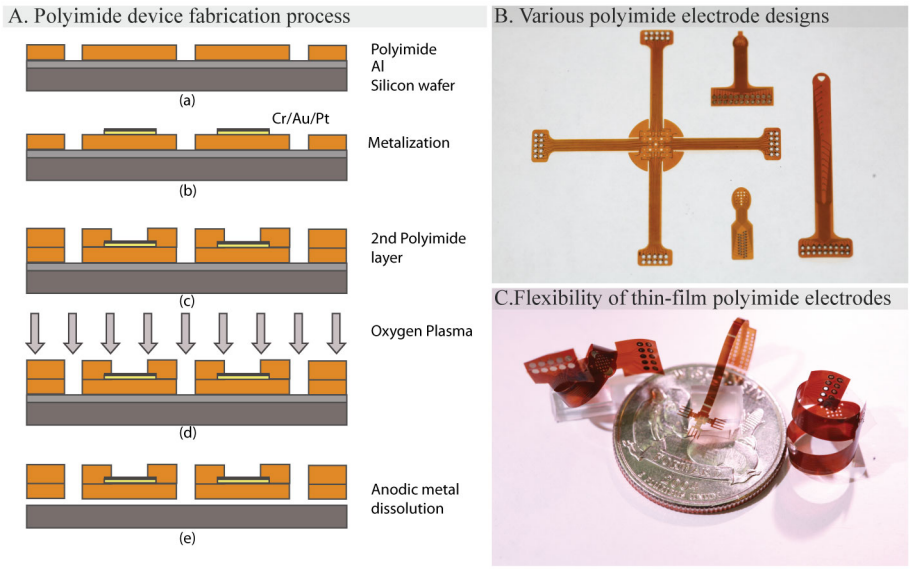

Figure 2.1: A. Polymide device fabrication process using traditional photolithography technique. B. Different polyimide electrode designs. C. Illustration of the flexibility of thin-film polyimide electrodes

with acetone, a 200nm thick layer of aluminum was evaporated (CHA-600 E-beam Evaporator) onto the surface as a sacrificial layer. Polyimide (HD 4110, HD Microsystem) was spun coated and patterned using photolithography (Mask aligner: MA6 Suss MicroTec) following the manufacturer's recommendation to form a 12 µm thick base layer. Photolithography masks were designed in Adobe Illustrator, and were printed on high-resolution transparency masks (Fineline-imaging, Colorado Springs, CO). A Micro-electrocorticography Platform and Deployment Strategies for Chronic BCI Applications polyimide (Figure 2.1A(a)). The polyimide was subsequently cured at 375 °C under a nitrogen atmosphere for 5 hours (Cooke Oven). A metallization step (10nm Cr/ 200nm Au/ 20nm Pt) defining the interconnec-

tion pads, connecting traces, and electrode sites was performed using electron beam evaporation (CHA-600 E-beam Evaporator) and a lift-off process. Platinum was chosen as the electrode material due to its low polarization at the phase boundary and also its low and stable impedance. The second layer of polyimide was then spin coated, patterned and cured under the same conditions as the first base layer. Before releasing the device, oxygen plasma (RIE Unaxis 790) was used to clean the surface for 2 minutes (250W, 20Torr) ensuring that the remaining polyimide and solvent residue on the electrode sites and contact pads were completely removed(Figure 2.1A(d)). The thin film devices were released using an anodic metal dissolution technique. In brief, the wafer was immersed in a sodium chloride solution (2M) with Pt counter electrodes under an applied voltage of 0.8 V that allowed the dissolution of the aluminum layer and release of the polyimide film. To complete the process, the devices were soaked in DI water, cleaned and dried.

2.2 Parylene C devices

Parylene C deposition process

Parylene is the tradename for a number of chemical vapor deposited poly(p-xylylene) polymer varieties commonly used as moisture and dielectric insulators. Parylene C with one Cl group per repeat unit (Figure 2.2A), is the most popular variety due to its low cost, excellent barrier properties and simple deposition processing. Parylene C can be conformally deposited on the sample surface at room temperature without using any initiator, terminator

or solvent and catalyst. This green deposition process makes fabrication process simple, safe for the user and unlikely to have harmful residue chemicals. The deposition process requires medium vacuum (~15mTorr) and high temperature furnace (690 °C) for dimer pyrolysis into monomer. Then the monomer particles deposit onto the sample surface at room temperature in the vacuum chamber (Figure2.2A).

Parylene C device fabrication process

Parylene C devices are fabricated under biocompatible condition starting from a chemical vapor deposition process and then simple photolithography, following by oxygen plasma etching (Figure2.2B). One major drawback of parylene C is poor adhesion to most smooth and non-porous substrate including silicon wafer without any prior treatment. In the context of thin film neural interfaces, the material constitutes the substrate of the device, and therefore its poor adhesion to other materials is not as critical. However, consideration should be put into choosing a suitable surface treatment for the silicon before the first layer of parylene C deposition to ensure that the film adheres to the wafer throughout the whole fabrication process without peeling off or forming bubbles. Several groups have demonstrated techniques to achieve this. One convenient technique is oxygen plasma treatment of the silicon wafer to modify the surface chemistry. Another approach uses an adhesive promoter recommended by parylene manufacturer, A-174 Silane, which can be vapor coated in situ or bonded via chemical wet bath [C J Mitchell (2006)]. This material creates a self-assembled monolayer of molecules that bond to the surface on one side and co-polymerizes with the

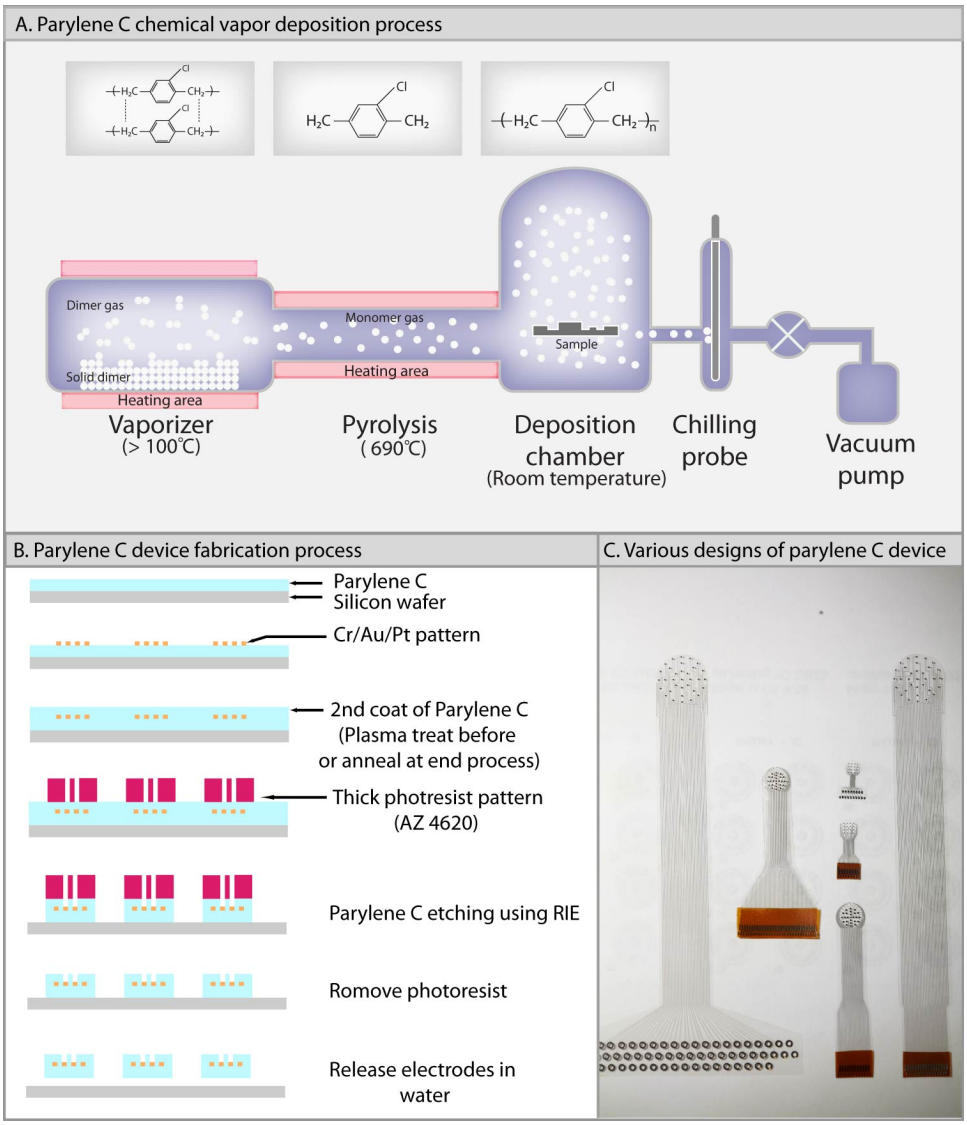

Figure 2.2: A. Parylene C chemical vapor deposition process, B. Parylene C device fabrication process. C. Various designs of parylene C device for different applications

parylene via a free radical addition reaction on the other.

The parylene neural interface devices were fabricated starting from plasma treated the silicon wafer substrate for adhesive promotion and then depositing 15 μm layer of parylene C (Figure2.2B). Via photolithography (Mask aligner: MA6 Suss MicroTec) and lift-off process the 10 nm Cr/ 200 nm Au/ 20 nm platinum metal layers were deposited and patterned to form the electrical connection traces and electrode sites. Subsequently, the second layer of parylene C (10 μm) is coated for electrical insulation. Patterning the devices and opening the electrode sites were performed via photolithography and oxygen plasma etching. Two layers of AZ P4620 (AZ Electronic Materials USA Corp) were spin coated to form 24μm layer of photoresist which is a photo-mask for oxygen plasma etching process (RIE Unaxis 790) at the rate of 0.3μm/min. Biocompatibility concern is the reason that oxygen plasma was chosen over more aggressive etching process with different gases. Finally, the devices can be released from the silicon wafer substrate via soaking in water bath (see more details in Appendix B).

2.3 Connection scheme

An overlooked challenge in developing neural interfaces is the creation of a reliable connection scheme to interface with the macro-scopic world and measurement devices. Some groups have proposed the use of wireless technologies, however, these have not reached a sufficient level of reliability in chronic implant studies. The alternative is the use of a physical wire connection either though soldering the electrode directly, which requires an

awkwardly large connector [Hollenberg et al. (2006)], or through an expensive custom-built micro-connector, which requires meticulous hand soldering like the "MicroFlex Interconnection" [Rousche et al. (2001)] and nano-strip connector (Omnetics Connector Corp.) [Henle et al. (2011)], [Rubehn et al. (2009)]. Thus the yield of such electrodes depend on the skill and experience of the assembly person. Large quantity of soldering is tedious and resulting in low yield. In this study, the alternative solderless connection schemes will be described and discussed. One alternative is the mechanically connecting DIP (Dual in-line package) sockets where the connection is solely depend upon the mechanically contact pins. The other is the Zero Insertion Force (ZIF) connector that is widely used in the flexible circuit and electronic applications.

Mechanically connecting: DIP interconnect socket

Mechanically connecting the electrode contact pads and the connector pins is possible using sandwiching the electrode contact pad between two DIP interconnect socket pins (MilMax Mfg. Corp.) where the shoulder and the hole are the contact points (Figure 2.3A). This straightforward connection can reduce assembly time significantly. The first contact pad is a simple ring contact designed to fit on the shoulder of the connector pin. However, this design results in approximately 80% yield of all connecting pins due to the chance of damaged contact pads during mechanically pressed between the two connector pins as shown in Figure2.3B. Therefore a serrated annular ring contact pad shown in Figure 2.3C was developed to relief mechanical stress at the connector shoulder and improve the connectivity yield to almost 100%.

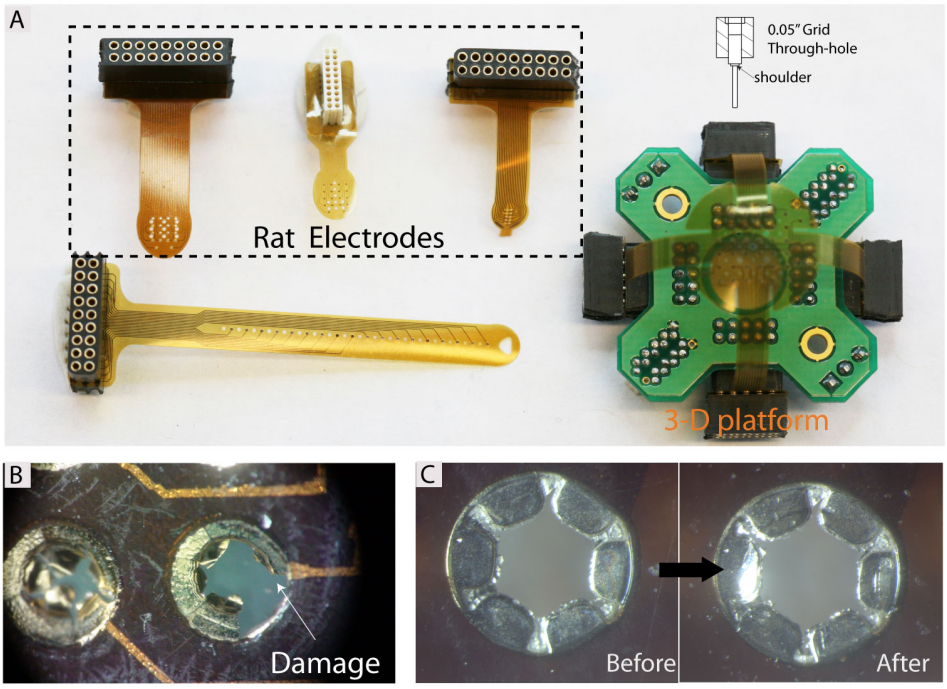

Figure 2.3: A. Different electrode designs using the Milmax connector. B. Damage on the contact ring due to the mechanical stress when clamping two Milmax pins together to form electrical connection. C. Modified contact pad with serrated annular ring designed to relieve mechanical stresses at the pin shoulder and reduce the damage.

Figure2.3C (right) shows that mechanical stress was relief as the leaflets of the contact pad can conformally wrap around the connector shoulder and hence avoid an unnecessary damage.

Nevertheless, the DIP interconnect socket has one drawback that is crucial in animal study practice. The difficulty associating with plugging and unplugging the MilMax-connector headstage adaptor for each recording experiment is not user friendly. Moreover, when plugging and unplugging

the headstage adaptor a significant force is required creating an unnecessary pressure and stress on the animal, especially the rat electrode design. Despite this disadvantage, a 3D platform electrode shown in Figure 2.3A leverages this tight contact of the DIP sockets and provides a stable platform for the four-tethers monkey electrode.

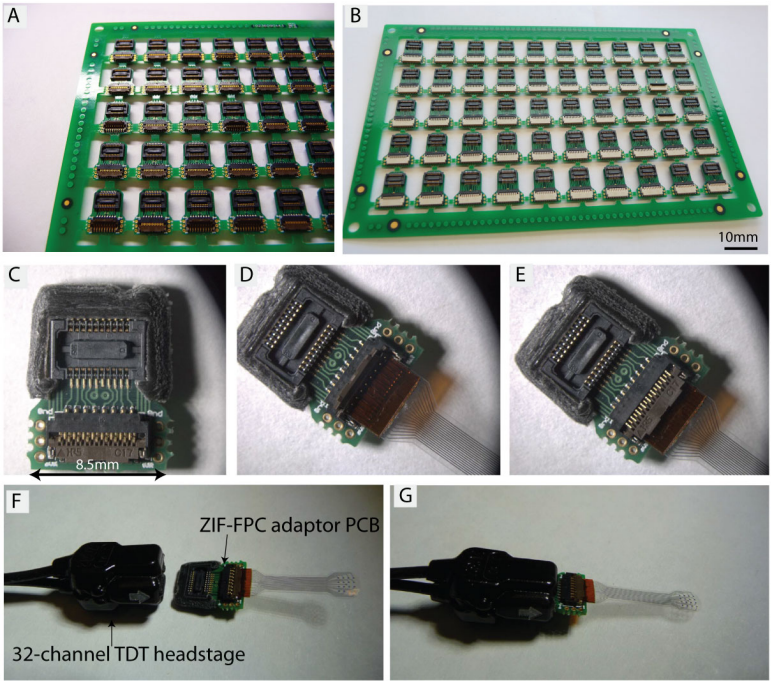

Figure 2.4: A,B. Custom made PCB for double-sided ZIF headstage connection with either a bottom contact (A) or top contact (B) flexible printed circuit (FPC) connector. C. Input from electrode array (FPC) connector and output to ZIF connector in the headstage. D,E. Illustration of the simplicity to assemble the electrode array on a PCB via inserting in the FPC connector and closing the latch. F,G. User friendly ZIF headstage from TDT connecting with the ZIF-adaptor PCB.

Zero Insertion Force (ZIF) connector and Flexible Printed Circuit (FPC) connector

Extending the simplicity of solderless connection scheme, another connector commonly used for connecting the thin-flexible electrode cable is FPC connector. The FPC connectors are available from many venders and come in different packages with various number of contact position, type of contact and spacing, depending on the manufacturer. Using the 32-channel ZIF-headstage from Tucker-Davis Technologies (Figure 2.4F), a ZIF-FPC adaptor printed circuit board was designed and mass-produced in order to achieve the cost-effective device. This approach was used as shown in Figure 2.4A (bottom-contact FPC connectors) for the electrodes designed for bilateral implant studies where the electrode sites can be facing down on the cortex and Figure 2.4B (top-contact FPC connectors) for those electrodes designed for 32-channel electrodes suitable for non-human primate implant studies. This adaptor PCB is not only cost-effective, but also user friendly as electrode assembly can be easily executed by inserting the electrode cable and closing the latch (Figure2.4D and E).

3 MATERIAL CONSIDERATIONS FOR THIN-FILM NEURAL INTERFACES

Neural interface devices are divided into two different categories that target either the central nerve system (CNS) or the peripheral nerve system (PNS). These devices show significant similarities in material choices and fabrication methods but also key differences. As the PNS and CNS have different nerve structures, the interface devices require a specific feature design to maximize their signal recording quality and match the mechanical properties of the target nerve tissue, such as stiffness and geometry. This chapter will emphasis on neural interface that targets the CNS, a region where the brain is soft and elastic [Guillaume et al. (1997)]. Thus, the creation of a suitable neural interface device requires the choice of a flexible material with a Young's modulus close to that of the brain to minimize any biological and immunological response due to its presence. Polyimide and parylene C are the most frequently used materials for neural interface devices especially ones that fall in the category of micro-ECoG since they are flexible with Young's Modulus of approximately 3.5 GPa for polyimide (HD microsystem) and 3-4 GPa for parylene C [Hsu et al. (2009)], [Hassler et al. (2010)].

Both of these materials have unique properties and require a specific fabrication process. Although the use of polyimide and parylene C as encapsulating materials for neural implant device have been reported [Hassler

et al. (2010)], little characterization of these materials exists. Of particular interest for implantable neural interfaces is their long-term behavior in a chronic implantation context. This study aims to test the long-term stability of electrode impedance, signal quality and biological response of the devices with polyimide and parylene C encapsulations. Different methods are used to approach this characterization work. First, a general idea of the behavior of the electrode can be obtained entirely in-vitro by performing accelerated soak-tests, to speed up the degradation of materials and transport of metal ions. Although these test provide a good idea of the material resistance, they do not provide information on the biological response of the implanted device in the brain. In-vivo testing is ultimately needed to identify biological reactions to the foreign body, including vasculature growth response, scar tissue, bone growth and astrocyte, and microglia response.

3.1 Property changes of polyimide and parylene C after accelerated soak test

A long-term assessment of the material insulation and mechanical properties in a normal body temperature (37 °C) and normal biological environment is a time-consuming process. The alternative is to accelerate the process by elevating soaking temperature of phosphate buffered saline (PBS) to 90 °C to assess various possible failure mechanisms including corrosion, wear and delamination of the implantable microdevices. The relative time scale of the accelerated test can be evaluated by using the classic Arrhenius equation for acceleration of degradation by temperature in a first order chemical reaction

or diffusion process [Whitmore and Schenkelberg (1997)]. The estimated stability at 90 °C for 1 day is assumed to be equal to 236 days of stability in body temperature (37 °C).

We tested in parallel neural devices fabricated out of polyimide and parylene C materials and recorded various physical, chemical and material properties over time. These tests include measurement of impedance changes over time, as these could suggest changes in the electrode surface morphology due to the accelerated electrolysis or oxidation as well as possible failure of the encapsulating material due to delamination. The test also record the variation in the materials tensile strength or Young's Modulus that could indicate any sign of degradation and moisture absorption.

Tensile strength

Mechanical properties such as tensile strength and strain were measured for both polyimide and parylene C electrodes to understand the correlations between the mechanical degradation of the substrate polymer and failure of the thin film electrode array observed during long term implantation. A number of American Society of Testing and Materials (ASTM) standard specimens of polymide and parylene C were soaked in accelerated condition for 30 days. The tensile strength of the polyimide and parylene C thin film was measured with specimens fabricated using the ASTM D638-03 process with a Tensile Testing machine (MTS system, MN, USA). The specimen has a thickness of 20 μm, a gauge length of 63.5 mm, and a gauge width of 3.18 mm. Each tensile strength data point was obtained using at least 3 specimens.

Stress-strain analysis of thin parylene C film shows relatively small values of tensile strength (approximately 80 MPa) and around 160-190 MPa for polyimide specimens as shown in Figure 3.1A. Their initial tensile strength were similar to manufacturer data sheets and decreased after a few days of soak test. The tensile strength of both polymers appear to be stabilizing after a period of 30 days, although parylene C appears to have more stable tensile strength over the time. This discrepancy could be explained by the different moisture absorption of each thin film [Hennig et al. (2004)], i.e. less than 0.1 % for parylene after 24 hours (from Special Coating Systems data sheet) compared to 1.3% for PA-4100 Polyimide film (HD Microsystems data sheet). Despite of the slight decreasing of tensile strength from these the preliminary data, both polymers appear to be stable for more than 20 years based on the time scale calculation given by the Arrhenius law.

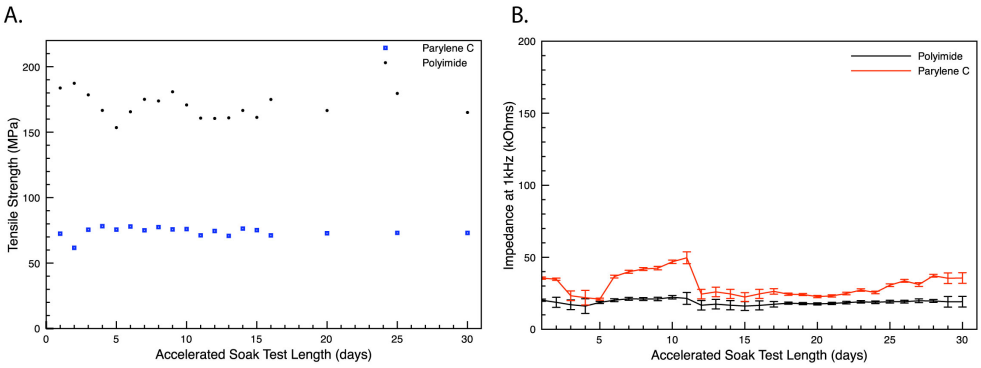

Figure 3.1: Tensile Strength and Electrical Impedance of the polyimide and parylene C devices correspond to accelerated soak test time. A. Variation of polyimide and parylene C tensile strength after accelerated soak tests. B. Variation of the polyimide and parylene C electrical impedence showing a stable trend after day 12.

Electrode impedance

The consistency of the electrical recording is a central aspect in developing chronic implantable devices providing a reliable signal upon which biological conclusion can be drawn, diagnoses and treatments can be performed, and BCI can be developed. It has been suggested that polyimide can experience high water vapor adsorption, which can lead to swelling and delamination of metal/polyimide interfaces [Blum et al. (1991)]. The parylene-based implantable electrodes reported by Wen Li *et. al* suggest that the moisture absorption may be the cause of failure as a large increment of electrical impedance in accelerated soak test were observed [Li et al. (2006)]. To assess the change of impedance due to an accelerated soak test condition, the connected micro-ECoG samples were soaked in a custom made test tube sealed with PDMS lid containing phosphate buffered saline solution at 90 °C and measured electrode impedance once per day for 30 days. General mechanical failure such as degradation and delamination can also be observed.

The preliminary results shown in Figure 3.1B indicate that the electrode impedances at 1 kHz of a set of five polyimide and parylene electrode pairs soaked under accelerated condition are fairly stable after 12 day. The initial fluctuations may be due to control issues originating from the custom build experimental setup. These results suggest that both polymers withstand the accelerated soak test condition and show that the polymer degradation and platinum electrode corrosion may not occur significantly enough to increase the electrode impedance. These accelerated *in-vitro* electrode impedance

measurement results indicate that both polyimide and parylene neural interface device could be stable for more than 20 years in normal body temperature using Arrhenius-equation model. Nonetheless a chronic implant study in rats is necessary to reveal additional sources of electrode failure.

3.2 Chronic implant studies in rats

In addition to the material considerations, chronic implanting of neural devices poses significant challenge due to the biological response of the organism. Biological reactions to foreign objects, including vasculature growth, scar tissue, bone growth and astrocyte, and microglia response are possible mechanisms of device failure over time. Verifying that there is no significant immunological and biological reaction observed after at least 6 months is important for developing effective neural interface devices, but also critical to start non-human primate studies and ultimately clinical trials. Therefore, we performed chronic implant studies in rats to test thin-film electrode impedance stability, quality of recording signal, durability of the entire equipment setup including the connector and biological reaction of the electrode *in-vivo* over a long time period. Polyimide and parylene C neural devices were implanted bilaterally on rat brains in order to compare the induced biological responses in the living condition.

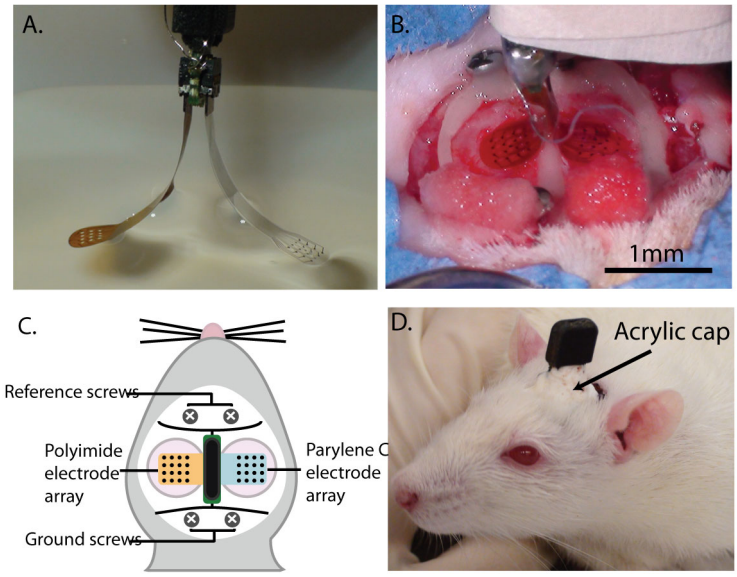

Figure 3.2: A. Polyimide and parylene C electrodes with ZIF-FPC adaptor board assembly. B. Bilateral craniotomy for polyimide and parylene electrode placement and stereotaxic tower for lowering and placing the electrodes on the cortex. C. Location of electrodes and ground/reference screws. D. Sealing of the craniotomy and securing of the entire head cap with acrylic for long-term studies.

Methods and materials

Micro-ECOG implantation

Rats were implanted with an epidural micro-ECoG electrode over sensorimotor cortex. Three male Sprauge-Dawley rats weighing approximately 300 grams were selected. Surgical methods closely follow previously published work [Williams et al. (1999)], [Rousche et al. (2001)]. The animals injested buprenorphine (0.05mg/kg subcutaneous injection) for analgesic control during the surgical implant procedure. Subsequently, they were induced

with 5% isoflurane gas and then maintained on 1.5-3% throughout the duration of the surgery. Following isoflurane anesthesia, rats were placed into a stereotaxic frame, and the scalp shaved and prepped with alternating povidone iodine and alcohol. After the initial incision, exposed skull was cleaned and dried. Two stainless steel screws (size 00-80), one for attachment of a ground wire, and another for mechanical support, were attached to the rostral and caudal areas of the skull (Figure 3.2B). Next, UV curable acrylic (Fusio) was placed on the periphery of the exposed skull to provide an anchor for the attachment of future acrylic. A small craniotomy (5mm x 5mm) was made using a spherical burr (Dremmel #106, 107) made for use with a high speed surgical drill. After exposing the dura, the micro-ECoG was placed epidurally onto the somatosensory area of the cortex. GelFoam (Pharmacia and Upjohn Co, New York, NY) was placed on top of the electrode to protect the device and the brain tissue. The connector was then cemented onto the skull with acrylic, and a cap was made to encapsulate and protect the electrode. The wound was closed using a purse string suture (3-0 vicryl absorbable). Triple antibiotic ointment was added to the wound during closing to prevent infection. Rats were monitored post-surgically until they were ambulatory and showed no signs of pain or distress. An additional dose of buprenorphine was given 8-12 hours after the initial dose to relieve any pain the animal may have been experiencing following the surgery. All procedures were approved by the Institutional Animal Care and Use Committee at the University of Wisconsin Madison.

Cranial window implantation

Biological reaction can also be observed *in-vivo* by utilizing the cranial window surgical technique [Forbes and Wolff (1928)],[Morii et al. (1986)] that allows imaging in real time of the brain surface. The cranial window implantation for *in-vivo* brain imaging was done similarly to the previously mentioned surgical technique. Instead of covering the implanted device with the gelfoam and UV curable acrylic, the devices were placed on the craniotomies and covered with 5 mm circular glass coverslips to create the window through which the electrode array and the brain surface could be imaged over time (Figure 3.6). The perimeter of the craniotomies were then covered with thin gelfoam and UV curable acrylic to seal the entire window. Under the cranial windows, the electrode arrays was carefully placed without applying excessive pressure on the cortex surface or dura.

***In-vivo* imaging through cranial windows**

During the imaging procedure, the animal were anesthetized without causing any respiratory depression under Dexmedetomidine (100 μg/kg) and the heart rate and oxygen level were monitored regularly. Under anesthesia, the rats were fixed with the sterotaxis and ear bars to minimize the breathing pulsation during the imaging. The bright-field images of the brain surface and electrode array were taken from the upright microscope (Nikon). Then the fluorescein isothiocyanate-dextran (FITC-dextran) (10-100 mg/kg in 0.2ml saline) was administered via tail vein injection in order to make blood vessels fluoresce under the blue light. The blood vessels formation and growth

were observed closely and imaged twice a week. The rate of angiogenesis occurs on polyimide electrode in comparison with the parylene C electrode was determined. At the end of the imaging session Atipamezole (up to 100 μg/kg) was administered to reverse the Dexmedetomedine effect.

Histology of the brain

After the implantation ended, the rat brains were fixated using 4% paraformaldehyde solution under the deep anesthesia with pentobarbital (120 mg/kg) and 5% Isoflurane gas anesthesia throughout the procedure. Before the fixation initiated, the transcardiac perfusion with phosphate buffered saline was applied for 10 mins and then follow with 4% paraformaldehyde solution for 10 mins. Following perfusion, brains were stored in the Hank's Balances Salt Solution (HBSS) with Sodium Azide (90mg/L).

Rat brain was then sliced at 80 μm using a vibratome and immersed in Hank balance salt solution (Sigma-Aldrich) with sodium azide (90 mg/L). Brain sections were then stained for GFAP and IBA-1 markers, characteristic of astrocyte and microglia expression. Sections were washed in Hank buffer-HEPES with sodium azide solution and then sodium borohydride (452882, Sigma-Aldrich). After rapid rinsing, sections were washed with 1-2% Triton X100 (X100, Sigma-Aldrich). Then soaked in 5% Brovine Serum Albumin (BSA, Sigma-Aldrich) overnight. Primary antibodies used were rabbit anti-GFAP (anti-GFAP raised in rabbit, G4546, 1:500; Sigma Aldrich) and rabbit anti-IBA1 (1919741, 1:800; Wako). After washing with 0.5% weight Tween 20 (P1379, Fisher Scienctific), sections were then incubated in secondary antibodies Alexaflour488 anti-rabbit (A-11029, 1:200; Invitrogen)

and Alexafluor568 anti-rabbit (A-11036, 1:200; Invitrogen). Tissue slices were then washed with Tween solution and mounted on the glassslide with prolong gold (see more details in Appendix D).

3.3 Results

The chronic implant results obtained from this preliminary stage could indicate whether different encapsulating materials like polyimide and parylene C have any impact on the electrode impedance and signal quality in the long run. This section presents more details on the electrode impedance characteristics and signal quality monitoring in alive animals.

Impedance monitoring

The impedance measurements from the 32-channels electrode (16-channel for each side) chronically implanted in 6 rodents were taken weekly for 3, 6 and 12 weeks to monitor the changes in magnitude and phase angle. These changes are illustrated with the Nyquist plots of an example rat (M25) shown in Figure 3.3. The R-X relationship of impedance spectrum across the electrode array was very linear a week after implantation (dark blue); however, there is a slight increase in impedance magnitude similarly to other published studies [Takahashi et al. (2003a)], [Henle et al. (2011)]. After implantation for 3 months (orange), the impedance plots appear to have higher real component and no longer exhibit the linear relationship between R and -X, and have a slight variability of the imaginary component of the impedance spectra. Hence, we hypothesize the existence of some biological

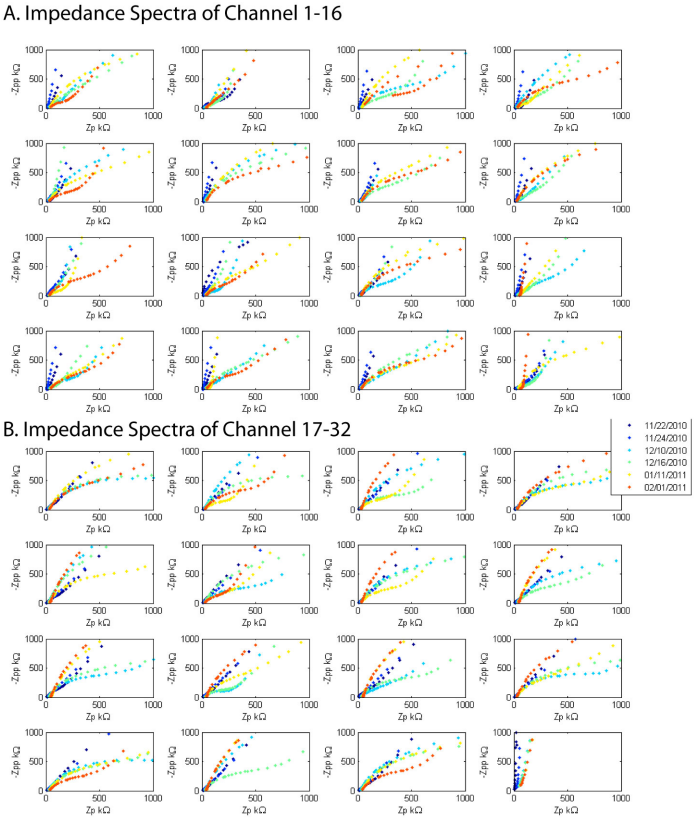

Figure 3.3: Post-implant impedance spectra of M25 (recorded weekly). Decreasing of the complex impedance phase angle indicates an increase in impedance possibly due to a mild tissue response on the electrode surface. A. Example of impedance spectra of polyimide electrode channel 1-16 over 3 months and B. Examples of impedance spectra of parylene electrode channel 17-32 over 3 months.

reaction to the foreign object presence after implantation.

When looking at the evoked potential response at 1 kHz, Figure 3.4 shows an increasing in the magnitude of impedance after week 2 for both polyimide and parylene devices. Following the increase, Figure 3.4C and D show that the electrode impedance at 1 kHz stabilizes after week 6 in all animals. This increasing of electrode impedance amplitude is observed in all rats and could be due to the thickening of the dura or a thin layer of bone tissue growth underneath the electrode. These results will be discusses further at the end of the chapter. Furthermore, the electrode impedance recorded on an individual site of mouse M25 (Figure 3.4E) as well as the average impedance from mice ID M46, M47, M26, M27 and M24 (Figure 3.4A, B, C, D and F respectively) show no significant difference between encapsulating materials confirming the results found *in-vitro* testing.

Signal quality monitoring

The slight elevations of electrode impedance described in the previous section raise a question whether high impedance magnitude has any effects on post implant signal quality. To monitor power spectrum across the entire electrode array and their signal quality, weekly baseline recording and evoke potential stimulation were performed after dosing with Dexmedetomidine (50-500 μg/kg). During the entire baseline and evoke potential stimulation procedures, the oxygen support and warm waterbed were provided to keep the rats in stable condition. At the end of the recording procedures, an equal amount of Atipamezole was injected to reverse the sedative and analgesic effects of dexmedetomidine.

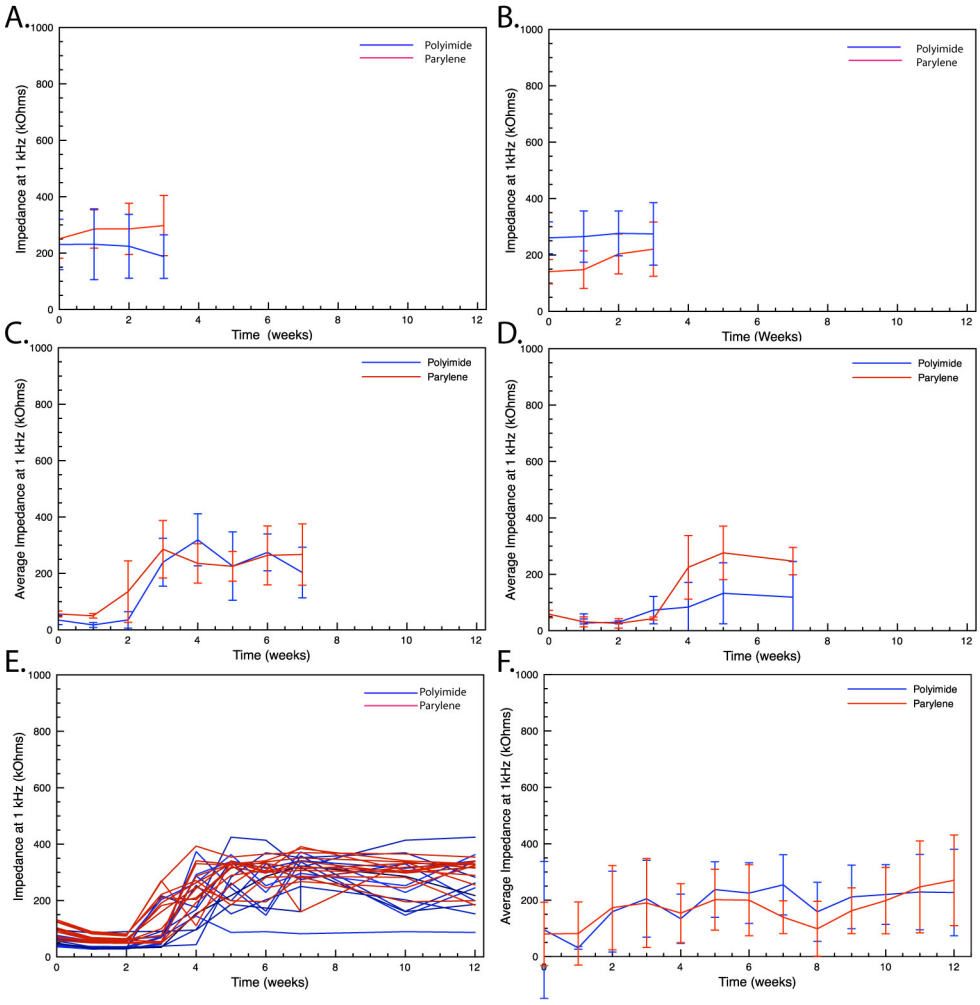

Figure 3.4: Post-operative impedance data at 1kHz of a number of rat (n=6). All 6 rats show an increasing trend of the impedance at 1 kHz starting from week 2, stabilizing after week 5. A. and B. Averaged impedance of the electrodes at 1 kHz over 3 weeks of M46 and M47, respectively. C and D. Average impedance at 1 kHz data of M26 and M27, respectively over 6 weeks. E. An individual electrode impedance plot of M25 shows that impedance over 12 week period was stable up to 2 weeks then reach the stabilized level after week 5. F. Averaged impedance at 1kHz of M26 over 12 weeks, showing similar trend to other rats. (The average data excluded some dead channels that failed due to the connector problem.)

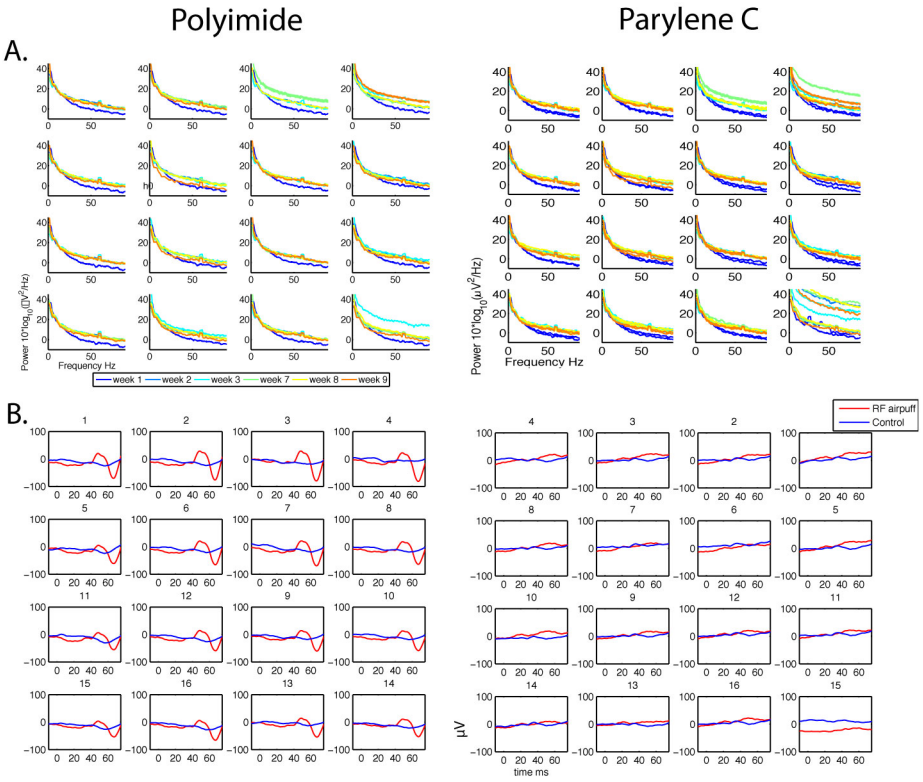

Figure 3.5: Power spectrum of baseline recording and evoked potential response from an rat M25. A. The power spectrum of 32 electrode sites on a polyimide and parylene electrode illustrating the slight power decrease particularly at a lower frequency ranges. The noise at 60 Hz is due to the absence of filtering. B. Evoked potential response of polyimide and parylene C devices using an air puff stimulation and control baseline recording in a rat after 2 weeks post-implant.

The baseline recording and evoke potential recording were performed using data acquisition system from TDT (Tucker-Davis Technologies, Alachua, FL). However, the evoke potential stimulation is performed by means of an airpuff stimulation on the rat paws using a digital dispenser (DX-250 series, OK International, Germany) with a setting of 20 psi and 40ms per pulse/puff. Figure 3.5A illustrates a slight decrease of power spectrum of the baseline recording from 32 electrode sites of polyimide and parylene electrodes representing the similar result in majority of the sites for over 3 months. Signal power spectrum is decreasing after 3-4 weeks corresponds to the slight increase of electrode impedances. The 60 Hz noise can also be observed because this data representing an unfiltered data. Post-mortem skull inspection also shows that thin layer of bone grows under the electrode arrays. This could well be the cause of impedance change. An example of evoke potential response of one rat (M25) at week 2 post-implant 3.5B shows that both polyimide and parylene electrodes can record the evoked potential response compared to the baseline control response. This is shown by the larger signal magnitude up to 100 μV on the contralateral cortex after foot stimulation. For comparing the encapsulating materials, the earlier results shown in Figure 3.5B is presented since at the early stage the electrode impedance across 32 channels are very similar (Figure 3.4A and B). Both power spectrum of baseline recording and evoke potential response from polyimide and parylene device show no significant difference.

Biological response

In-vitro cytotoxicity for polyimide and parylene C materials have been extensively studied [Richardson et al. (1993)], [Rubehn and Stieglitz (2010)], [Kamińska et al. (2009)], [Chang et al. (2007)], however it is relatively unknown if these models are predictive of the *in-vivo* response. In general, biological response of the surface electrode array is commonly thought to be minimal due to the relatively minimal invasive nature of the platform. Experimental evidence supporting this assumption will be presented in this section. In addition to the conventional immunohistological readout of the tissues underneath the electrode array, the realtime *in-vivo* vasculature and tissue response of the electrode array was monitored through the use of cranial window.

In-vivo window imaging for vasculature response observation

Micro-ECoG electrode is implanted on top of the dura; therefore it is often assumed that there is little biological reaction after a long period of implantation compared to the penetrating electrode. However, though the implant device material is a biocompatible and chemically inert, it is believed that an onset of Foreign Body Reaction (FBR) occurs due to the adsorption of the protein to the materials [Wilson et al. (2005)] as well as hypoxia. To verify the reaction of the brain to the micro-ECoG platform *in-vivo*, a cranial window was made for direct imaging the surface of the brain. Clear cranial windows enable both bright-field and fluorescence imaging as shown in Figure 3.6. An important factor controlling the composition of the adsorbed

layer is the hydrophobicity of the material [Tang and Eaton (1993)]. Since the polyimide surface has higher hydrophobicity than parylene C surface, I hypothesize that the adsorption of the proteins and antibodies that could initiate inflammatory process on the polyimide is likely to be higher than that on parylene C surface.

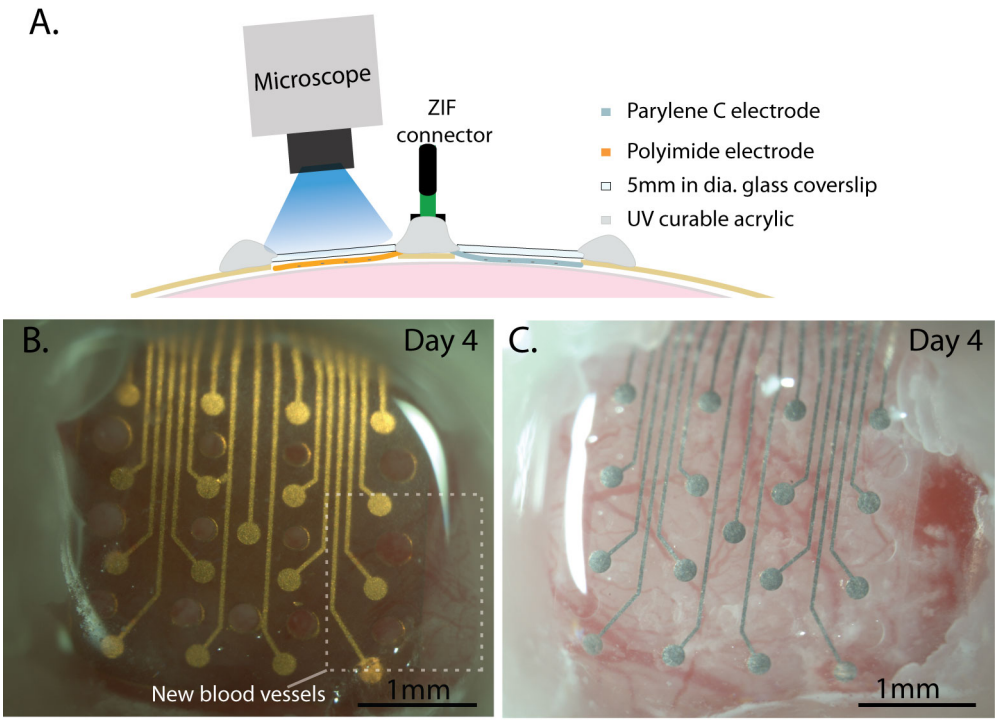

Figure 3.6: A. Cross section view of the cranial window and electrode implantation with polyimide on the left craniotomy and parylene C on the right craniotomy and covered with the glass coverslips. B. Bright field image of polyimide electrode array 4 days after implantation shows new blood vessel formation through the holes, particularly more on the lower right corner. C. No new blood vessels formation observed on the parylene C electrode 4 days after implantation.

Figure 3.6B shows that there was new blood vessels formed around the edge of the polyimide electrode array, particularly near the bottom right corner of the window. This formation of new blood vessels or angiogenesis is believed to be part of the progression of Foreign Body Reaction (FBR) [Luttikhuizen et al. (2006)]. The cranial window in Figure 3.6C clearly shows that the brain surface under the transparent parylene C electrode array has no visible biological reaction, such as new blood vessel formation, inflammation and bone growth 4 days after implantation. The red spot under the dura on the right of the electrode array in Figure 3.6C is not related to the electrode array as it was observed during the surgery and before electrode implantation. From this first stage of implantation, the appearance of the new blood vessel formation on the polyimide electrode array suggests that it has faster onset biological reaction than parylene C material. However, the vasculature formation observed is minimal as it does not promote thick scar tissues around the polyimide array. Compared to the penetrating electrode arrays [Williams et al. (1999)],[Grand et al. (2010)], this angiogenesis from the surface electrode array is minimal.

New blood vessel formation can be imaged clearly by staining the blood vessels with FITC Dextran. Under the blue light (approx. 450 nm), FITC emits green light as appears on the images shown in Figure 3.7. As mentioned previously, polyimide has some new blood vessels formed around the right edge of the electrode array (Figure 3.6B). Figure 3.7 A and C show clear evidence that there are new blood vessels formed not only around the edge of the polyimide electrode array at 4-day post implantation but they also grow through the 300 μm-diameter holes made for minimizing the electrode

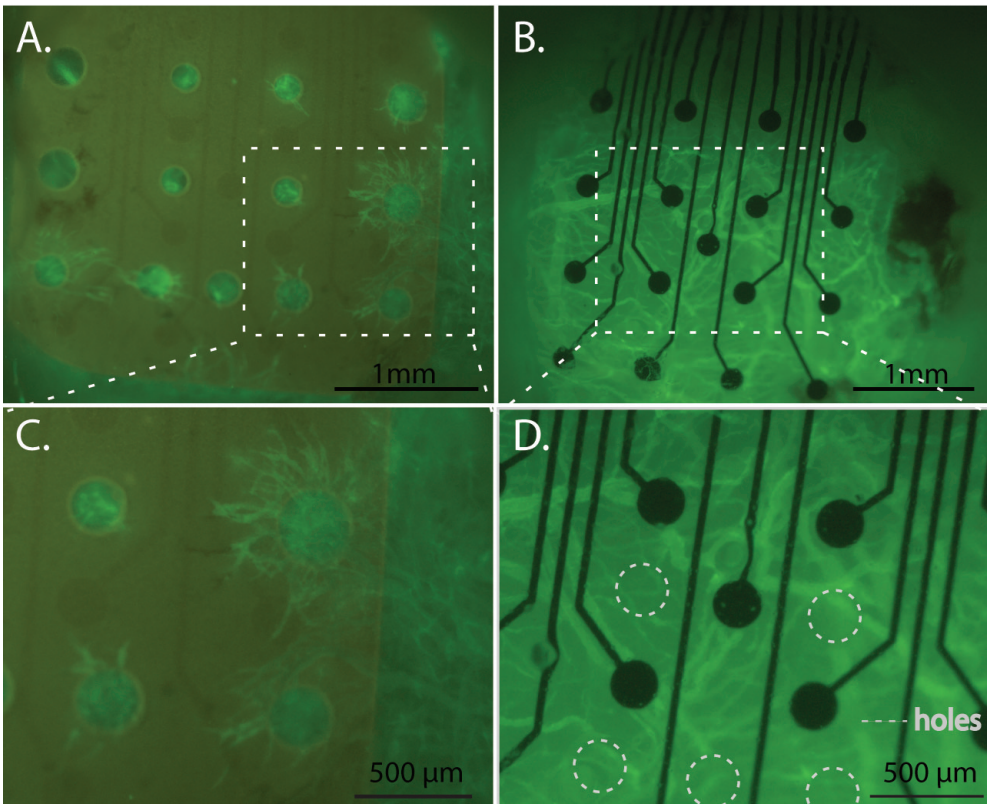

Figure 3.7: Vasculature response highlighted by FIT-C Dextran 4 days after implantation: A. and C. New blood vessel formation (shown in green) through every hole on the polyimide electrode array is easily observed, especially around the lower right corner of the array. B. and D. Parylene C electrode array has no visible new blood vessel formation through the holes or on top of the array observed after 4 days.

footprint and increase the ventilation. On the other hand, Figure 3.7C and D show no obvious angiogenesis on top of the parylene C electrode array. The blood vessels that are visible in Figure 3.7C and D are the preexisting blood vessels underneath the electrode array that can be seen since parylene C material is naturally transparent. At day 6 and 10 post implantation, the bright-field and fluorescence images of both polyimide and parylene C show that the formation of the new blood vessels has extended and become larger vessels (Figure 3.8A(i)). The white region on the right side of the polyimide electrode array also appeared to be uncalcified bone tissues upon closer inspection. This region has a large number of new blood vessels within the layers as shown in Figure 3.8A(ii). The early stage of angiogenesis on top of the electrode array was similar for polyimide and parylene C as new blood vessels grew through the holes of the array (Figure 3.8A(iii) and (iv)). However, angiogenesis of parylene C electrode occurred two days after noticeable vessels growth observed on the polyimide side. At day 10, both polyimide and parylene C electrode array were covered with uncalcified bone tissues (inside dashed line) approximately 70% of the entire window (Figure 3.8B(i) and (iii). The fluorescence images (Figure 3.8B (ii) and (iv)) confirm the existence of the blood vessels in the region believed to be bone tissue. After 3 weeks of implantation, the uncalcified bone regions shown in Figure 3.8B have become denser and thicker (Figure 3.9A and C). The blood vessels also appear to be denser as some of the blood vessels have become larger (Figure 3.9B and D).

Angiogenesis observed in this case perhaps is not only an indication of minor biological response to the foreign body but it could also be there

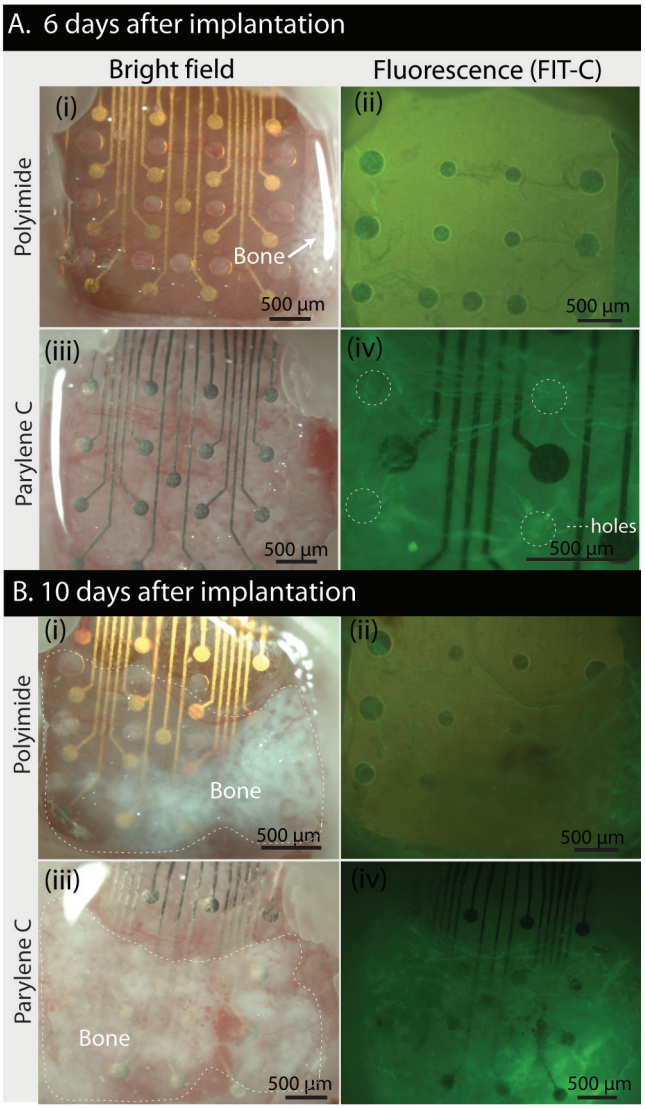

Figure 3.8: Vasculature response both bright field images and highlighted by FIT-C Dextran images 6 and 10 days after implantation. A. At day 6 after implantation A(i) and (ii) show more new blood vessel formation and some uncalcified bone growth on the right side of the polyimide electrode array. A(iii) and (iv). New blood vessels start to grow through the holes on the parylene C side at day 6 but considerably less than that on the polyimide electrode. B(i) and(ii). At day 10, the white uncalcified bone (inside dashed line) starts to cover approximately 70% of the polyimide electrode area. B (iii) and (iv). The parylene C electrode has uncalcified bone grows rapidly covering approximately 70% of the electrode area comparable to the polyimide electrode.

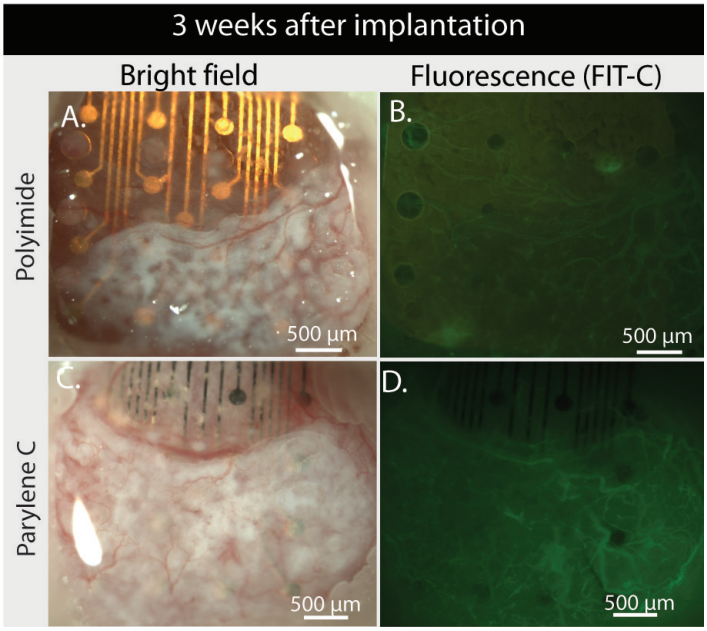

Figure 3.9: Both bright field images and highlighted by FIT-C Dextran images 3 weeks after implantation show thick bone layer covered almost 80% of the electrode array.

for supplying nutrients for the newly formed osteoblast layers. Although the bone tissue formation is undesirable for cranial window imaging the fact that there was bone layer forming on top of the electrode array does not deteriorate the electrode signal recording integrity. However, this thin bone layer also observed under the electrode arrays after a few weeks of implantation and will be discussed in the next section.

Histology and bone growth

Initial results show that the electrical aspects of both materials used for neural device development demonstrate similar results. This means the

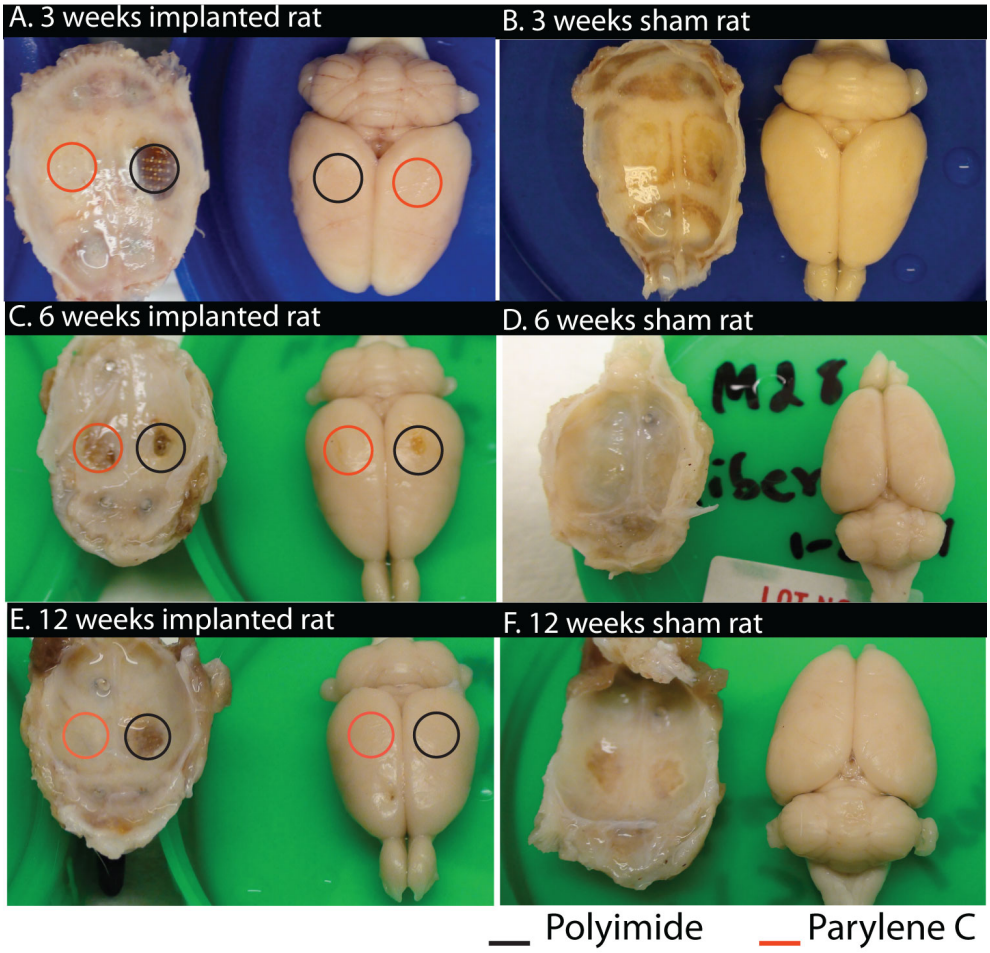

Figure 3.10: A. 3 weeks post-implant skull shows a thin layer of dura clearly under the polyimide electrode array; however the dura is not easily observed even though upon further inspection the thin dura also exists under parylene C electrode. C. 6 weeks post-implant (M27) skull shows a reduced craniotomy as the bone grew underneath each electrode. Smaller craniotomy on the polyimide side and noticeable marks in the brain can be observed. E.12 weeks post-implant (M25) brain shows no immediate distinctive signs of biological reaction but the craniotomy on both sides are completely closed as thin bone layer grew underneath the electrodes. B,C and D Control rats for 3, 6 and 12 weeks implantation show no immediate sign of reaction.

polymer degradation and electrode corrosion is not significant enough to create distinctive electrical property differences for each material. However, a more interesting finding resides in the biological response of the devices. Upon preliminary visual inspection, the brain surface under polyimide and parylene device appear to have some marks typical of bone growth on some of the rats as shown in Figure 3.10. This may suggest that polyimide and parylene C devices have different surface roughness, contact angle or molecular structure that could result in different bone growth rate. Since the number of animal used for this stage is small, solid conclusions on the encapsulation material effect can not be made yet. However, the thin bone layer was observed under both electrode arrays after 3-week implantation (Figure 3.10A) by visual and physical inspection. After 6 and 12 weeks of implantation, the bone growth has been completed showing craniotomies covered with a thin layer of bone (Figure 3.10C and E). The results from other 4 rats show the same trend (Images not shown). The control animals for the 3 time points indicate that there is no biological response created by the surgical procedures (Figure 3.10B, D and F. Further investigation was performed using histoimmunological identification for detecting the response of the astrocytes and microglia cells of these rats will be discussed further in the next section.

The expected astrocytes and microglia response after the chronic implant of the micro-ECoG device (3 weeks post-implantation) evaluated using immunohistochemistry techniques are illustrated in Figure 3.11. Fluorescent staining of astrocytes and microglia was performed with glial Þbrilliary acidic protein (GFAP) (Figure 3.11) and ionized calcium binding adapter

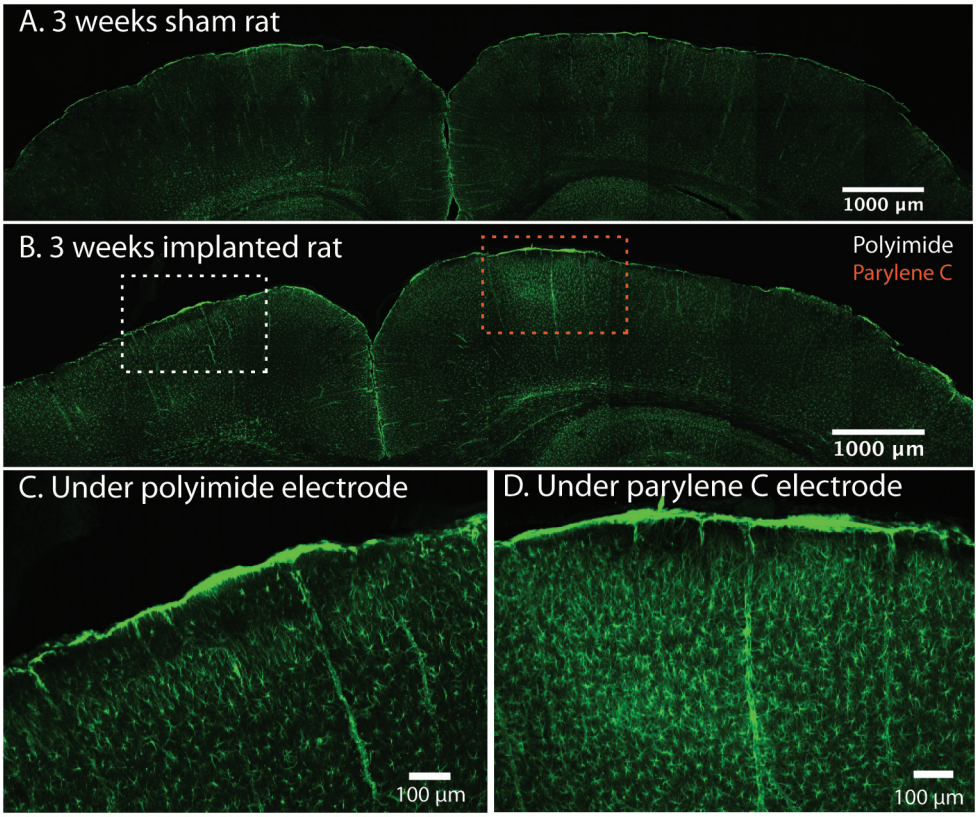

Figure 3.11: Immunohistochemistry images of labeled astrocytes from a rat brain after a 3-week chronic implantation with a polyimide and parylene C electrode from previous experiments. A. Astrocyte distribution imaged by staining for GFAP of a 3-week implantation control rat shows mild reaction of astrocytes underneath both craniotomies. B. Population of astrocytes underneath both electrode arrays is slightly less populated right under the electrode as some astrocytes may have migrated away from the foreign objects, indicating a mild astrocyte activation. Further away from both electrode array show a normal astrocyte distribution. C. A close-up image of the area under polyimide electrode array indicates that right under the electrode there is a 100 µm void region of astrocytes below the dura as they migrate to the next layer (100-200 µm) below the surface. which appears to have higher population of astrocytes. D. A close-up image of the area under parylene C electrode array shows similar distribution of astrocytes compared to the polyimide electrode side.

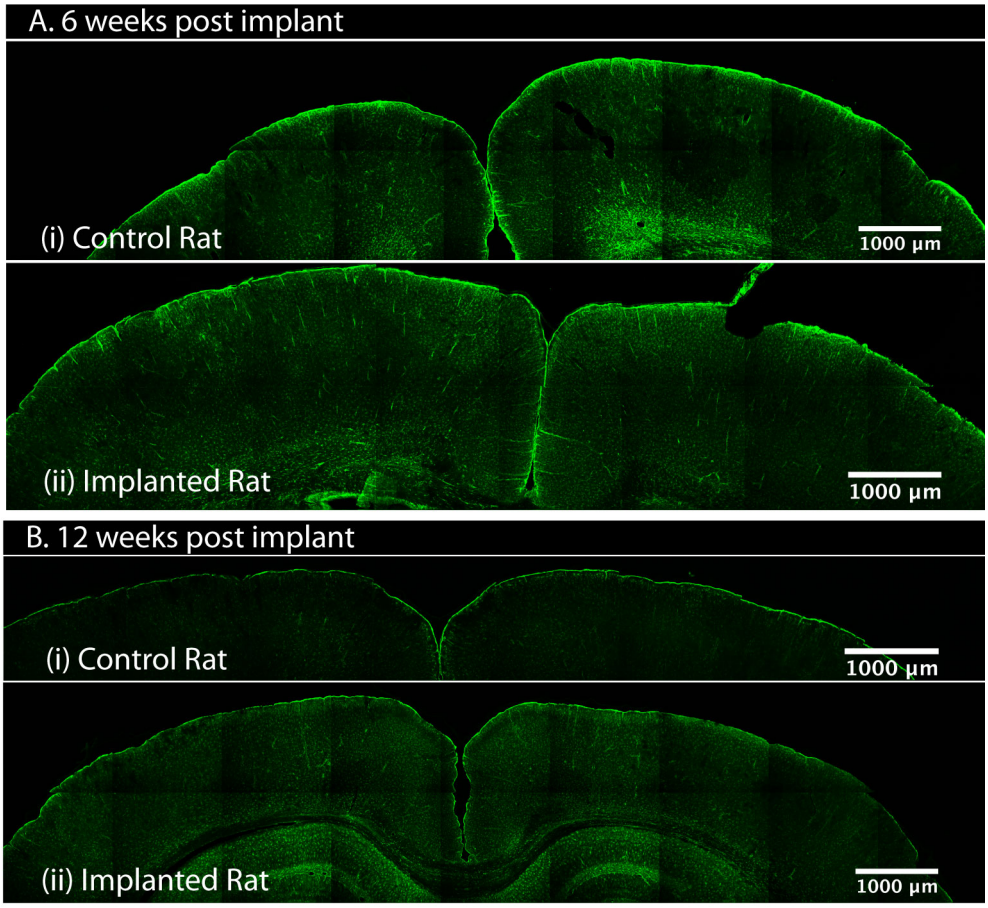

Figure 3.12: Immunohistochemistry images of labeled astrocytes from a rat brain after a 6 and 12 week chronic implantation with a polyimide and parylene C electrode from previous experiments. A. (i) Astrocyte distribution imaged by staining for GFAP of a 6-week implantation control rat shows mild reaction of astrocytes underneath both craniotomies. A(ii) Astrocyte reaction under the parylene C electrode array (left) has minor aggregation under the electrode area similar to the control in A(i). but under polyimide electrode array (right) is similar to the parylene C and control except some visible tissue damage due to the surgical procedures. B. Population of astrocytes underneath both electrode arrays after 12 weeks have similar results to both 3 and 6 weeks implanted rats.

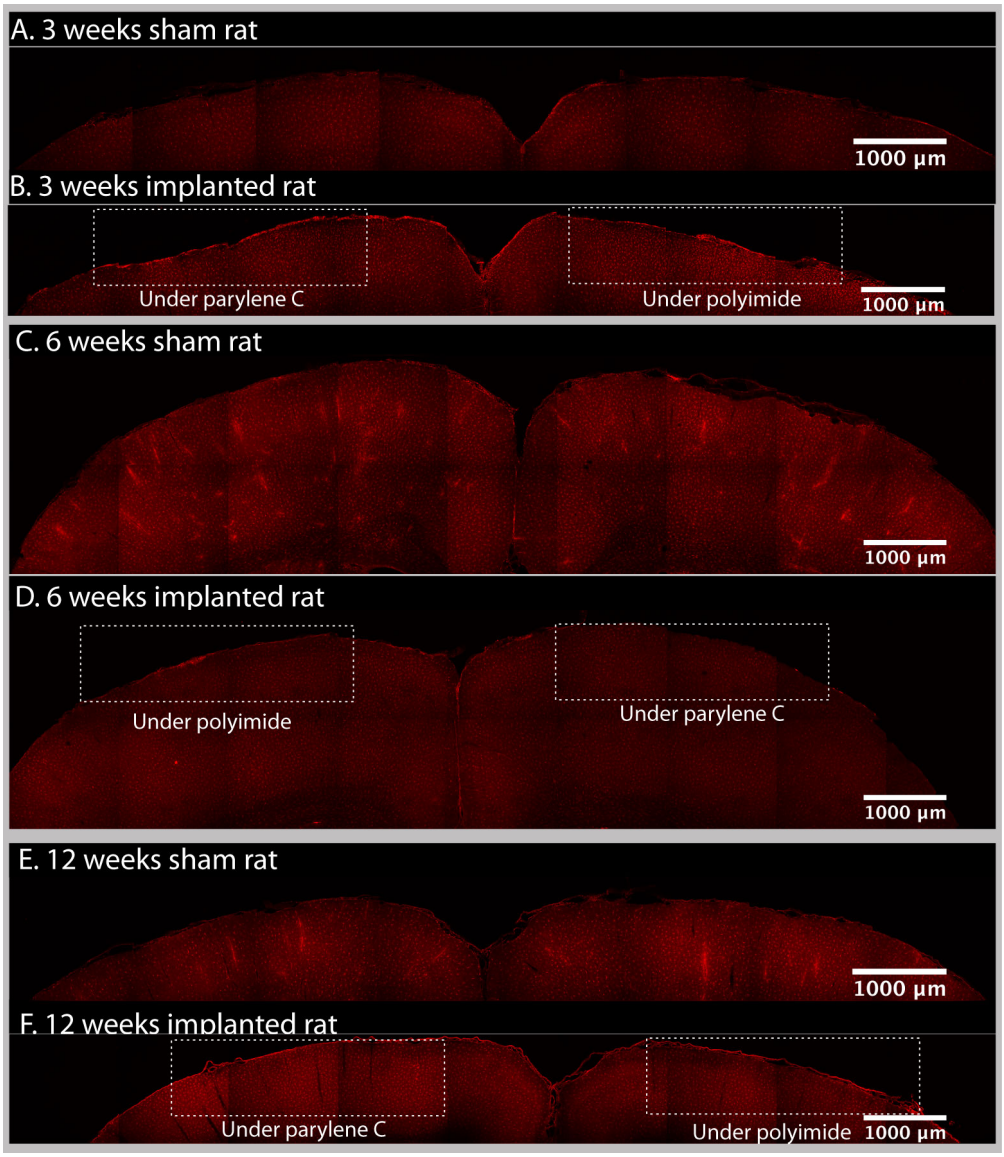

Figure 3.13: Immunohistochemistry images of labeled microglia from a rat brain after 3, 6 and 12 weeks of chronic implantation with a polyimide and parlene C electrode. A. Microglia distribution imaged by IBA-1 staining of a 3-week control rat implantation shows minimal microglia activation on both sides. B. Microglia distribution labeled with IBA-1 antibody of a 3-week implanted rat shows a minor microglia activation under the electrodes and the area further away from the electrode has relatively even distribution of microglia. C. and D. At 6 week after implantation, both control and implanted rats show minimal microglia activity under the craniotomies. E and F. After 12 weeks of implantation, microglia has relatively even distribution on both sides suggesting that the reaction to the foreign objects has been resolved.

molecule 1(IBA1) antibodies (Figure 3.13), respectively. The distribution of astrocytes appears to be higher in the area under the electrode than areas further away suggesting a mild astrocyte response but not sufficient to form the thick tissue scaring that is common for penetrating electrodes [Grand et al. (2010)], [Williams et al. (1999)], [Seymour and Kipke (2007)], [Seymour and Kipke (2006)] (Figure 3.11C and D). Microglia, however, appears evenly distributed in all areas (Figure 3.11). This results is expected because the microglia response usually occurs in the first two weeks and then resolves [Wirenfeldt et al. (2011)]. Seeing no abnormalities in microglia distribution and morphology after 3 months of implantation is a good indication of material biocompatibility and adaptation of the brain to the micro-ECoG device (Figure 3.12).

3.4 Conclusions

Finally, the properties of polyimide and parylene C can be summarized in Table 3.1. The chosen photodefinable polyimide material makes the fabrication process simpler and posses a good adhesion between each layer. However, at the end of the fabrication process the device releasing time is long (up to 5 hours). It also need 5 hours curing time at high temperature (375 degree celsius). On the other hand, parylene C does not require curing time and device releasing from the Si wafer substrate is instantaneous. The disadvantages of parylene C device are the development of adhesion problems, long deposition time and multiple steps of etching for patterning. By comparing only the fabrication process aspect, polyimide and parylene C have com-

parable advantages and disadvantages. The electrode electrode dielectric strength, moisture absorption, electrode impedance and biological reaction are comparable for both materials. The main distinct property of parylene C is its light transmittance that is superior to the polyimide; therefore parylene C is better for any applications that requires transparent material, such as cranial window imaging and devices for optical applications. For the device that will be exposed to high temperature (above 300 degree celsius), polyimide would be a clear choice. Moreover, parylene C is more versatile material particularly for micro-ECoG device than polyimide, especially for window imaging and optogenetic-related device.

	Polyimide Device		Parylene C Device	
Fabrication Process	Pros - Easily patterned - Controlled thickness - Good adhesion	Cons - High curing temperature - Long curing steps - Long device releasing time	Pros - Environmental friendly deposition - No curing needed - Instant device releasing - Controlled thickness	Cons - Long patterning/ etching steps - Adhesion problem
Tensile Strength	180 MPa		70 MPa	
Light transmission	Not transparent (brown)		Transparent (clear)	
Melting point	525˚C [(1)]		290˚C [(2)]	
Dielectric strength	345 V/µm [(1)]		220 V/µm [(2)]	
Moisture absorption	1 % [(1)]		0.06 % [(2)]	
Electrode Impedance (average at 1kHz)	30 kOhms		50 kOhms	
Biological Reaction	None significant reaction		None significant reaction	

Table 3.1: Summary table of the polyimide and parylene C properties,((1) HD microsystems, (2) Special coating systems)

4 CHRONIC IMPLANT STUDIES IN NON-HUMAN PRIMATE [1]

Electrocorticography (ECoG) has become an increasingly standard clinical tool that has also spurred experimental exploration. Clinically approved ECoG arrays are relatively large and new smaller scale devices (micro-ECoG) are being developed using a variety of fabrication methods, materials, and designs. Micro-ECoG arrays are poised to improve on both the degree of invasiveness and signal quality by utilizing flexible electrode deployment through smaller craniotomies and by increasing the spatial and spectral resolution with higher density and smaller electrodes. To date, these clinical devices have been built upon existing macro-ECoG platforms, and have not leveraged contemporary microfabrication processes. Electrocorticography (ECoG) allows reading cortical signals with a significantly better accuracy than previous technologies such as the EEG. As such ECoG has been envisioned as a powerful technique to improve the accuracy of Brain Computer Interfaces (BCI). ECoG has been used in both monkeys and human patients for many applications such as cortical mapping [Towle et al. (1995)], monitoring epilepsy [Iida et al. (2005)], [Blanco et al. (2010)], [Luther et al. (2011)], [Panagiotides et al. (2011)], spatiotemporal cortical mapping and monitoring during word repetition [Felton et al. (2007)], [Edwards et al. (2010)], [Pei et al.

[1] This chapter was adapted from the paper: "A micro- electrocorticography platform and deployment strategies for chronic bci applications", S. Thongpang, T. J. Richner, S. K. Brodnick, A. Schendel, J. Kim, J. A. Wilson, J. Hippensteel, L. Krugner-Higby, D. Moran, A. S. Ahmed, D. Neimann, K. Sillay, and J. C. Williams. *Clin EEG Neurosci*, 42(4):259 - 65, Oct 2011.

(2011)] and motor task control [Leuthardt et al. (2004)], [Pistohl et al. (2008)], Sanchez et al. (2008)], [Yanagisawa et al. (2009)]. The signal from an ECoG, can also be leveraged for developing brain-computer interfaces (BCI), such as controlling the P300 speller BCI [Brunner et al. (2011)], virtual keyboard [Krusienski and Shih (2011)] and BCI2000 software [Leuthardt et al. (2006)].

The ECoG provides a significantly higher signal to noise ratio and spatial resolution than the EEG as it benefits from a higher proximity of the intracranial electrodes to the cortical surface. However, the spatial resolution of ECoG due to its large electrode diameter (1-3mm) and inter-electrode spacing (1cm) does not meet the requirement to record higher frequency signals (>70Hz), known as higher gamma modulations analysis, during motor tasks. ECoG is made out of silicone material and only designed for short term implantation. Hence, micro-Electrocorticographic electrode array was developed in order to improve the spatial resolution of the ECoG as well as reduce the invasiveness of the device by shrinking its size. At the early stages, microscale ECoG was developed using wire-lead bundles cast in polymer mold and implanted in human subjects and successfully recorded the brain signal from sensorimotor cortex [Ohara et al. (2000)], [Leuthardt et al. (2009)] and Wernicke's area [Kellis et al. (2010)] for a short period of time.

Recently, thin-film micro-ECoG made of polymers such as polyimide and parylene were developed and tested in small animals and rodents [Takeuchi et al. (2005)], [Pellinen et al. (2005)], [Hollenberg et al. (2006)], [Henle et al. (2011)]. Furthermore, these thin-film MEMs-based devices have been implanted in monkeys and their chronic behavior is starting to be

characterized [Rubehn et al. (2009)]. One of the problems in monkey chronic implant studies for BCIs is the reliability issues inherent to the electrode chamber and connection scheme durability. As mentioned previously, other micro-ECoG arrays were not designed for a motor task control. In those experiments the monkey's head is fixed in a frame on the recording chair while their motor task behavior is monitored daily. To go through many of these sessions, the head chamber and the connectors for data acquisition have to be robust and maintain the signal recording capability. Also, as described in Chapter 2, these electrode arrays require meticulous hand soldering skill and a long assembly time. Another problem is the invasiveness of the micro-ECoG, although it is minimally invasive other research groups have used surgical techniques that require almost half of the skull to be opened. To minimize the invasiveness and the risk of infection, we have developed a novel electrode and head chamber that reduce the size of the craniotomy while providing sufficient electrode array coverage on the sensorimotor cortex for BCI applications.

While there have been a number of previous studies that have described several micro-fabrication techniques for producing micro-ECoG electrodes for high resolution mapping experiments [Viventi et al. (2010a)], there remain a number of hurdles towards the adoption of this technology in a clinical setting. In this chapter I will present the developments made to improve surface electrode technology, connection scheme and head chamber design in order to facilitate chronic implantation in the sensorimotor cortex. These studies were performed on rhesus macaques to demonstrate their potential for BCI applications. Issues of signal quality and reliability will also be

discussed as they are essential for the development of long-term implantable devices.

4.1 Electrode and chamber development

Standard ECoG fabrication, involving discrete electrodes and wires embedded in silicone, has been pushed to its practical limits in adapting to the micro-ECoG spatial scale [Kellis et al. (2009)], [Leuthardt et al. (2009)], [Blanco et al. (2010)], [Pei et al. (2011)]. Further advancements may involve bio-microelectromechanical systems (BioMEMS) [Rubehn et al. (2009)], [Hollenberg et al. (2006)], [Viventi et al. (2010b)], [Toda et al. (2011)]. Because the development of BioMEMS devices utilizes photolithographic techniques, many electrode variations can be produced in one batch, greatly reducing the time required for the development and testing cycle. In addition, to minimize the invasiveness of the implanting procedure, novel electrode and chamber designs are presented.

Using the ZIF-FPC adaptor board shown in Figure 2.4B (top contact FPC), we developed a novel design in which 32-electrode sites are facing outward and down onto the brain surface (Figure 4.1 and 4.2A,B and C). The micro-ECoG device forms a loop allowing for a solid and easy connection to the adaptor board, as well as the implantation by sliding the electrode array under the skull. The electrode site diameter and spacing are optimized to cover the sensorimotor cortex. The chosen electrode size were 500 μm in diameter with 3 mm spacing. However, the spatial resolution can be easily increased by using pre-amplifier headstage allowing for more input channels

and the corresponding ZIF-FPC adaptor board.

The electrode design shown in Figure 4.1A or its fully assembled form shown in Figure 4.2A leverages the hydrophilic nature of the polymer allowing the electrode to couple with the brain surface and allow small displacements without damage. Bending the legs of the device produce a small spring-force that help keep the device in contact with the dura or pia matter without breaking electrode contact with the brain surface. This is important for chronic ECoG monitoring, as in clinical applications the brain can move relative to the skull. The device presented in figure 4.1B utilizes the flexibility and robustness of polyimide and parylene C to create a large cortical surface contact area that can be slid under the cranium with the help of a stainless-steel wire. This approach allows to implant a relatively large device while minimizing the scope of the surgery required. With a small rectangular craniotomy (approximately 19mm x 10mm, Figure 4.3C), a 32-channel electrode array can be deployed to cover more than 160 mm^2. Using this electrode design technique it is straightforward to increasing the cortical monitoring area without extending the scale of the craniotomy. In addition, the fact that the electrode area is far from the craniotomy (Figure 4.2C and D), the risk of getting infection and biological reaction from the surgery procedures can be minimized.

The head chamber is another important consideration of a good chronic implantable device. A suitable chronic implant head chamber should be a closed architecture in which the entire craniotomy is covered and sealed to protect any possible infection in the wound edges or worse in the brain. Some research groups have been using a semi-closed design head chamber

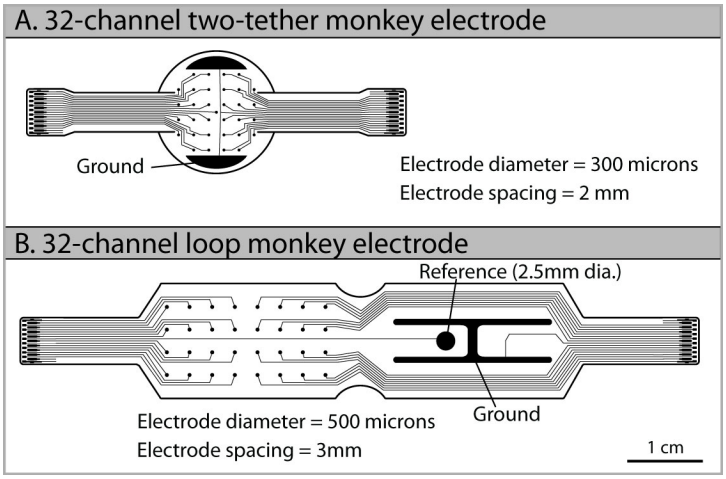

Figure 4.1: A. 32-channel two-tether monkey electrode design and B. 32-channel loop monkey electrode design

as the researcher can open and close the headcap when needed [Schmidt et al. (1976)], [Betelak et al. (2001)]. Although a headcap is acting as a barrier of the brain and outside environment, it is challenging to keep it completely sealed. More recently, a completely sealed head chamber for penetrating micro-electrode [Kipke et al. (2003)] was reported specifically for its reliability and clinical benefit.

In this section, I present two technologies for designing head chambers for chronic implants in rhesus monkeys. The first is applied for developing a head chamber for a short-term chronic implant (less than 3 months) and the second for long-term chronic implant (more than 3 months).

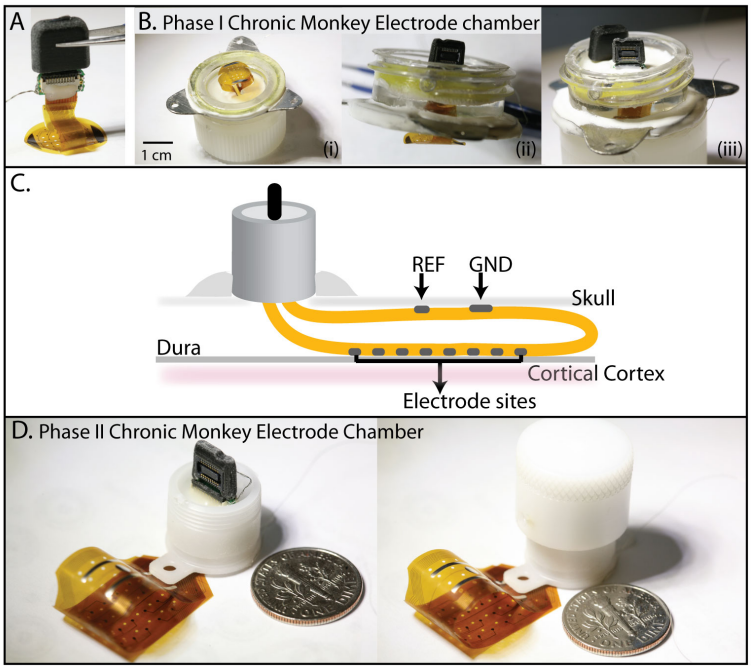

Figure 4.2: A. 32-channel electrode cable using ZIF-FPC adaptor PCB (top-contact FPC). B. Phase I head chamber for short-term chronic implant made from a PET plastic bottle neck and cap. C. Cross section illustration of the loop-electrode design implantation on the dura with minimal craniotomy. D. Phase II custom design head chamber for long-term chronic implant made from ACETAL plastic material

PET plastic head chamber design

The basic requirements of an acceptable chronic implant headcap material are excellent moisture barrier, lightweight, durable and biocompatible. Polyethylene terephthalate (PET) was chosen because of its appropriate size, durability and availability. Since this plastic is a clear thermoplastic that can be cut and modify easily, the head chamber for the initial tests (3 cm in diameter) was put together as shown in figure 4.2B. The electrode array and

connector are placed in the middle of the chamber and casted with the UV curable acrylic (Flow-IT ALC™) and silicone elastomer (Polydimethylsiloxane (PDMS), Slygard ® 184). By placing the electrode/head chamber on the craniotomy, the electrode is self-seated on the dura easily. To fix the head chamber on the skull permanently, a triangular-ring shape titanium sheet (0.125 inch thick) was added to increase the strength by fixing three bone screws through the holes on its tabs. Everything was then sealed with the dental acrylic to completely close the carniotomy. We have observed that this first design is only able to stay intact on a fully awake monkey behavior condition for around 2 months due to the failure of the screw tabs.

Custom design plastic head chamber

Subsequently, we modified the design of the head chamber and utilized a semi-crystalline material, ACETAL (DELRIN®), that provides high strength and stiffness with enhanced dimensional stability and ease of machining (Figure 4.2C). This material also characterized by a low coefficient of friction and good wear properties that are desirable for a chronic implant head chamber. The chamber was machined from a 3D CAD design (SolidWorks®), and designed to fit a ZIF-FPC adaptor PCB precisely at the center resulting in compact size head chamber (15 mm in diameter) as shown in Appendix C. Although, the dental acrylic provides an airtight seal, a chamber cap is also essential for keeping the electrode connector clean and safe inside the chamber (Figure 4.2C (right)). In addition, a set of small fixed screws on the cap was used to prevent the monkey from opening the cap.

4.2 Pre-Implant Impedance Testing

The impedance of the electrode has significant impact on the recording brain signal quality. An increase in impedance due to the changes in electrochemical phenomena, such as corrosion process or electrodeposition, at the interface between a metal and an aqueous solution as well as scar tissue formation, could reduce the recording signals [Williams et al. (2007)]. For these reasons, pre-implant impedance testing and weekly impedance measurements were performed to monitored changes in impedance of the electrodes. *In-vitro* impedance measurements were made with a two-electrode set up (with stainless steel counter electrode) using an Autolab potentiostat (PGSTAT12, Eco Chemie, Netherlands) in PBS solution. The impedance spectrum was measured at a range of frequencies from 100 Hz to 100 kHz, in logarithmic steps. The impedance of the electrodes used in these monkey chronic implants are ranging from 5-30 kOhms at 1 kHz.

4.3 Surgical techniques

Proper surgical technique, that minimizes stress to the animal, is important for its survival given the importance of the procedures perfromed. The monkey's vital signs have to be regularly monitored and recorded to reduce the chance of brain-damaged. An aseptic technique was applied throughout the surgery procedures in addition to thorough sterilization of the electrode array and surgical tools. By minimizing the craniotomy using the chamber and electrode array developed here, the risk of infection and mortality of the animal after the operation and operating time can be reduced.

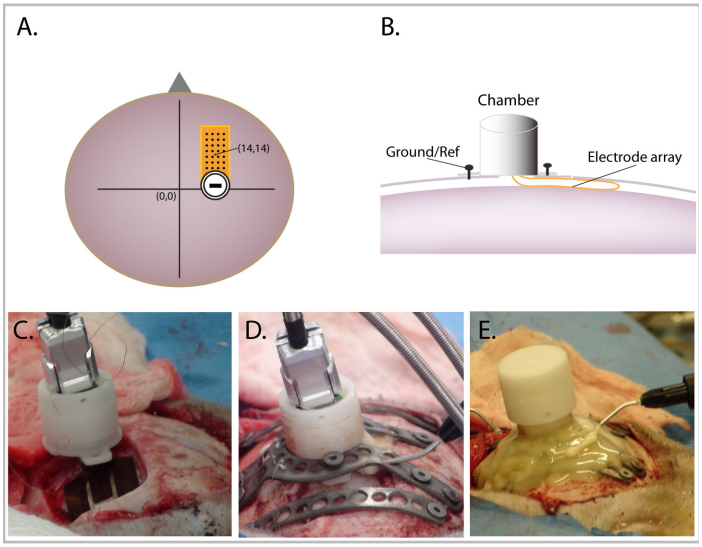

Figure 4.3: A. Top view diagram of an implant on the sensorimotor cortex of a rhesus monkey. B. Cross-section view showing the chamber and the electrode position. C. Rectangular craniotomy and electrode deployment under the skull. D. Placement of the head chamber and the titanium straps. E. Application of the dental acrylic to keep the head chamber sealed and fixed in place for long-term chronic implant.

Survival surgery procedures approved by IACUC were done in rhesus macaques (n = 3) using the electrodes and chamber designs shown in Figure 4.2 and the deployment method shown in Figure 4.3. Rhesus macaques were chronically implanted with a microelectrode array over the right sensorimotor cortex region, centered 14 mm anterior of the ear bar line and 14 mm laterally off the mid suture (Figure 4.3A). The monkeys were first anesthetized with Ketamine (10 mg/kg) for surgical preparations including vital monitor positioning and intubation. Isoflurane (0.5-5%) was used for anesthetic induction and maintenance during the non-recording parts of the procedure.

Following anesthetic induction, monkeys were placed into a stereotaxic frame, and the scalp shaved and prepped with alternating povidone iodine and alcohol. After the initial incision, exposed skull was cleaned and dried.

To obtain interoperative recordings, ketamine/fentanyl continuous rate infusion was initiated just before the skull was opened and isoflurane concentration maintained at 0.5% or less. A small hole was drilled through the skull until dura was exposed, and a stainless steel screw (size 4-40) was used for attachment of a ground wire. Then a rectangular craniotomy (19mm x 10mm) was made using a spherical burr (stryker) designed for use with a high-speed surgical drill (Figure 4.3C). After exposing the dura, the micro-ECoG array was inserted epidurally under the skull (Figure 4.3B) onto the sensorimotor area of the cortex. GelFoam (Pharmacia and Upjohn Co, New York, NY) was placed on top of the electrode to protect the device and the brain tissue. Titanium straps were then placed to hold the head chamber down and fixed with the bone screws (size 4-40) as shown in Figure 4.3D. Extra titanium straps were added on the surrounding area close to the head chamber and fixed on the skull with the screws to increase the strength of the acrylic cap. Finally, the edges of the head chamber base were sealed with the dental acrylic and then all the surrounding area (up to 5 cm around the chamber base) was covered with the dental acrylic (Figure 4.3E). After suturing the skin edges around the chamber base, triple antibiotic ointment was applied to reduce the risk of infection.

4.4 Long-term signal recording

Initial signal recording procedures were obtained using standard methods to elicit stimulus-evoked potentials, both interoperatively (as described above) and chronically. For chronic recordings, light anesthesia (Ketamine, 10-15 mg/kg) and pain relief drugs (Buprenorphine, 0.025-0.1 mg/kg) were administered for the procedure and electrical simulation evoked potentials were recorded. Multiple (n=60) short cathodic electrical stimulation (2 ms pulse) of current 2-4 mA was applied with 25 gauge needle electrodes. Neural activity was sampled at 3051 Hz using an RZ2 amplifier (Tucker-Davis Technologies, Alachua, FL). A band-pass filter was set at 0.1 to 200 Hz.

Longitudinal baseline recording for power spectrum analysis of the micro-ECoG over 23 weeks was performed. The power spectra of channels 1-16, within the area of interest for the foot electrical stimulation, are illustrated in Figure 4.4A. The power spectra of channels 17-32 also appear to be stable. Baseline recordings, evoked potentials and electrode impedance were obtained for 5 minutes weekly to ensure the long-term stability of the micro-ECoG device. The baseline power spectrum was stable in most of the electrode sites (Figure 4.4B). In sensorimotor rhythm, a mu band (8-12 Hz), beta band (18-26 Hz) and gamma band (>40 Hz) are present and can be recorded by the ECoG device.

With a 3 mm spacing, the non-human primate electrode arrays showed a distinctive evoked potential amplitude between adjacent electrode sites when the contralateral foot was electrically stimulated (Figure 4.4C). Higher

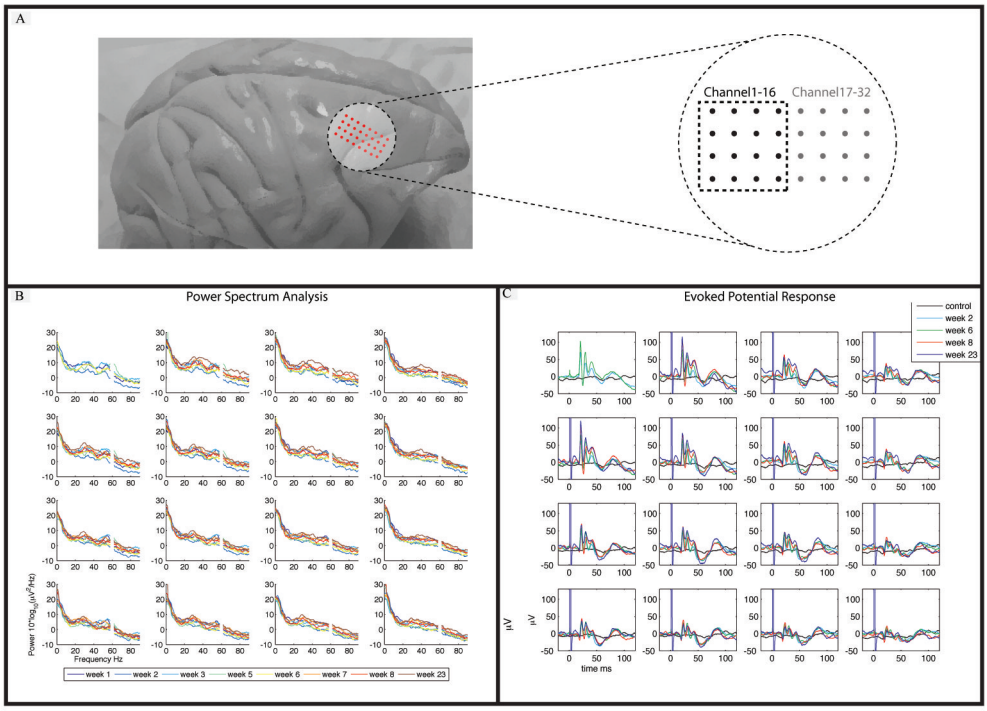

Figure 4.4: A. Position of the electrode array on the sensorimotor cortex of a non-human primate brain (Rhesus monkey). B. Power spectra of channel 1-16 over 23 weeks showing stability in long-term implant. C Evoked potential response after electrical stimulation (2.5mA) of channels 1-16 on the motor cortex of contralateral (left foot) compared to the control baseline recording for week 2, 5, 8, and 23.

evoked potentials were observed over the stimulated part of the cortex and then faded out slowly towards the anterior (channels 17-32). With multiple electrical pulse (2.5mA) stimulation, the evoked potential was observed up to 80 μV in amplitude, this was large compared to the control baseline recordings which were essentially flat. This demonstrates that the epidural micro-ECoG device we developed has an acceptable signal quality and a high spatial resolution, and does not have signal properties that are drastically different than what has previously been reported from both micro and macro electrode recordings.

Similarly the wavelet evoke spectrogram and evoked potential can be plotted on top of each other (Figure 4.5A and Figure 4.5B) for week 2 and week 23, respectively. Through the use of the same stimulating conditions, the high gamma band (>70 Hz) power is distinctively high within the stimulated somatosensory cortex (foot area) and fade out slowly toward anterior. This indicates that the electrode site size and spacing have acceptable spatial resolution. Currently several BCI applications rely on the change in power specific spectral bands associated with imagined motor movement [Felton et al. (2007)], [Wilson et al. (2006)], [Miller et al. (2007b)], [Miller et al. (2008)], [Wolpaw et al. (1991)]. Higher frequency power law range, χ (76-150 Hz [Miller et al. (2007a)]), has highest power in accordance to the stimulated cortex. This high frequency was reported to have highest classification percentage when performing the imagined hand and tongue movement compared to lower frequency bands [Miller et al. (2007a)]. In summary, the electrode array we designed is suitable for BCI application as it is capable of recording a good resolution of this high frequency band.

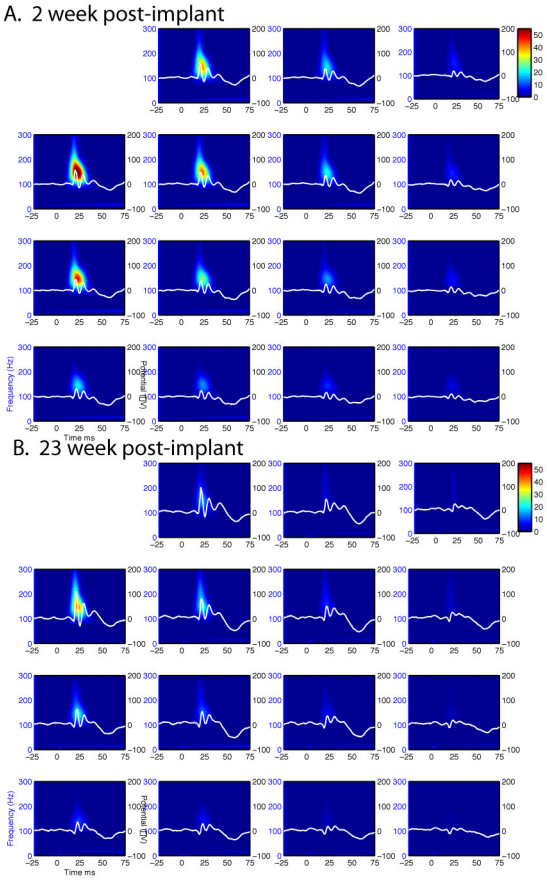

Figure 4.5: Wavelet evoked spectrogram of channel 1-16. A. After 2 weeks, an electrical stimulation on the contralateral foot shows good recorded signal quality with the evoked potential up to 80 μV and the wavelet spectrogram shows high gamma frequency (>70Hz) power is high at the upper left corner of the array (foot area on the cortex) due to the electrical stimulation. B. Evoked potential and wavelet spectrogram of 23 week post-implant have the same evoked potential level but reduce in high gamma power.

These chronic implant preliminary results using the electrode arrays and head chambers presented in this chapter demonstrate long-term signal recording stability in a chronic rhesus macaque model. The power spectra of the baseline recording and the evoked potentials of all sites were stable over 6 months (Figure 4.4B and C). Moreover, our collaborator, Prof. Daniel Moran and his team, in the University of Washington at St. Louis has implanted the micro-ECoG electrode arrays we developed in Rhesus macaques for at least a year with no complications. Before moving forward to clinical trials, an acceptable chronic implant electrode has to address issues related to biological response in long-term.

4.5 Biological Response

Micro-ECoG has gained more interest among the BCI community due to its minimal invasive and its robust signal quality. An important aspect for successful BCI device is a minimal biological response. In the previous section, I showed that the micro-ECoG developed present promising signal quality over a period of 6 months. At the end of the experiment, we collected the brain tissue of the primates in order to observe the biological response at a cellular scale using immunohistochemistry to identify astrocytes and microglia.

Tissues and immunofluorescence

The primate cortical brain tissue slices were acquired from a perfusion-fixed rhesus macaque tissue underneath the electrode area [4% paraformaldehyde

(PFA)]. All procedure was approved by Institutional Animal Care and Use Committee of University of Wisconsin-Madison. The primate brain was soaked in 4% PFA in PBS to fix overnight after perfusion and washed by soaking in HEPES in Hank Buffered Salt Solution with sodium azide. Brain was then sectioned at 80 μm using a vibratome and immersed in Hank balance salt solution (Sigma-Aldrich) with sodium azide (90 mg/L). Sections were then stained for GFAP (MAB360, Millipore) and IBA-1 (Wako) markers, for astrocyte and microglia expression respectively. Primary antibodies used were anti-GFAP (MAB360, 1:500; Millipore) and rabbit anti-IBA1 (1919741, 1:800; Wako). Sections were then incubated in secondary antibodies Alexaflour488 anti-rabbit (A-11008, 1:200; Invitrogen) and Alexafluor568 anti-rabbit (A-11036, 1:200; Invitrogen). Tissue slices were then mounted on glass slides (see more details in Appendix D).

Imaging collections and analysis

Tissue slice images were obtained from the multiphoton laser-scanning system built around a Nikon TE300 microscope (LOCI, UW-Madison). Emission wavelengths of 800 nm and 890 nm were used to image both fluorophores and magnification was set at a 10X objective. The images were selecting from the Z-plane that has the most expression of astrocyte and microglial cells. The GFAP stained tissues for astrocyte were imaged with PMT of 0.37 and IBA1 for microglia were 0.38.

GFAP expression highlights the astrocyte morphology and distribution under the electrode array (Figure 4.6). Qualitatively the astrocyte distribution appears to be normal along the cortical cortex, both under the electrode

array and further away from the device. Compared to the penetrating probe astrocyte distribution after chronic implantation in which astrocytes form scar tissue around the electrode [Williams et al. (1999)], [Kipke et al. (2003)], the astrocyte activity shown in Figure 4.6 is minimal after 6 months implantation.

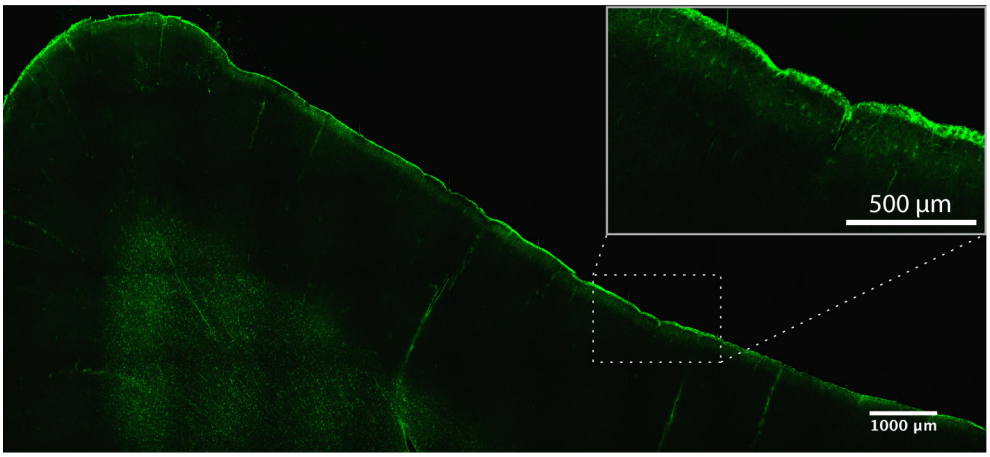

Figure 4.6: Astrocyte morphology (inset) and distribution of one example implant monkeys observed from GFAP antibody expression (green) appear to be normal, no scar tissue underneath the electrode array and uniformly distribution along the cortex after 6 months of implantation.

Microglia are the major glial cell type involved in wound healing response, contributing 5-10% of the glial cells in the brain [Ling and Wong (1993)]. These cells perform similar functions to macrophages in the neural tissue, and are recruited to the site of an invading foreign body to degrade it by secretion of enzymes or clear it through phagocytosis [Polikov et al. (2005)]. When

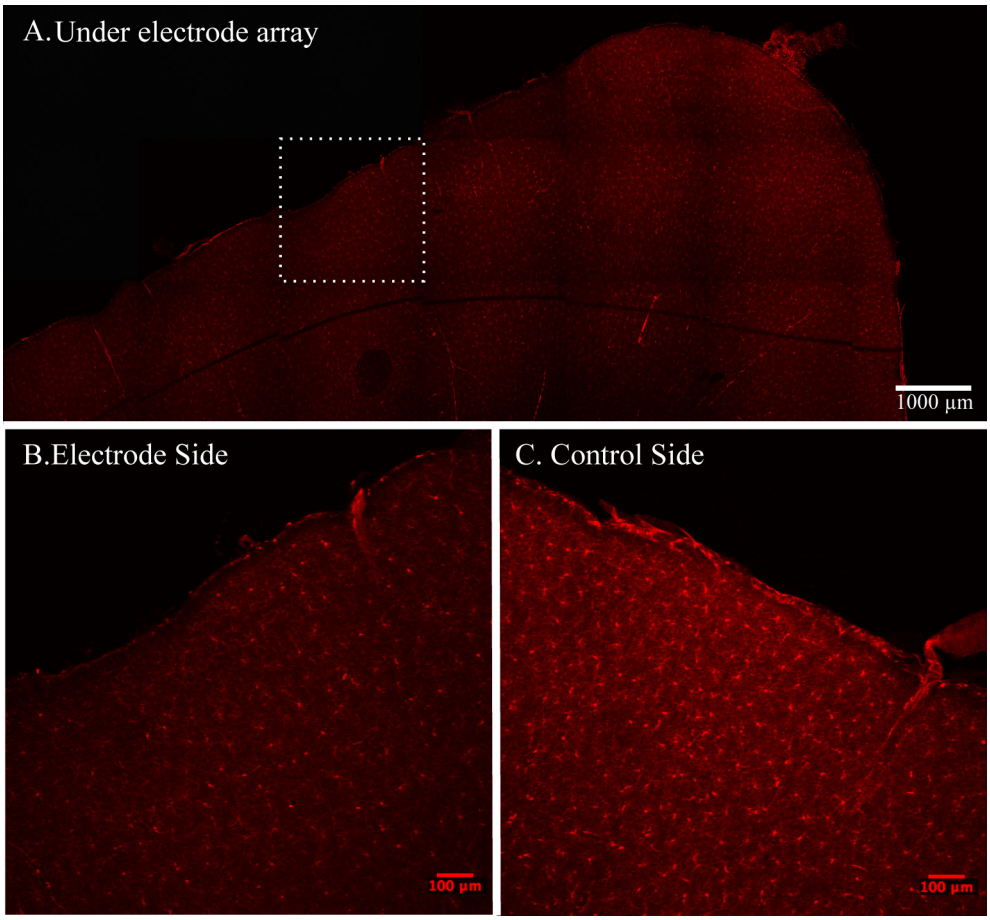

Figure 4.7: Microglia response to the injury due to surgical procedures and foreign body presence is minimal. A. Evenly distributed microglia is observed across entire brain section indicating inactivation state of microglia after 6 months of implantation. B. The close-up view inside dashed line in A. shows normal microglia morphology as they are in the highly branched state, not amoeboid like cells. C. The microglia morphology and distribution of the control side brain (contralateral to the implant) are similar to the brain section under the electrode array shown in A and B.

microglia are inactive, they display a highly branched state. When activated via an injury mediated mechanism, these cells become more compact and display an amoeboid morphology. Microglia distribution under the electrode array in Figure 4.7A is homogeneous, indicating that the presence of the electrode array does not activate the neural immune cells after 6 months of implantation. However, microglial cells are known to be activated by the presence of foreign body and traumatic injury during surgical procedures starting from the implanting procedure up to 6-8 weeks [Luttikhuizen et al. (2006)]. This may signify that the microglia were activated in early stages and returned to their normal state after several weeks. Closer inspection reveals that the morphology of microglia cells appears to be normal (Figure 4.7 B), in highly branched state, similarly to the microglia distribution on the control side (Figure 4.7 C). These results allows us to conclude that the electrode array induces minimal biological response, mainly due to two factors: a more suitable electrode material and the development of minimally invasive surgical technique.

4.6 Conclusions

The electrode performance during chronic implant in non-human primate shows good signal recording quality, stability and robustness. The micro-ECoG array we developed has shown good signal stability as the baseline power spectrum, evoked potential amplitude, and spectrogram power were not greatly reduced over at least 6 months. The head chamber design and connectors are also strong enough to sustain the weekly recording

sessions. Moreover, the biological reaction of the electrode array is very minimal with normal astrocytes and microglia morphology and distribution after 6 months. Longer term implantation and the use of our electrode array for controlling virtual robotic arms are currently under investigation. Preliminary results from Dr. Moran's laboratory suggest that the micro-ECoG platform developed allows a monkey to operate a virtual robotic arm with several degrees of freedom. These studies will be pursued further to develop tangible BCI applications.

5 MICRO-ECOG ELECTRODE OPTIMIZATION WITH OPTOGENETIC STIMULATION [1,2]

Progress in microelectrode development and optogenetics has enabled minimally invasive neural interfaces that have the ability to interact with the brain actively. This two-way interface could be used for the electrode optimization in order to obtain the best possible spatiotemporal performance. Recent advancement in optogenetics has lead the neuroscience community to new possibilities for optimizing devices and techniques for obtaining biological readouts and delivering cell type specific stimulation. The idea of individually controlling one type of cell in the brain has been suggested by Francis Crick since 1979 but has not been possible until recent advances that enabled to turn genetically modified neurons on and off in response to diverse color of lights [Boyden et al. (2005)], [Deisseroth et al. (2006)], [Zhang et al. (2006)], [Adamantidis et al. (2007)],[Gunaydin et al. (2010)]. New materials and microfabrication techniques have enabled the creation of micro-ECoG devices that are flexible and transparent, with a high density of electrode sites. These arrays with transparent substrates, and transparent

[1]This chapter was adapted from the manuscripts: "An optogenetic micro-ECoG neural interfaceÓ, Thomas Richner, Sanitta Thongpang, Sarah Brodnick, Ryan Falk,Amelia Schendel, Lisa Krugner-Higby, Ramin Pashaie, and Justin C Williams, submitting to Journal of Neuroscience.

[2]Parts of this chapter was adapted from the manuscripts: "Micro-electrocorticography Electrode Site Size Optimization with Optogenetic Stimulation", Sanitta Thongpang, Thomas Richner, Sarah Brodnick, Ryan Falk, Amelia Schendel, Lisa Krugner-Higby, Ramin Pashaie and Justin C Williams, in preparation for Journal of Neural Engineering submission.

metallization layers [Ledochowitsch et al. (2011)], have clear applications in for in vivo optogenetics.

Micro-Electrocorticography (micro-ECoG) was originally developed for recording brain electrical activity on the sub-millimeter scale, and it has been applied to many neural interface applications. Thin-film technology enabled flexible arrays with high channel count [Rubehn et al. (2009)], [Viventi et al. (2010a)], long term stability [Rubehn et al. (2009)], [Thongpang et al. (2011)], integrated circuits [Viventi et al. (2010a)], and degradable substrates [Kim et al. (2010)]. The smaller electrode sites and interelectrode spacing of micro-ECoG enable higher spatial and temporal resolution recordings. However, optimizing electrode site size and electrode site spacing is not straightforward, because the origin of the brain signal is not usually known precisely, even for sensory evoked potentials. Combining optogenetics with cranial window implantation is a promising approach for electrode site optimization, because it allows for precise spatio-temporal activation of specific groups of cells.

Many optogenetic animal models are now available including several microbial opsins and their engineered variants (see [Yizhar et al. (2011)] for review). These opsins vary in wavelength sensitivity, ion selectivity, conduction, and kinetics. Thus, the choice of the particular strain of mice depends entirely on the application [Mattis et al. (2012)]. While channels with fast off kinetics and high single spike reliability (e.g. ChR2/E123T [Gunaydin et al. (2010)]) would be well suited for intracortical electrode arrays to modulate multi-unit activity, channels with somewhat slower off kinetics (e.g. ChR2/H134R [Nagel et al. (2005)]) are expected to be a better

match with micro-ECoG arrays. One of the advantages of using slower off kinetics is the lower light requirements, as well as the ability to observe precise spatial patterns of neural activation and relaxation.

In this study, optical fibers and LEDs were used in combination with cranial window imaging techniques to determine the optimal micro-ECoG electrode site size and spacing. Optical fibers [Gradinaru et al. (2007)] and waveguides [Aravanis et al. (2007)], [Arenkiel et al. (2007)] have been employed previously for optogenetic applications. Technically, waveguides could be integrated with thin-film microfabrication, but high density optical connectors are difficult to fabricate. Alternatively, cranial windowing, a surgical technique in which the craniotomy is sealed with a small glass coverslip [Levasseur et al. (1975)], [Mostany and Portera-Cailliau (2008)] allows direct optical access to neurons on the cortical surface. Blue LEDs were combined with microscope optics to either broadly photoactivate the cortex under the entire window, or to focally stimulate small region of cortex within the window. Focal LED light was used at different brain surface locations to activate Channelrhodopsin-2 (ChR2) expressing pyramidal neurons while simultaneous electrophysiological recordings were made with a micro-ECoG array. Stimulating with external optics through the cranial window is a powerful technique characterize micro-ECoG performance in two spatial dimensions, but there has been recent interest to relate micro-ECoG signals to those deeper in the cortex. Deeper sources can generally be expected to have lower amplitude and broader spatial distribution due to the electrostatics of a distant source, so discriminating between multiple deep sources is generally limited by the signal to noise ratio. Therefore, it is also important to optimize

the micro-ECoG array with test signals at various depths. We used a LASER coupled optical fiber to stimulate various depths while recording from the micro-ECoG array.

5.1 Methods and materials

Mice electrode design

Custom micro-ECoG arrays were designed to meet the size constraints of chronic implantation in a mouse. To fully understand the relationship between the electrode size and its recording capability, three electrode designs, shown in Figure 5.1D, were fabricated using parylene C as the insulating substrate. Figure 5.1D(i) illustrates an electrode array of sixteen electrode site (150 μm in diameter) arranged in a 4x4 grid. This design has a 500 μm hole near the tip for optical fiber insertion. The photoelectric effect was determined using this array with equal site size and spacing. The second design (Figure 5.1D(ii) has the same metal electrode size but the sizes of the electrode openings are 200 (top row), 100, 150 and 100 μm in diameter, respectively. In this case, broad photostimulation was performed using a single bright LED placed 2-3 cm above the brain surface. The last design minimizes the electrode footprint and increases the area for optical fiber insertion for the focal photostimulation experiments. The masks required for photolithography fabrication process were designed with Adobe Illustrator and printed on with a high definition LASER printer.

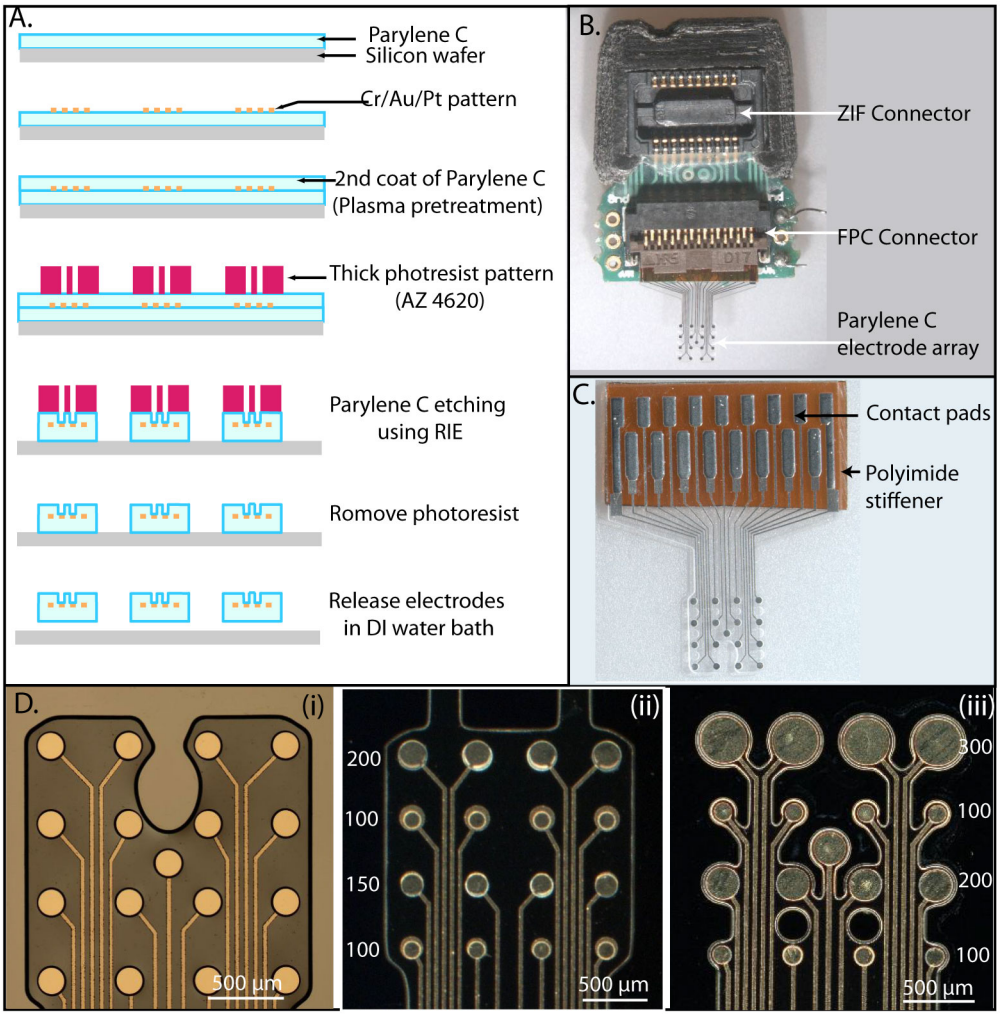

Figure 5.1: Mice electrode design and fabrication. A. Mice electrode fabrication process. B. Fully assembled micro-ECoG and Printed Circuit Board connecting the electrode array to the Flexible Printed Connector (FPC) and the Zero Insertion Force (ZIF) connector. C. An example of mice electrode designs bonded with thick polyimide adhesive sheet to fit the FPC connector. D. Three different mice electrode designs (i) an electrode with all electrode site size 150 µm in diameter, (ii) an electrode array with the same electrode size but with various electrode site opening, 100, 150 and 200 µm, (iii) a minimal footprint electrode array with various electrode site size (100, 200 and 300 µm in diameter)

Electrode fabrication

Micro-ECoG electrode arrays were fabricated using parylene C as a transparent flexible insulating material sandwiching the electrode sites and interconnecting metal layers. Similar to the electrode arrays designed for rat implantation shown in Chapter 2 and 3, parylene C arrays were fabricated by deposition of polymer layers using a chemical vapor deposition process, patterning by simple photolithography followed by oxygen plasma etching (Figure 5.1A). Parylene C was selected as a substrate for its optical transparent qualities. First a conformal layer of 15 μm of parylene C was deposited, followed by a photoresist layer. The photoresist was patterned using lithography techniques and several metal layers ((10 nm Cr, 200 nm Au, and 20 nm Pt) were deposited on top. After a lift-off process, the second parylene C layer of 10 μm was deposited on the entire wafer. Two 24 μm layers of AZ P4620 photoresist (AZ Electronic Materials USA Corp) were spun on the wafer and the electrode sites were defined. Openings in the parylene C layer were obtained using oxygen plasma etching (RIE Unaxis 790). Finally, the electrode arrays was released from the silicon wafer substrate in a water bath. A 175 μm thick polyimide adhesive sheet (LF polyimide sheet, Dupont) was cut with a cutting-plotter (Craft Robo Pro) and bonded under the contact pad area to add thickness and rigidity to the area which is required by the printed flexible connector (FH26, Hirose). The backing polyimide sheet was manually bonded with the electrode contact pad at 180 °C under 235 kPa pressure for 1 hour (Figure 5.1C).

The simple electrode assembly is the key feature of the double sided

Printed Circuit Board (PCB) with Flexible Printed Circuit (FPC) connector. The boards were designed with Eagle (CadSoft) and the surface mounted connectors were assembled (Imagineering Inc., Elk Grove Village, IL). The parylene electrodes with polyimide backings were inserted into custom PCBs being in physical contact with the FPC connector pins (Figure 5.1B). An FPC connector (FH26, Hirose) accepts the electrode via contact pads that are routed to a zero insertion force (ZIF) connector (DF30, Hirose). The ZIF connectors are designed to be compatible with Tucker Davis Technology amplifiers. This mechanical connection scheme was chosen due to the difficulty soldering platinum, and the desire to more rapidly assembly the electrodes. The electrode contact pads strengthen and assembly with the connector board can simply be done in about a minute. After assembly, the electrode impedance spectroscopy was used to ensure the electrical continuity and typical impedance values (e.g. 50-600 kOhms at 1 kHz)at every site prior to implantation.

5.2 Cranial window implantation

All procedures were approved by the University of Wisconsin School of Public Health and Medicine Institutional Animal Care and Use Committee. The initial approach was to implant a micro-ECoG array under a cranial window (Figure 5.2A and B.) in optogenetic mice. Transgenic mice were chosen over transfection methods for greater and more uniform expression levels. The H134R variant of Channelrhodopsin-2 (ChR2) was chosen for its longer off kinetics [Mattis et al. (2012)], [Gunaydin et al. (2010)], [Nagel

et al. (2005)], reducing the amount of excitation light required. While other opsins (e.g. ChETA) may be best suited for modulation of single spikes [Gunaydin et al. (2010)], H134R is a good choice for LFP modulation [Mattis et al. (2012)]. Guoping Feng *et al.* developed several ChR2/H134R mouse lines [Zhao et al. (2011)] and generously donated them to Jackson Labs. Five male mice from the Thy1-ChR2/H134R (Jackson Labs Stock no. 012350) line and one wild type mouse (control) were used in this study.

The night prior to surgery and an hour before the surgery, dexamethasone was given (2 mg/kg) to prevent cerebral edema. Buprenorphine (0.05 mg/kg) and ampicillin (100 mg/kg) were given 30 minutes before surgery, and glycopyrolate was given at the beginning of the procedure. Isoflurane (1.25-2.0% in oxygen) and midazolam (0.25 mg/kg) were used during surgery to maintain anesthesia/analgesia. Anesthesia depth was monitored with toe pinch and by counting the respiration rate, and a water heating pad was used to maintain body temperature.

Surgery was done using aseptic technique with sterile instruments and supplies. Implantation was similar to the rat surgery described in Chapter 3 with some modifications specific to mice and cranial windowing. The mouse was shaved, and the surgical site was cleaned with iodine and alcohol. After draping, an incision was made over the calvarium to expose the bregma and lambda sutures, and the connective tissue was removed with cotton swabs to expose dry bone. Then a titanium frame was mounted onto the skull the superglue. Once the glue was dry, the titanium frame carefully was mounted on the fixture with screws. UV acrylic (Fusio by Pentron) was then applied in front of bregma, behind lamba, and around the periphery of exposed

bone. A drill (myNeuroLab) was used with a burr (#105 and #106 Dremel) to thin an area of bone, and to create a craniotomy for the electrode array. The electrode was lowered onto the dura with a stereotaxic electrode positioner. With the electrode in place, a round piece of cover glass 3 mm in dimater (Warner Instruments) was placed over the craniotomy, and the cover glass was encircled with small pieces of gel foam. A small piece of drape was used to occlude the window while UV acrylic was applied around the edge of the glass and up to the connector. Once the electrode and connector were stable, the electrode positioner was removed. The gold ground/ref wire was coiled and implanted over an area of thinned skull, similar to that used for thinned skull in vivo imaging. The bone was thin enough, and the area of the coiled wire was sufficient, to provide a low impedance ground. To keep the ground in good contact with the underlying thin skull, the ground/ref coil was placed under the extra parylene C device. The ground/ref was covered with a piece of gel foam and sealed UV acrylic (Figure 5.2A). The subject was then recovered while maintaining supplemental oxygen and heat, and initial recordings were made.

For the focal stimulation with an optical fiber experiment, terminal surgery was required according to the protocol. The terminal surgery was started with the same procedures as the survival surgery except the anesthesia was switched from isofurane to ketamine (50 mg/kg) and dexmedetomidine (25 μg/kg), because isoflurane causes irregular brain signals. The ketamine and dexmedetomidine were redosed (25 mg/kg, ketamine and 12 μg/kg, dexemedetomidine) every hour. Once all the recording procedures were done, the mice were euthanized by an IP injection of Pentobarbital 120mg/kg

or commercial euthanasia solution with 5% Isoflurane.

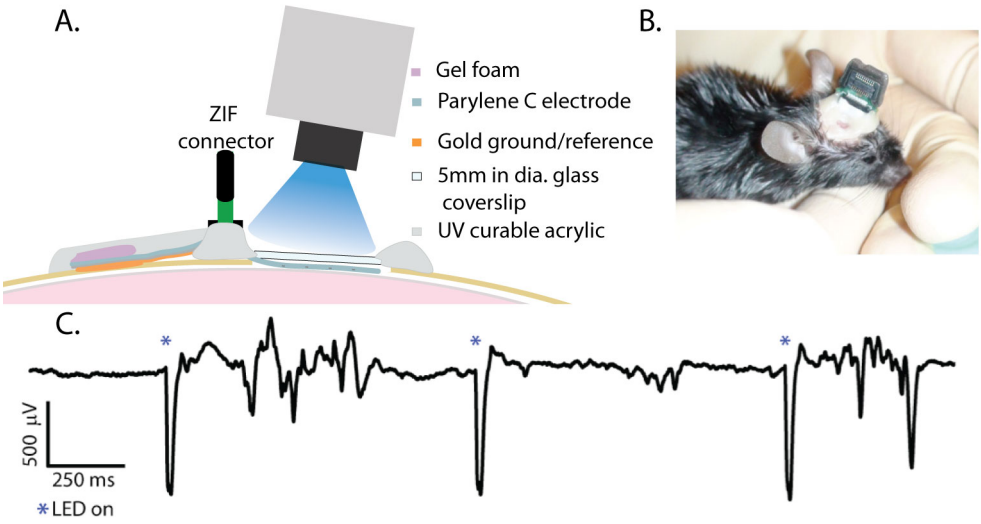

Figure 5.2: Cranial window implantation. A. Cross section window implantation. B. Cranial window on a live mouse. C. Short 5ms pulses of blue light on the cortical surface reliably evoked large negative deflection in the micro-ECoG signal through the cranial window.

5.3 Electrophysiology

This section comprises of two photostimulating paradigms; first was the surface broad stimulation using bright blue LED and the second was focal stimulation with either focused LED beam or optical fiber coupled laser source.

Surface stimulation

Local field potentials (LFPs) were recorded from the micro-ECoG array while pulses of blue light were applied through the cortical window. For electrophysiology sessions on the days subsequent to implantation, the mice were sedated with ketamine (75 mg/kg) and dexmedetomidine (25 μg/kg), and supplemented with oxygen and a heating pad. A Tucker-Davis Technologies system (RZ2/PZ2) was used to sample the signals at 3 kHz and to generate the LED control signal. A blue LED (Cree RGBW MC-E Star) was positioned 2 cm from the cranial window (Figure 5.2A), and the voltage control signal was converted into a constant current pulse (0-1000 mA, 0.5-12 ms) with a BuckBlock LED driver (LEDdynamics, Randolf, VT), and the LED output waveform was verified with a photodiode and oscilloscope.

Single pulses blue light were applied broadly to the cortical window every 750 to 1000 ms. The pulse duration was varied from 0.5 to 5.0 ms, the intensity was varied from 20 % to 100% of 32 mW/mm^2. These stimulus parameters were combined and randomly interleaved for presentation to the subject. All photostimulation was performed with the animal's eyes blocked to prevent the visual evoked response.

The LED beam was also focused to a point approximately 200 μm across through the microscope (115x) for surface focal stimulation (Figure 5.5B). The focal point on the brain surface was shifted easily by moving the mice on the microscope x-y stage. Evoked potential responses resulting from the two stimulus levels (0.44 A and 1 A applied to the LED) with 3ms pulse duration were acquired at multiple locations on the electrode array.

A set of control experiments were conducted to verify the optogenetic origin of observed signals. The cranial window was occluded with a black piece of tape to test the necessity of light through the window. This control was used to rule out visually evoked potentials and electromagnetic noise from the LED circuit. The photoelectric effect was addressed by implanting and testing a wild type mouse lacking the optogenetic gene and by applying the broad photostimulation to the cranial window 15 minutes after the animal had been euthanized.

The micro-ECoG signals were initially recorded with no digital filtering, and later processed in Matlab. The only filter applied was a 500 Hz low-pass FIR (order 25, applied forwards and backwards to preserve phase). Multiple trials were averaged to generate event relate potentials for Figures 5.8.

Focal depth stimulation

The signal recording performance of each electrode size was determined by focal stimulation near each site with the blue LASER (473 nm) coupled with an optical fiber (Figure 5.5A and B). The optical fiber was fixed to a steotaxic probe inserter (myNeuroLab) with a digital micrometer for precise insertion depth. Before inserting the optical fiber either through the holes or the brain surface (depth = 0 mm) near the electrode array, the evoked potentials responding to 3 ms pulses of photostimulation at many locations near the electrode sites were recorded. Subsequently, the optical fiber was inserted and recorded the evoked potentials at multiple depths (0 - 3 mm, in 0.15 mm increments). At the end of the depth stimulation procedure, the mice was euthanized with an IP injection of Pentobarbital 120mg/kg

or commercial euthanasia solution. Then the post mortem control was performed 15 minutes after euthanasia to rule out the photoelectric effect and electromagnetic noise.

5.4 Results

To figure out the correlation between the electrode site sizes and their recording capability, we recorded the local field potential caused by the broad or the focal LED light stimulation and focal laser stimulation. Our hypothesis was that the size of the electrode site does would not affect the recorded potential amplitude if the headstage amplifier had high input impedance. Given our amplifier's input impedance of 10^{14} ohms, we expected that electrodes with impedances anywhere in the kOhm range would equally be able to record the brain activity. To test this hypothesis, electrode designs with one electrode site size or multiple site sizes (Figure 5.1D) were used.

Broad surface stimulation results

In this section, the cortical response due to a broad light stimulation that covered the entire electrode array will be discussed. The brain activity with no stimulation applied was recorded and presented in (Figure 5.3A). This baseline activity shows that the larger electrode sites (200 and 300 μm in diameter with average impedance less then 300 kOhms at 1 kHz) had lower high frequency noise than the smaller sites (100 μm with the impedance of 600 kOhms at 1kHz on average). Figure 5.3B clearly shows the elevation of high frequency noise in the range above 150 Hz of the electrode size

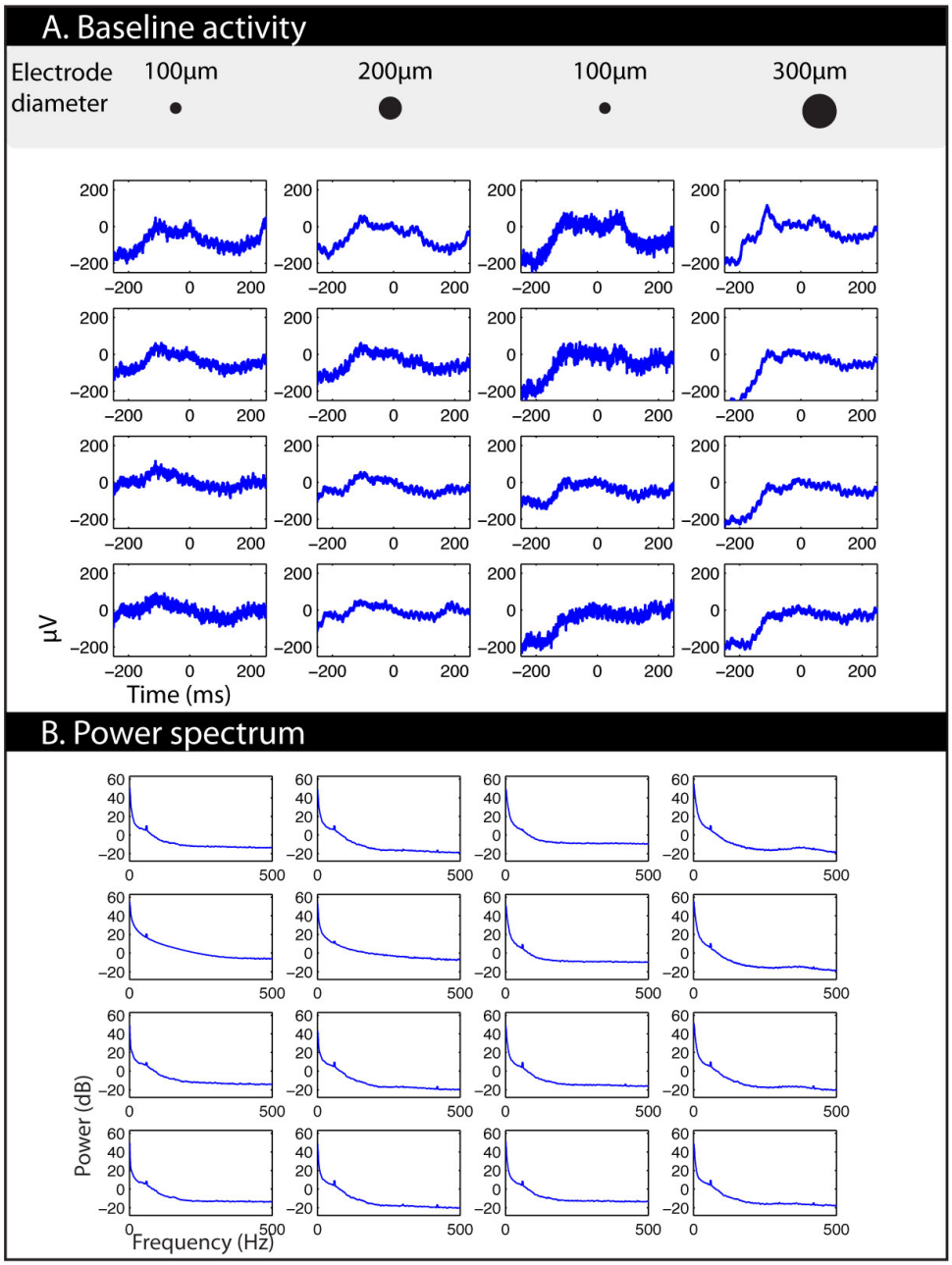

Figure 5.3: Baseline recording and power spectrum of different electrode size array. A. Baseline recording. B. Power spectrum of the baseline recording indicates higher noise floor (approximately 8dB higher) for the smaller electrode size (100 µm, column 1 and 3).

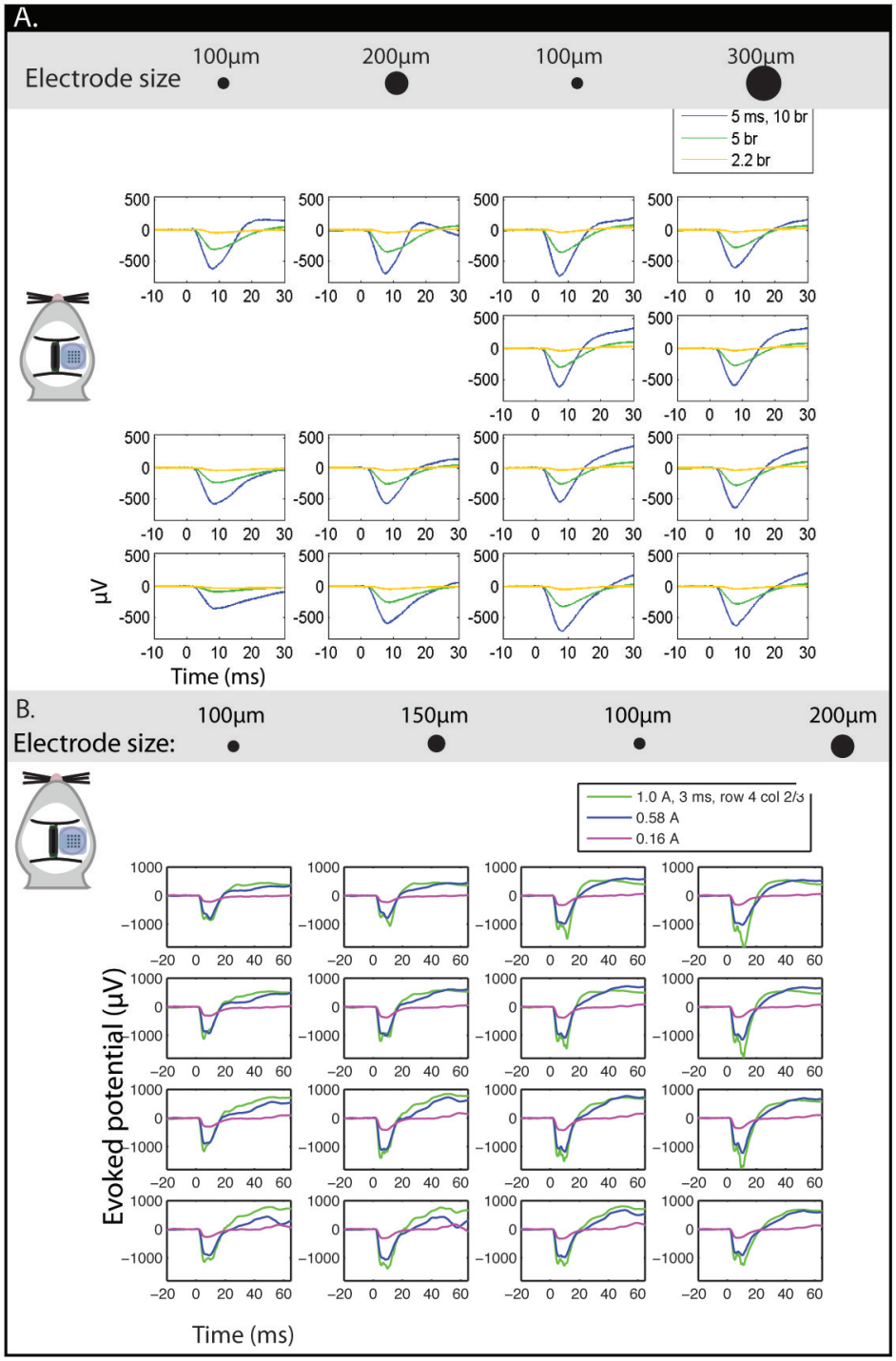

Figure 5.4: Broad LED pulses of 5ms at 22, 50 and 100% brightness. A. and B. Average evoked potentials recorded from electrode array comprised of multiple electrode site sizes (100, 150, 200 and 300 µm).

100 μm (column 1 and 3) which presumably relates to the high electrode impedance. However, the frequency range below 150 Hz appears to have similar power to the large electrode sites. This suggests that the evoked potential amplitude may be similar for all different electrode sizes. The level of high frequency noise may be important, because high gamma ECoG activity has shown utility in a number of BCI applications.

Further investigation of electrode performance based on electrode site size was done employing optogenetics to evoke a similar cortical response across and under an electrode array with multiple site sizes. Light pulses from an LED were broadly applied with relative intensity levels of 5, 44 and 100 % (Figure 5.4) through the cranial window. At full brightness (32 mW/mm^2), a 5 ms light pulses evoked approximately 600 μV depolarization across the array regardless of the electrode size. The onset of the depolarization was rapid and persisted briefly after the light was turned off, consistent with ChR2 mediated activity. These equally large local field potentials recorded from different electrode sizes as shown in both Figure 5.4A and Figure 5.4B support our hypothesis that the site size has little correlation to the LFP amplitude. Although high light intensity (1 A in Figure 5.4B) evoked a second negative peak at 12 ms which appear to be higher in column 4. The slightly higher depolarization found in that column was perhaps due to the experimental setup which allowed slightly more light shined on that area.

Focal stimulation results

Broadly applied light pulse stimulations have shown little relationship between the evoked response amplitude and the electrode size. The only

observable differences among the different electrode site sizes was the high frequency noise floor which was greater for the small electrode sites. We extended this investigation to focal stimulation with either light from an LED focused through a microscope or light from a LASER coupled optical. Focal stimulations at multiple locations were obtained by using the focused LED beam though the 115x microscope (Figure 5.5). The evoked potential amplitudes were higher near the stimulus and were comparable for both 100 and 200 μm electrode size. This result also supported our hypothesis that electrode size does not affect the evoked potential amplitude.

Focal sitmulation with a LASER couple fiber positioned allowed us to determine the recording capability of different electrode site sizes both at the brain surface and at multiple cortical layers. At the brain surface, we stimulated focally near each electrode size (row 0) starting from column 1 to 4 (Figure 5.6B). Similar peaks were recorded when we move the optical fiber close to each electrode size. This set of results also suggests that the recorded potential amplitude does not depend on the electrode size.

We then tested the ability of electrode sites of different sizes to record signals originating deeper within the cortex. The optical fiber was inserted incrementally and multiple photostimuli were applied at each cortical layer. For this depth focal stimulation, we used a minimal footprint micro-ECoG array that has larger area for optical fiber insertion as shown in Figure 5.1D(iii). Additionally, inserting the fiber below the array, as opposed to stimulation from above the array, eliminates diffraction and occlusion effects due to different metal site sizes and interconnection traces. The plots shown in Figure 5.7 were the results of the optical fiber inserted at row 0, column

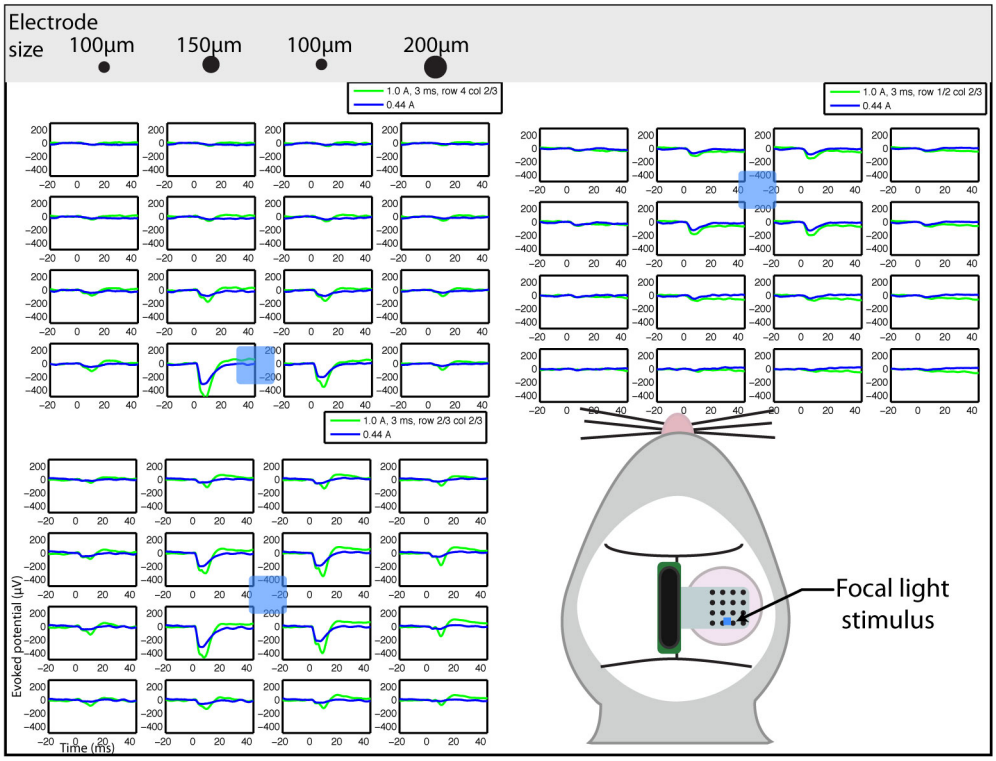

Figure 5.5: The focal LED light stimulation at different locations shows comparable evoked potential amplitude near the stimulated area between the two different electrode sizes.

3 at multiple depths (0-3 mm). At every cortical layers presented in this figure, equivalent signal amplitudes were recorded near electrode sizes 200, 100 and 300 µ in column 2, 3 and 4, respectively. As expected, the recorded evoked potentials from deeper cortical layers were smaller and spread more broadly than the shallower cortical layers. The difference in recorded potential amplitude followed spatial trends (sites nearest the fiber had larger amplitidues) more than any trend due to electrode site size. Again, there was no apparent relationship between the electrode site size and the

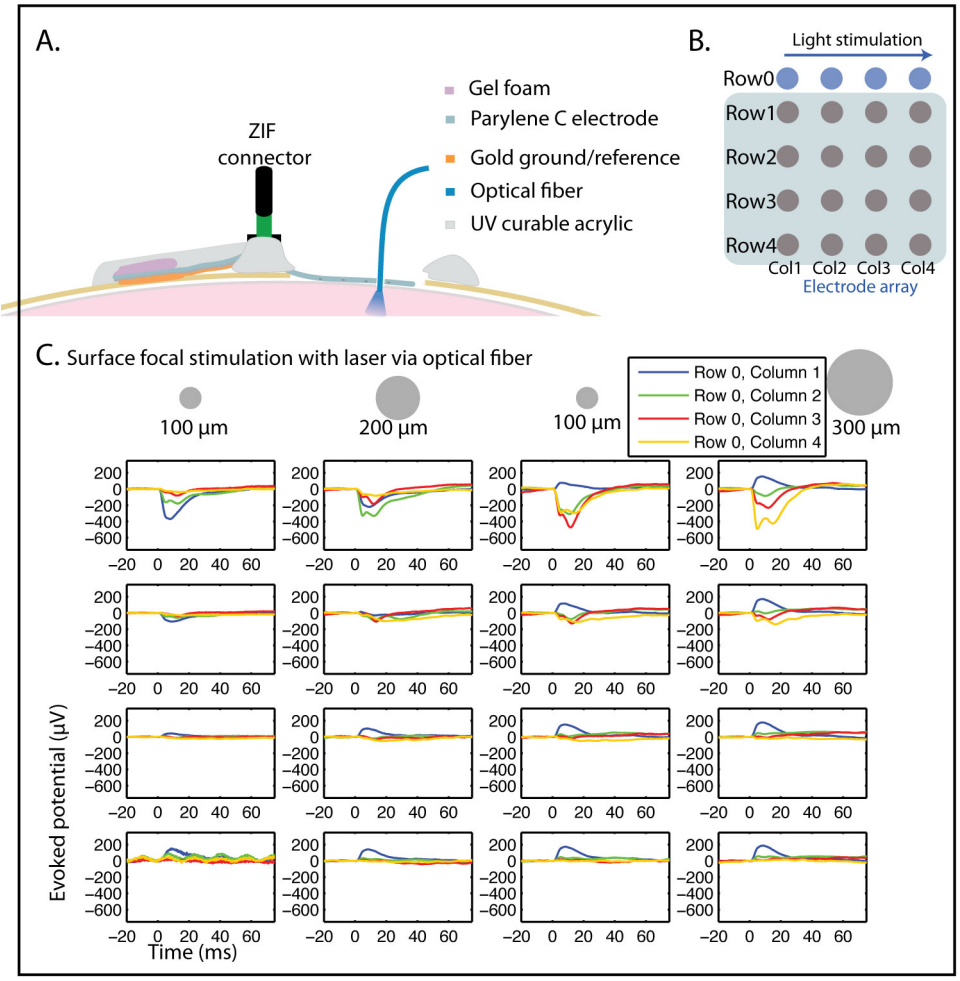

Figure 5.6: The focal stimulation at multiple locations on the brain surface. A. The cross section of terminal open cranial implantation surgery accommodating the optical fiber insertion. B. The electrode array layout and the surface photoactivation with optical fiber coupled laser. C. Evoked potentials in response to the photoactivation near each electrode site.

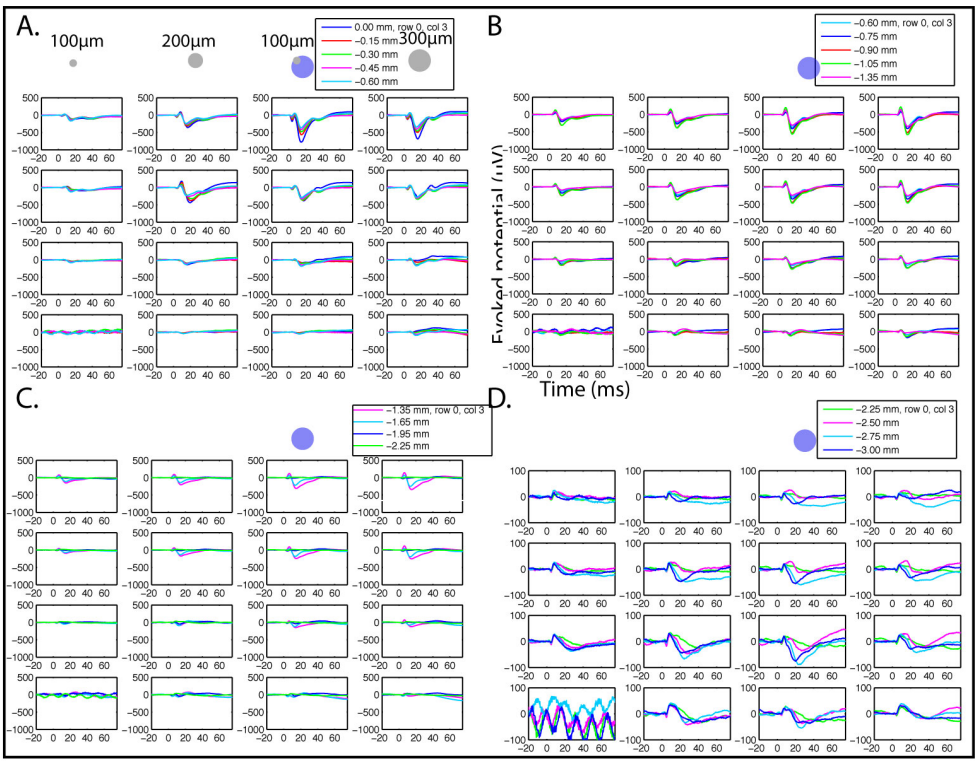

Figure 5.7: Focal stimulation at various depth with optical fiber coupled blue laser. A. At shallow cortical layer (0 to 0.6 mm deep) recorded local evoked potentials were large near the activated area (column 3) and found to be decreasing with depth. B. at 0.6 to 1.35 mm deep, C. at 1.35 to 2.25 mm deep and D. at 2.25 to 3 mm below the brain surface also follow the same trend as in A.

recorded potential amplitude after the focal depth stimulation.

Control experiments results

Three types of controls were performed, and all confirmed that the signals observed in Figures 5.4 and 5.5 were largely optogenetically mediated origin. Red LED light was used as a control stimulation as the Channelrhodopsin-2 is mainly activated by blue light (450-470 nm). The broad blue light stimulation with 50 and 100% of the LED light intensity, evoked large depolarization across the entire same electrode size array while red light stimulation did not activate the Channelrhodopsin-2, and thus no depolarization peak was observed (Figure 5.8A). We also implanted the micro-ECoG array in wildtype mice lacking ChR2 expression. No depolarization peak was recorded from the wildtype mice after due to blue light stimulations (Figure 5.8B). In addition, blocking the cortical window with black tape in mice expressing ChR2 abolished the observed depolarization (Figure 5.8C), a negative control confirming the necessity of light through the window to cause such a signal, and ruling out electromagnetic noise and visually related potentials. The photoelectric effect was less than 10 μV for a 10 ms pulse of light at full brightness. Compared to the depolarization observed in Figure 5.8A and C, the photoelectric effect (Figure 5.8C: right panel) was 2 orders of magnitude smaller. Moreover, the signal observed in vivo had a short onset delay followed by a briefly persisting depolarization (Figure 5.8C: left panel), while the photoelectric waveform did not show an onset delay or persisting depolarization. The post mortem control was also obtained 15 minutes after euthanasia. Blue optical fiber coupled laser stimulation at brain surface

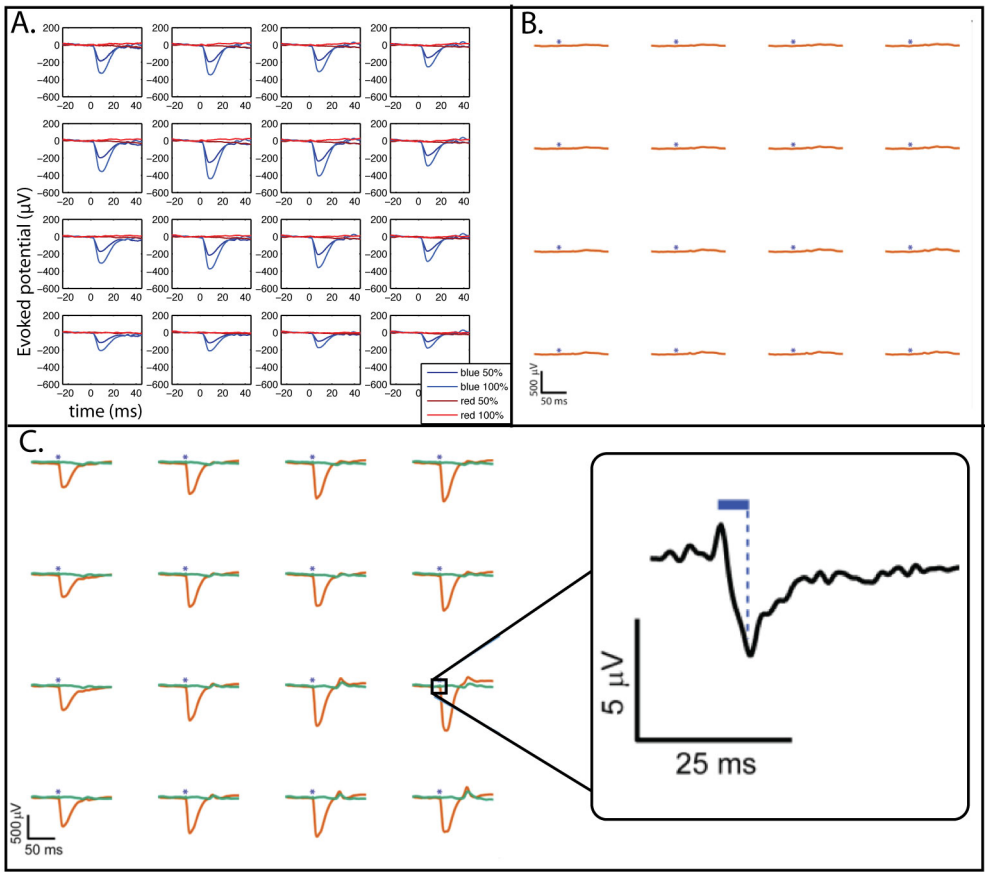

Figure 5.8: Control experiments performed to rule out photoelectric effect, electromagnetic effect and visual evoked potential. A. Broadly photostimulation with blue and red LED light at 50 and 100% light intensity shown that the channelrhodopsin 2 expressed neurons only activated by blue light. B. Wildtype mice implantation also show no depolarization in response of the blue LED light pulses. C. Photoelectric effect was tested utilizing the blue light pulse stimulation (shown in orange) and the window block result (in green) on the left panel. On the right panel, time-locked photoelectric response of less than 10 μV is shown (50 times smaller than the observed large negative peak).

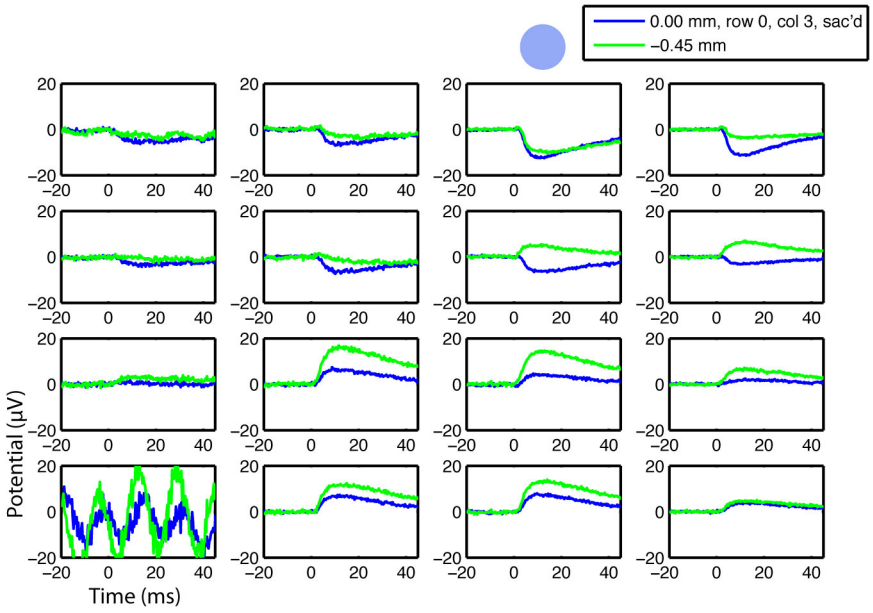

Figure 5.9: The potentials were recorded after the animal is dead for 15 minutes in respond to the focal stimulation with the optical fiber coupled laser at the location indicated by blue circle. These small potentials (less than 20 μV) are believed caused by the photoelectric effect but they are insignificant compared to the optogenetic response (more than 500 μV).

and 0.4 mm below the brain surface did not cause any depolarization post mortem as expected (Figure 5.9). These potentials were less than 20μV, and are presumably due to the photoelectric effect. However, they are incomparable to the previously recorded optogenetic response (more than 500 μV) before death. All of the controls clearly confirm that the potentials observed are mainly due to the collective depolarization of ChR2 expressing neurons due to photoactivation, not the photoelectric effect, electromagnetic effect or visual evoked potential.

5.5 Discussion and conclusions

A chronic optogenetic micro-ECoG neural interface utilizing the transparent electrode array and cranial window was demonstrated. Key features of this two-way neural interfacing are the minimal invasive nature of the micro-ECoG array and a non-invasive photostimulation. Together they provide a powerful tool for signal recording and stimulation that could be useful for many fundamental and application oriented developments. Rather than broadly activating the cortex through the cranial window, small volumes of cortical tissue could also be selectively activated with focused points of light. In this case, the spatial resolution of both micro-ECoG array and light source are important.

Optimizing the spatial resolution of the surface electrode array has been hindered by the difficulty of localizing the source of the neural activity of the recored potentials. Moreover, the accuracy of the neural activity origin can only be determined if the actual source location is known. The spatial resolution of the electrode array can be optimized by finding the suitable electrode site size and interelectrode spacing. By photostimulating known cortical locations, the correlation between the site size and recording capability can tested with our optogenetic micro-ECoG platform.

Our results have shown no relationship between electrode site size and the evoked potential amplitude in response to broad or focal photostimulation. However, different electrode sizes have different electrode impedances which corresponded to their surface area. The only noticeable difference between different electrode site recording capability was the high frequency noise floor.

Electrode sites with higher impedance tended to have greater high frequency noise. All the controls have ruled out the photelectric effect, electromagnetic effect and the visual response and confirmed that the depolarization was definitely a result of photoactivation of the nearby neurons. Based on these results we suggest that the interelectrode spacing may play more important role than the electrode size as the space between the electrode sites presumably influences the spatial sensitivity of the array. By adapting the experiment design, micro-ECoG arrays with various interelectrode spacing could be tested and optimized.

Further spatial investigations could be implemented with the current experimental setup, but further platform development could lead to more advance applications. One possible development is a fully integrated micro-ECoG array and the optical light source. The next chapter will include some of the proposed future directions for such device.

6 THIN-FILM MULTI-ELECTRODE ELECTRORETINOGRAPHY [1]

The tools developed for fabricating thin-film flexible micro-ECoG platforms has applications beyond the field of neural engineering. Using similar parylene C-based fabrication techniques, a thin-film electrode array was developed for novel ERG recording applications. Electroretinography measures electrical fields created by neurons in the retina and provides the clinician with useful information about the function of the retina. The ERG measures the activity of millions of retinal cells extending from the pigment epithelium to the innermost nuclear layer. By applying light stimulation to the eye, different ERG waveforms can be detected. The spatial and temporal distribution of the ERG waveforms are the basis for making a diagnostic decision.

As described in Chapter 1, ERG can be used for diagnosing defects in retina function, such as those occurring in eye diseases such as glaucoma [Moiceanu and Cârstocea (2010)], [Pangeni et al. (2012)], [Poloschek and Bach (2012)]. ERG can be used to detect and monitor many other retinopathies as well, such as retinal scar, Oguchi disease [Usui et al. (2004)], cone dystrophy [Kellner and Kellner (2009)] and hypoplasia of the optic nerve [Francois and Rouck (1976)]. In the past decades, several standard ERG electrodes have

[1] This chapter was adapted from the following manuscripts: "A novel multi-electrode Electroretinographic contact lens", Sanitta Thongpang, Ashley Selner, Tomas Ban, Thomas Richner, John Hetling and Justin C Williams, in preparation for Journal of Neural Engineering submission.

been used by clinicians, including the Henkes Lovac®, the Goldlens®, the ERG jet® and the Burian-Allen®. However, they have a single recording electrode that spatially averages the corneal potentials. Using the flexible thin-film technology developed, I demonstrate the ability to create electrode arrays mounted on a contact lens able to record tens of individual channels simultaneously, termed multi-electrode ERG, or meERG. The motivation for developing meERG arrays is to gain spatial information about the state of the retina by recording spatial differences in corneal potentials that are related to the spatial differences in retinal activity. Spatial differences in retinal activity often are associated with eye diseases that could be detected by early ERG screening and monitoring. However, spatial distribution of the corneal potential is currently under-studied, mainly because of a lack in platforms enabling its measure. The development of a device with the ability to measure the spatial distribution of the corneal potential may lead to advances in electrophysiological functional imaging through a non-invasive approach that allows high temporal resolution. In addition, the multi-electrode array could be used to assess the response of different cell types and test functional pathways by using appropriate stimuli and analyses.

The design goals and device requirements for the meERG involve the use of accessible fabrication techniques in order to produce these arrays in clinically relevant volumes as well as the use of materials and method that enable high channel yields and good light transmission to enable good visual acuity. We also aim to integrate the speculum for good stability on the eye while being comfortable and safe for the patients. The main difficulty resides in fabricating a multi-electrode array with a given curvature to match

that of a contact lens. We designed two different prototypes that avoid the patterning of the electrode array on 3D surface, thus enabling batch fabrication and the use of well characterized fabrication techniques, by first using the custom-made poly-methyl methacrylate (PMMA) lens with a flat top where the planar electrode array can be placed and a second which uses 3D matrix transformations that allow the fabrication of the device on a 2D surface first which then can be bend onto a contact lens of the appropriate curvature.

6.1 Planar CLEAr lens

The similarities in fabrication and signal analysis between the meERG and the micro-ECoG electrode arrays combined with the good optical properties of parylene C make the thin film neural electrode technology ideal for the development of MEMS-based contact lens electrode array (CLEAr) lens. Based on this, we designed a contact lens electrode array prototype adapted from the parylene C micro-ECoG fabrication techniques. In this chapter, I will present the fabrication methods developed for creating this meERG device as well as the results of a preliminary human-trial study made to test the good-functioning of the device. Finally, the development of advanced techniques to reduce the limitations of the original device will be presented.

Fabrication methods

This CLEAr lens consists in a long parylene electrode cable leading to a contact lens machined from PMMA. On the corneal side of the contact lens

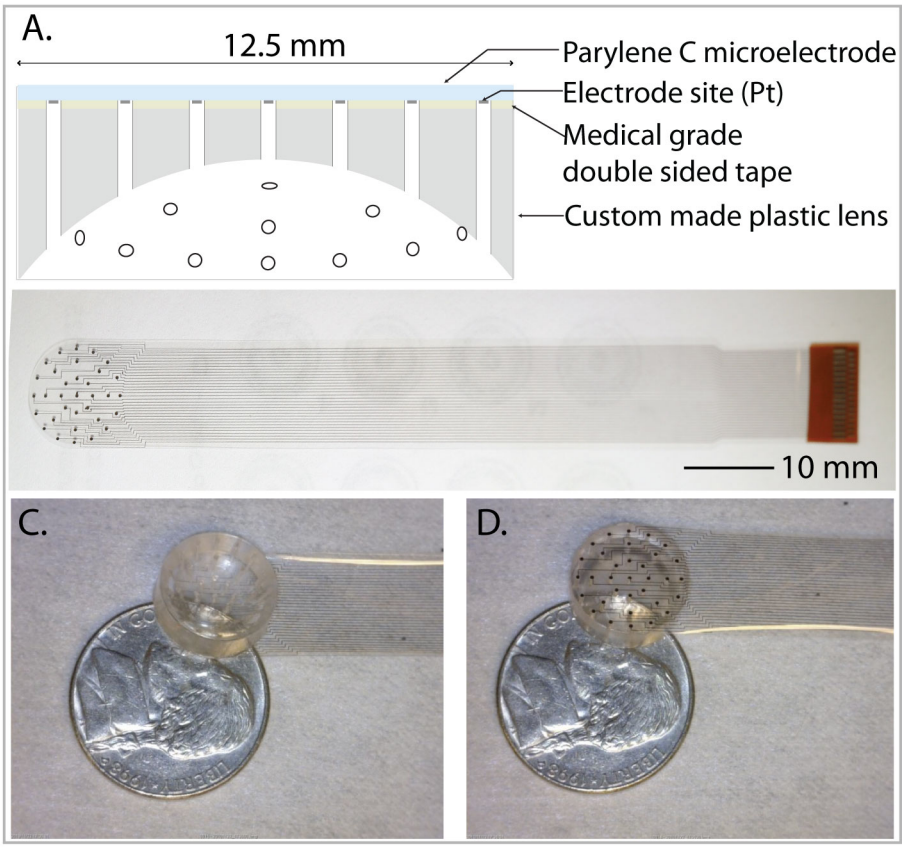

Figure 6.1: Human ERG electrode layout and assembly using a custom-made PMMA lens. A. Cross-section of the PMMA lens showing each assembly layer. B. Long multi-channel parylene C microelectrode array. C. Fully assembled human ERG with a polished corneal contact surface facing up. D. Identical CLEAr lens device with parylene C electrode array facing up. (C and D are provided by Prof. John Hetling, UIC, Chicago)

the PMMA surface was polished, and the opposite side is planar (Figure 6.1). The lens contains 33 holes with a diameter of 400 μm drilled perpendicular to the planar surface allowing each electrode site to be exposed to the eye surface. An electrode array containing 33 sites placed in a concentric ring pattern matching the holes in the PMMA structure was fabricated using similar methods as those used for parylene-based microECoG devices (Chapter 2, Figure 6.1B). The pre-cut medical grade double sided tape (3M®) was used as an adhesive layer to bond the contact lens and the electrode cable using a custom-made jig to align the hole and electrode site. The fully assembled ERG are as illustrated in Figures 6.1C and D.

Experimental setup

Human trials were performed to study the behavior of the CLEAr device. Prior to human involvement, each electrode array was initially thoroughly tested by measuring (1) the electrical impedance of each channel and (2) the electrical shunting between channels using electrode impedance spectroscopy (EIS). The latter was performed by applying a sine wave (100 mV peak-to-peak, 1- 300 Hz) to each electrode sites in saline bath. We verified that there was no cross-talk between channels observed and the average electrode impedance was 100-200 kOhms. Before using the ERG cable with the human subject, it was cleaned, disinfected and rinsed. Prior to recording the signal, an artificial tears solution is used to fill in the holes to conduct the electrical signal from the corneal to the electrode surface.

The CLEAr cable was connected to the data acquisition system via a commercially available 61-pin FPC connector (FH23-61S-0.3SHW(51), Hirose)

on the custom made printed circuit board which interfaces with a commercial 64-channel amplifier (Figure 6.2D). The subject pupil was dilated with eye drops (phenylephrine, 2.5%; tropicamide, 1%) and a topical anesthetic (proparacaine, 0.5%) applied to the cornea. Then the contact lens was placed on the cornea of the subject while seating with head in on the chin rest and facing a custom stimulus source dome as shown in Figure 6.2E. The reference electrode was placed on the cheek near the corresponding eye. After the eye of the subject adapted to the dark for 5-10 minutes, then full-field flash stimuli were introduced. The bandpass of the amplifier was set to include the range of at 1-300Hz, as recommended by the International Society for Clinical Electrophysiology of Vision (ISCEV) [Marmor et al. (2009)].

All 33 channels are recorded simultaneously with a sampling rate of 5 kHz. For each trial, 100 ms of pre-stimulus baseline and at least 900 ms of post-stimulus response were recorded. With the amplifier pass band at -3dB was 1 Hz - 5 kHz with a gain of 1200 and input impedance of approximately 10Î4 Ohms. The signal was recorded without filtering the 60 Hz noise, although it was removed later in post-processing. The position of the electrode sites were fixed and documented, for example as an orientation and mapping of the 33 channels shown in Figure 6.2A and B. With the 64-channel amplifier, a single Dark Adaptation (DA) response of all 33 channels can be recorded simultaneously as shown in Figure 6.2C.

Recorded electroretinogram signals

An important aspect of developing a functional electroretinograph electrode is the ability to measure different waveforms of ERG and determining

how these compare to standard ERG devices. We were thus interested in measuring these features for the novel CLEAr electrode developed. In particular, the meERG electrode should be able to measure the spatial and temporal distribution of the a-wave and b-wave following a light stimulation event. As mentioned previously in Chapter 1, dark adaptation (DA) refers to the recovery of the eye's sensitivity in the dark following exposure to bright lights. Similarly, light adaptation (LA) is the process by which a subject adapts to light when placing the subject in a dark room, and increasing the brightness of the light until the subject reports its presence. After the eye is adapted to the dark, the specific response of the retina can be measured by using a dim flash and bright flash. A brighter flash is used to measure the combined response of the rods and cones. For the CLEAr electrode array, the signal-to-noise ratio of the single DA (Dark Adaptation) response was calculated to be approximately 27 dB. However, variations in waveform shape, especially after the recording of the a-wave, indicates that some electrical paths between the cornea and the electrode were deficient, usually due to an inefficient distribution of the liquid from the tears and artificial tears, leading to inabilities to record spatial variations on corneal potentials. This can be avoided by making sure that that saline filling process was completed properly.

To confirm that the prototype can record ERG signal in different conditions, a bright flash DA stimulation, dim flash DA stimulation and Light Adaptation (LA) were performed. Some examples of bright flash DA response of two adjacent electrode sites (B1 and A16) are illustrated in Figures 6.2F and G. These show both an a-waveform with a magnitude of ~400 μV

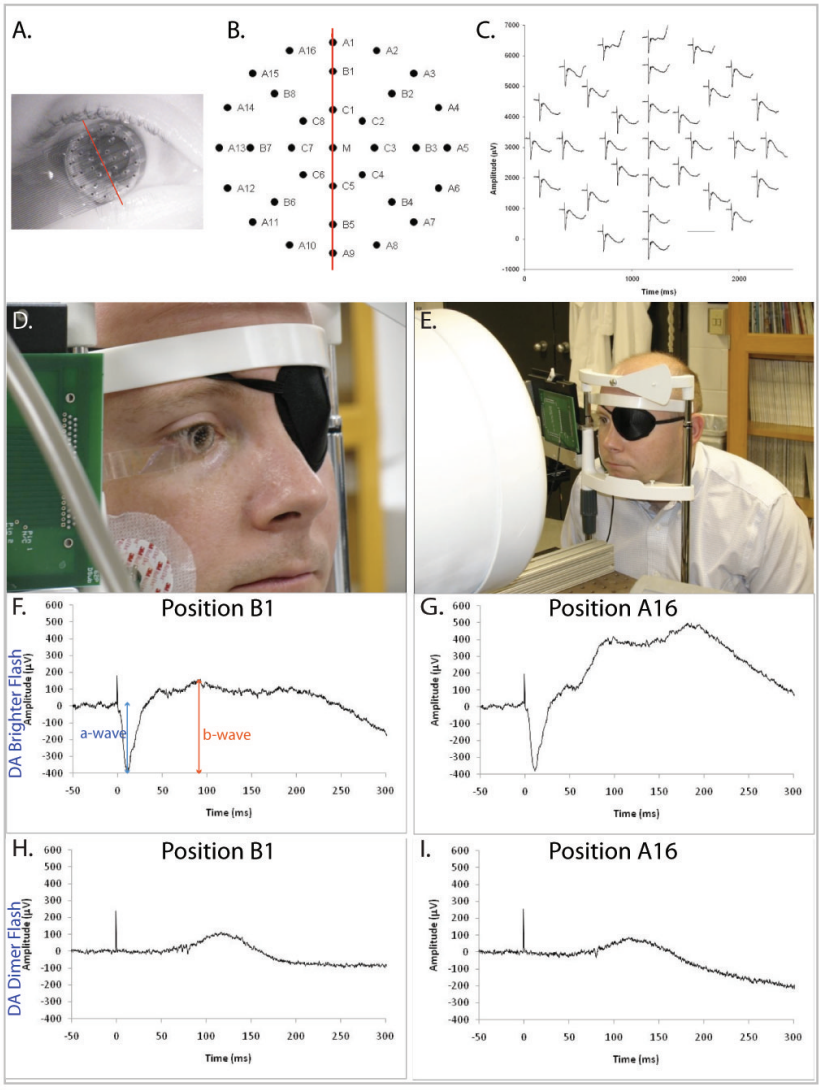

Figure 6.2: Human meERG electrode using a custom-made PMMA lens and example of the recorded signals. A. CLEAr lens position and orientation on the subject's eye. B. Electrode mapping of 32 channel meERG. C. A single Dark Adapted (DA) response illustrating a reasonable signal-to-noise ratio of ~27 dB in all 32 channels. D,E. Custom CLEAr lens on a human volunteer placed in the context of clinical diagnosis. F,G. DA bright flash response of two adjacent channels (B1 and A16) out of the 32 working electrodes displaying a- and b-wave response. H,I. DA dimmer flash response of the B1 and A16 electrodes which can be used to monitor b-wave originated in the ON bipolar cell. (These images are provided by Prof. John Hetling, UIC, Chicago)

(time to peak ~10 ms) and b-waveform with an amplitude of 550 μV (time to peak ~100 ms) in electrode B, as well as a slightly larger b-wave amplitude in A16 (~900μV) after a flash stimulus at time ~180 ms. A dimmer flash DA response as shown in Figure 6.2H and Figure 6.2I can be used to elicit a b-wave response. All of the example stimulated results suggest that this first CLEAr lens prototype has suitable recording characteristics compared to conventional ERG electrodes. However, several main limitations with this prototype were observed. First, the process required that the electrode holes were filled properly, which is why a vacuum-aided filling was chosen. Second, the shape of the meERG inherently means that it prevents proper formation of an image on the retina. To tackle these limitations, an improved meERG devices will be described next.

6.2 Image-forming ERG electrode arrays

Although preliminary data suggests that the first version of electrode array performs to an acceptable level, one factor that could improve the image formation of the CLEAr lens is to combine the rigid clear contact lens with the transparent ERG cable. Since the machined PMMA lens is up to a few millimeters thick around the edge, the subject cannot forms clear image through this lens. We propose an alternative design in which the thin-film parylene electrode is bonded on the concave side of the rigid clear contact lens such that the electrodes and the cornea are in close contact and the thin contact lens allows maximum light passing through. Contact lens fit specific patient eye sight conditions can be used and incorporated with the parylene

C ERG array. This new design enables higher light stimulating pattern complexity for greater spatial information achieved by the ERG electrode arrays. We hypothesize that this approach will increase the spatial resolution and hence improve the ERG signal quality. To achieve this goal, a 3D matrix transformation algorithm was adapted to create a planar multi-electrode array that conforms to the surface of the commercial contact lens.

Electrode design and Matlab transformation

Having a contact lens with electronic components embedded is a desirable feature, but achieving such objective is not simple because of the curvature of the desired electrode arrays. Moreover, it is time consuming and complicated to fabricate such devices as reported in different applications using maskless laser-write lithography [Yoo et al. (2009)], and vacuum-supported stretchable PDMS material to form 3D surface [Jung et al. (2011)]. An alternative design, proposed to overcome the discussed problems, can be developed by using 2D fabrication methods, similar to those used for thin film neural interfaces, and made into a 3D surface subsequently. The approach we propose uses a bucky-ball pattern in 2D to fill the surface of a 3D sphere [Hinds et al. (1991)]. After the fabrication is completed, the sphere can be formed using combination of hexagon and pentagon shape faces.

Figure 6.3 A shows how the bucky-ball hemisphere and points on hexagon and pentagon planes can be interpolated and projected onto the 2 dimensional surface. The algorithm used starts by creating the bucky ball vertices using built-in functions of Matlab and then unfolds the coordinates and connecting points to form hexagons and pentagons on a plane. Subsequently,

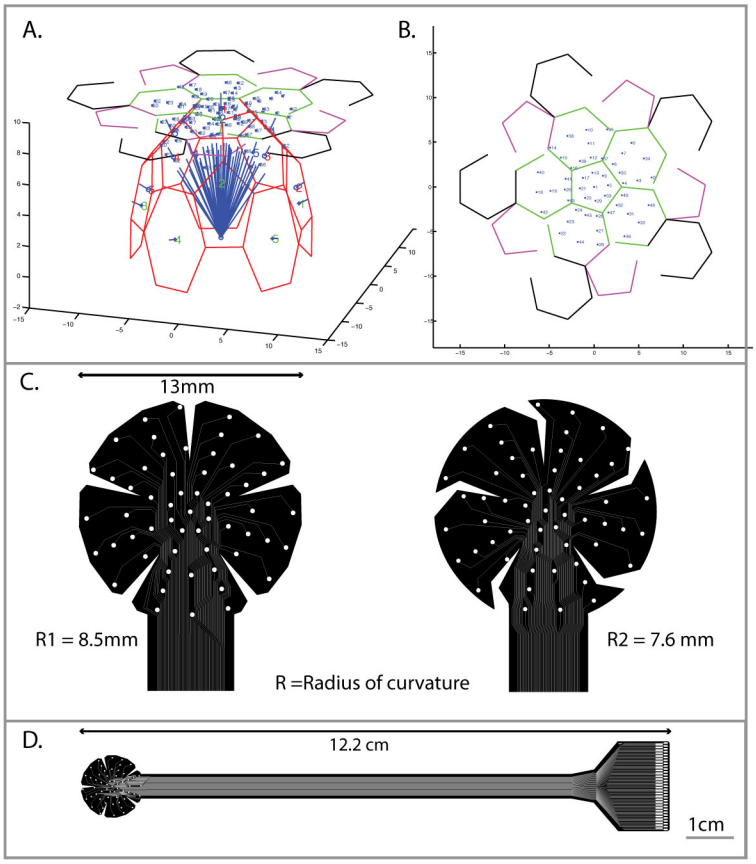

Figure 6.3: Image-forming lens design principle using matlab algorithms to map the curved 3D bucky-ball surface onto a planar surface. A. 3D view of the Bucky-ball shape and the projection of the electrode sites onto a planar surface using a matlab algorithm. B. Bucky-ball shape with the electrode sites projected onto a 2D plane. C. Design in Illustrator of the mask utilized for the patterning of the electrode sites in 2D based on the results of the matlab algorithm. Electrode array layout contains 57 electrode sites distributed concentrically on the lens area for different size of contact lens . D. General layout of image-forming contact lens with long cable of 12 cm.

the electrode sites are assigned by generating the lines from a hemi-sphere's origin and intersecting with each plane. Once the electrode sites are assigned on the hexagon or pentagon plane, the plane and points are translated and flattened. All the planes can then be projected to the top in Z axis. Since the human cornea may have different diameters and radii of curvature, the electrodes can be designed to fit perfectly each specific contact lens by simple Matlab parameters alteration (radius of curvature and angle of the outer most electrode row). This results in slightly different electrode layout for each contact lens as shown in Figure 6.3C. Final editing of the electrode pattern and scaling is performed in Adobe Illustrator (Figure 6.3D. Using simple photolithography described in Chapter 2, the thin-film parylene electrode arrays can be fabricated in large batches, thus facilitating the fabrication process.

Electrode assembly

The electrode and contact lens bonding is illustrated in Figure 6.4. 2D parylene C electrode arrays were bonded with the rigid PMMA contact lens (TruForm Optics Inc.) by sandwiching them between the PDMS molds. PDMS molds were specifically made from each contact lens size. The first step in the fabrication of the mold of the contact lens (Figure 6.4A) is the placing of the contact lens in a small pool of un-cured PDMS, applying a gentle pressure on it, and backing at 85 degree celsius for 1 hour. Next a monolayer of silane is deposited on the backed mold to facilitate further demolding steps (Figure 6.4B). A negative mold is then made by casting a second PDMS mold from the positive PDMS mold (Figure 6.4C). Silane

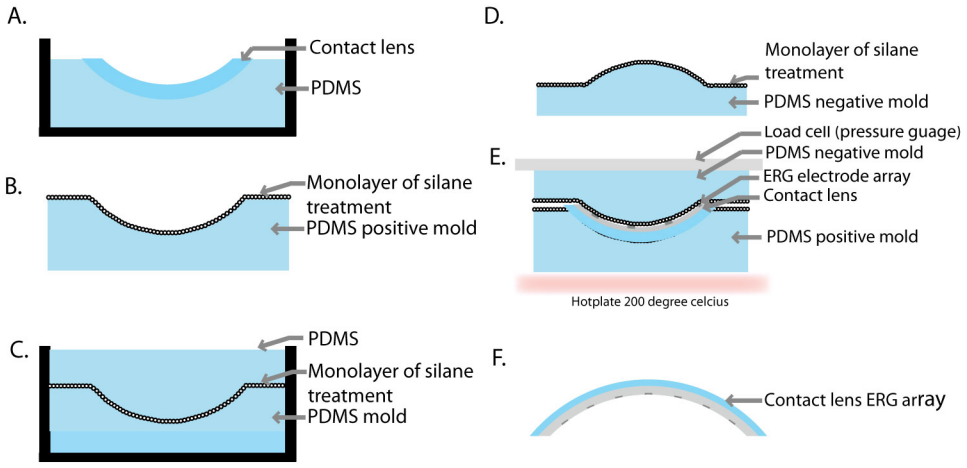

Figure 6.4: Overview of the fabrication steps for fabricating the curved meERG electrode array. A. A rigid contact lens is weighted down with a small piece of PDMS in a un-cured PDMS bath. B. The rigid lens is removed after curing and a monolayer of silane is deposited. C. Another layer of PDMS is poured in the mold and cured in an oven. D. The negative mold is removed and a monolayer of silane is deposited. E. The electrode array and contact lens are sandwiched between the positive and negative PDMS molds and bonded at a temperature of 200 degree celsius for 4 hours. F. Fully assembled curved meERG contact lens.

was deposited on the second mold as well (Figure 6.4D), after which the rigid clear contact lens and parylene C electrode array was aligned and sandwiched between the two PDMS molds under high pressure (300 kPa) at 200 degree celsius for 4 hours. This process firmly bonds the 25 micron-thick electrode array with the rigid contact lens without requiring any adhesive layer (Figure 6.5A). The bonding was tested successfully in a saline soaking test for 24 hours (Figure 6.5C). Since the electrode array with electrode site sizes of 250 micron in diameter (Figure 6.5B) as well as the contact lenses are

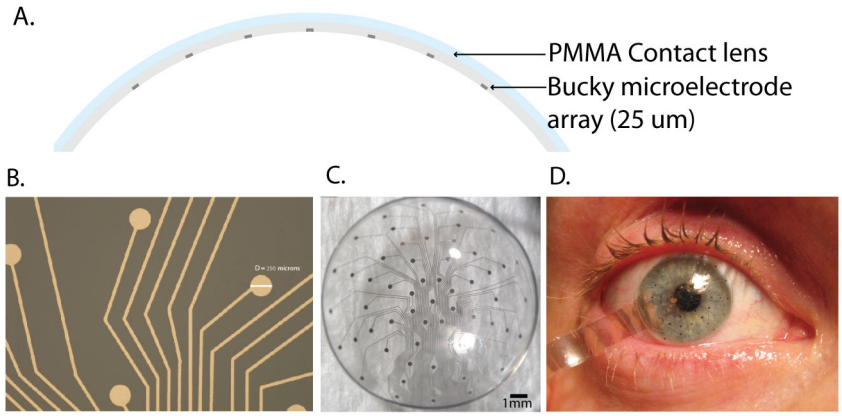

Figure 6.5: Human meERG. A. Cross section of the improved curved meERG electrode in which the thin-film electrode is bonded to a PMMA contact lens with applied heat and pressure. B. Microscopy image of the electrode array showing the electrode traces and electrode sites which have a diameter of 250 μm. C. Close up of a meERG electrode array bonded onto a rigid clear contact lens to form a 3D curved electrode array for ERG recording. D. Image of the meERG device on a human eye. The lightweight and flexibility of the electrode allows a much more convenient and comfortable diagnostic experience for the patient.

transparent, the finished image-forming ERG lenses has high visual acuity allowing good light transmission even with the parylene C electrode array which is desirable for ERG electrode (Figure 6.5C). In addition, this improved ERG contact lens also retains a close proximity to the cornea surface allowing a high visual acuity and image formation as can be seen in Figure 6.5D on a test subject's eye.

Despite success in the initial fabrication trials, the development of a useful ERG lens will require further characterization of the image forming ability and clarity of the electrode array, which is the topic of the next section.

However, in order to develop a fully re-usable device, further developments and optimizations would be necessary. Plans and ideas to enhance the ERG performance and durability are expanded in chapter 7.

Recorded ERG signals from rigid clear ERG lens and visual acuity testing

The response of the image-forming ERG electrode array for a panel of different tests was measured here. After impedance testing, the ERG signals of one human subject were recorded in response to the full field light stimulations. Examples of recorded signal from the first trial with this improved image-forming lens show multiple dead sites due to either a broken connection in traces leading to electrode sites or bad contact pads to FPC connections (Figure 6.6A). The ERG signals recorded from the working electrode sites show comparable signal quality to the CLEAr lens with a low noise level. Improved bonding and connecting issues will help increase the number of working electrodes in the future.

The improved image-forming lens appears to be clearer and allows more light to pass through than for the CLEAr lens. For ERG recording the subjects are seated in front of the full-field light stimulating setup and hence the severe compromised visual acuity occurring with CLEAr lens is not crucial. As long as the light was able to go through the lens, the recorded ERG signal should be sufficiently accurate. However, the ability to stimulate the retina with a spatially controllable signal, and subsequently record the response of the retina may help diagnose retina related diseases using

A. ERG signals

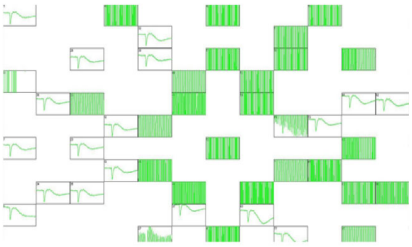

B.

Test		Lens without electrode	Lens with electrode
Humphrey	Mean Dev.	-3.24 dB	-5.24 dB
	Pattern Dev.	1.48 dB	1.19 dB
Goldmann (total visual field)		No significant difference	
Visual acuity	No correction	20/25	20/160
	Correction	20/12.5	20/32
Contrast sensitivity	No correction	1.95	1.95
	Correction	1.95	1.50

Figure 6.6: ERG signal recording and visual test results of the improved curved meERG device. A. Examples of ERG recordings of a clear ERG contact lens electrode. The sites with large large green traces display (dead channels) probable fabrication and assembly defects. B. A table summarized the visual test results of the clear contact electrode.

image-forming ERG lens. The visual acuity of the new image-forming lens was was characterized to prepare for these enabling experiments. Multiple visual tests including the Humphrey 24-2 SITA Standard test, the total visual field measure, the Lighthouse (Bailey-Lovie) chart and the Pelli-Robson contrast sensitivity test were performed with the image-forming lens with and without the correction lens for the patient's eye sight and these were compared to the values found in the absence of the electrode array.

A summary in Figure 6.6B shows that the lens without the electrode array is not significantly different from normal for all of the tests, but the lens with the electrode shows the Humphrey mean deviation approximately 2 magnitudes different from the normal value. Furthermore, the visual acuity test result of the lens with the electrode array without additional correction is significantly different from normal (20/160) whereas the normal acuity is 20/20. However, after adding a correction lens, the visual acuity has

improved to 20/32. The Pelli-Robson contrast sensitivity test results suggest that the image-forming lens slightly compromises the contrast sensitivity in general, although it is comparable to the lens without the electrode array. We found a value of 2.0 on this test, suggesting that the image-forming lens performs right at the limit at which sensitivity is determined to be impaired. For reference, the worse cases are visual impairment and visual disability are found for values of less than 1.5 and 1.0, respectively. However, the contrast sensitivity with the correcting lens shows greater impaired sensitivity (1.5). In addition, Goldmann perimetry test for total visual field of the lens with and without the electrode array have no significant difference between the two conditions. In summary, the image-forming lens slightly impairs the vision compared to the lens without the electrode. One has to keep in mind, however, that CLEAr lens does not allow proper visual function. Thus the developed image-forming lens that allows seeing and reading remains a significant improvement that could be brought to the device. Future development can also be performed to improve the visual acuity by using transparent conductive polymers for electrodes and trances, and the parylene C electrode cable thickness can be adjusted to avoid the use of correction lens.

6.3 Conclusions

The novel CLEAr and image-forming array displays good signal recording ability and acceptable stability. Moreover, the devices developed provide higher spatial resolution than all of the current ERG approaches. The density

of electrodes is also highly improved as the traditional ERG electrode has only one electrode channel, while the improved prototypes developed here contain up to 57 channels. This feature enables a high spatial information when recording corneal potentials. Finally, the image-forming lens developed hints at the possibility of creating micro electrode arrays that has high visual acuity, which would enable novel applications in which not only high spatial light stimulation can be inputed to the patient, but also spatial information of the retina. I expect that these devices will yield novel diagnostics abilities for retina dysfunction diseases.

7 CONCLUSIONS AND FUTURE DIRECTIONS

The work presented in this document describes devices and techniques for improving Brain-Computer Interface (BCI) and Electroretinography (ERG) using thin-film flexible electronics technology. In chapter 1, I presented an overview on neural interface development including neural systems, devices interfacing with the Central Nervous System (CNS) for BCI applications and retinal interface devices for ERG application.

In chapter 2, I detailed the general methods for materials selection, flexible thin-film device fabrication methods, device assembly, connection schemes and head chamber design for BCI. The development and methodologies presented in this chapter focuses on two major biocompatible materials for long-term neural interface device fabrication: polyimide and parylene C. These two thin-film materials are popular for the development of flexible electronics, and each have comparable advantages and disadvantages. Both materials can be fabricated and assembled conveniently using method developed and described in the chapter (i.e. methods based on Flexible Printed Circuit connector and Zero Insertation Force (ZIF)-Printed Circuit Board (PCB) adaptor). However, Parylene C presents an added advantage of being transparent and being the only Food And Drugs Administration (FDA) approved material for human implant. Thus, it is likely to be chosen for optogenetics and imaging applications.

In chapter 3, I presented a comparative study of polyimide and parylene C as materials for flexible thin-film micro-Electrocorticography (micro-ECoG) electrode. The two materials were compared for not only their electrical performance and durability pre- and post-implantation, but also for their long-term biological response. Rats were implanted with polyimide micro-ECoG arrays on one side of the brain and parylene C arrays on the other. This direct *in-vivo* comparison shows that both materials are comparable in terms of mechanical properties, suitable electrical properties and the minimal induced biological response. In summary, both materials are good candidates for developing micro-ECoG devices, although polyimide is more favorable for applications that require high temperature resistance and parylene C is more suitable for optogenetic, ERG and imaging applications.

In chapter 4, I investigated the long-term stability of the micro-ECoG array for BCI application in non-human primates. I present the electrode array and head chamber designs developed for improving long-term implantation ability as well as the signal performance and stability. Emphasis was put on developing methods for simple device fabrication and minimally invasive surgical techniques. Further, the signal recording quality and stability show promising results as they can record evoked potentials and baseline activity with minimal noise for at least 6 months after implantation. I demonstrate that the developed platforms are able to record the high frequency gamma band (70 Hz) with an optimized spatial distribution. This ability is important for BCI application as it is thought that the high gamma band contains useful and important information. Finally, I present results on the biological response at a cellular scale of chronic implantation of these devices, and

show that the micro-ECoG platforms we developed have the potential of being opted for BCI in clinical setting.

In chapter 5, I presented work aimed at theoretically optimizing electrode array design for optimal brain signal recording. An important technology adopted and developed in this chapter is optogenetic, which allows to activate neurons with the use of light in a very controlled spatio-temporal manner. Spatial resolution of the electrode array is an important factor for developing optimal BCI devices. By combining optogenetic animal models and cranial window imaging, I presented results of the baseline neural activity and the evoked potential in response to the light stimulation either on the brain surface or under the cortex. The correlation between the electrode site size and the signal amplitude is insignificant as the electrode array with different site size can record comparable evoked potential amplitudes. However, the small electrode site size has high electrode impedance induced high frequency noise. For the best recorded signal-to-noise ratio, the bigger electrode site sizes are preferable although they limit the spatial resolution. While further investigation is required, the models developed here are good starting points for answering these questions.

In chapter 6, I emphasized other application that was made possible by the versatility of the fabrication methods developed. Using the similar processes, the flexible thin-film electrode arrays were designed for recording the neuron signals originated from the retina. Such electrode is called electroretinography (ERG) electrode array. Our novel electrode arrays utilize the flexibility, transparency and durability of parylene C to make multi channel ERG electrodes for retina mapping and retina function monitoring

that have pre-determined curvatures to adapt to the organ they target, in this case, the eye. I show that these types of devices are simple to fabricate, have potential medical diagnostics applications, and show promising results on preliminary human trials.

To address some issues and potential improvements of neural interface devices presented in this dissertation, the next section will discuss the future directions of the devices for BCI and ERG applications.

7.1 Future directions for micro-Electrocorticographic electrode array

Several improvements on current methods for micro-ECoG show promise, including the development of organic conducting materials for simpler fabrication methods and the integration of light sources to the micro-ECoG platform with light-guides and/or Light Emitting Diode (LED). Optogenetics has enabled the efficient and minimal invasive two-way neural interface for more advanced BCI as discussed in Chapter 5. Fully transparent and light source integrated device that allows maximum light transmission to the cortical cortex in awake animal is desirable. This section presents some of the possible device improvements that are well suited for optogenetic applications.

All-polymer micro-ECoG electrode

The current micro-ECoG fabrication relies on high cost materials and processes, involving complex equipment for the fabrication steps (i.e. Reactive

Ion Etcher and metal evaporation). In order to make it more accessible, an interesting approach, the solution based or roll-to-roll production is favorable. Moreover, to take advantage of optogenetics, the completely transparent device would be attractive as it passes most of the stimulating light to the underlying target cell specific regions. This section will propose some of the considerations for new electrode designs including materials consideration and possible fabrication methods.

Materials consideration

The current micro-ECoG array are made of parylene C and polyimide as insulating materials and gold/platinum is used for the electrodes and traces material. These two polymers are proven to be well suited for long-term neural implant device as discussed in both Chapter 3 and 4. However, emerging neuroscience tools such as optogenetics and cranial window implantation require a maximum light transmitted device. For this reason, parylene C would be an obvious choice for the insulating layers. One limitation of using parylene C is its patterning process, as it requires complex and expensive laboratory equipment. Alternatively, polymers such as Poly(p-vinyl phenol) or PVP [de Gans et al. (2006)] can be patterned using low-cost ink-jet printing methods, which have the ability to make the whole micro-ECoG field accessible to a larger audience of researchers, and be the basis for rapid-prototyping micro-ECoG techniques. Another interesting insulating polymer is sprayable colorless polyimide from Kolon Industries. This newly developed polyimide is colorless (88% light transmission at 550 nm) as well as being a great moisture barrier with good dielectric properties and easily

processed by organic solvents, with roll-to-roll processing capability.

The current conductive layer for electrode and interconnecting traces is based on metals such as Au and Pt. Gold and platinum have low electrode impedance, good conductivity and are bio innert, therefore they were chosen as conductive materials. However, they are not transparent and hence not the best option for optogenetic related applications. ITO is a transparent metal oxide that has been applied for example in organic LEDs [Kim et al. (1999)] and Flexible sensors [Mitsubayashi et al. (2003)]. However, the high cost and brittleness of ITO are strong limitations for flexible electronic applications. Alternative flexible conductive polymers exist, such as Poly(3,4-ethylenedioxythiophene) poly(styrenesulfonate) or PEDOT:PSS. This polymer has additional interesting features such as providing good conductivity, a fully solution-based material [Touwslager et al. (2002)], inkjet printability [Srichan et al. (2009)], [López et al. (2008)] and low cost. Yet another conductive polymer used in all-polymer integrated circuit [Drury et al. (1998)] is doped polyaniline (PANI). The important considerations for choosing the conductive polymers are the conductivity, solubility and biocompatibility. PEDOT:PSS has already been applied in neural penetrating probes for lowering the electrode impedance [Yang et al. (2005)], [Ouyang et al. (2011)], [Ludwig et al. (2011)], suggesting that it will be a good biocompatible candidate in micro-ECoG applications.

Possible fabrication methods

The all-poymer approach can be fabricated using polymers mentioned in the previous section. One strategy is to take advantage of our existing

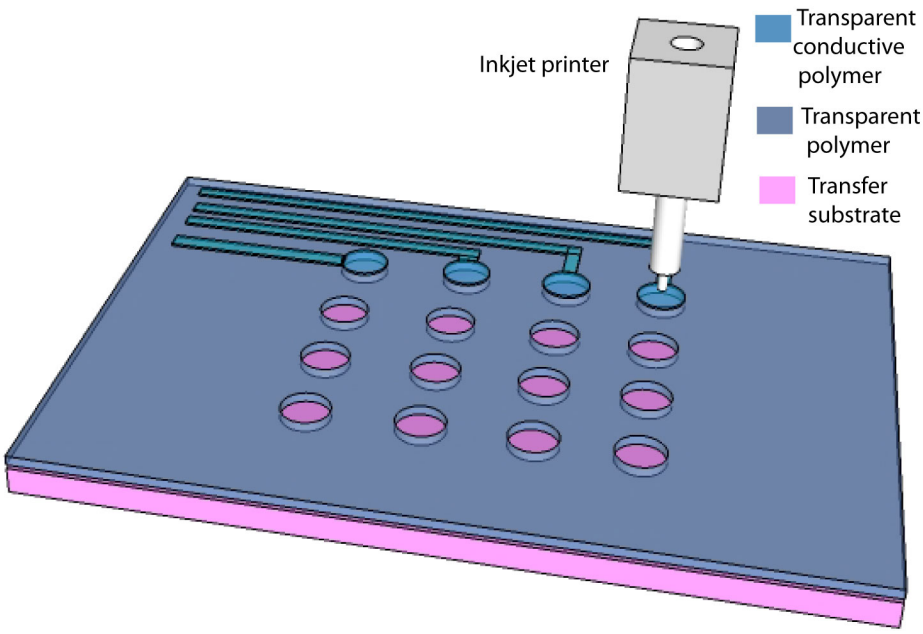

Figure 7.1: All-polymer micro-ECoG based on inkjet printing process

parylene C material that is well characterized. The first layer of all-polymer micro-ECoG will use patterned parylene C layer as a bottom insulating layer. Then conductive polymer such as PEDOT:PSS can be printed on top of the underlying parylene C layer using inkjet printer or Dimatix bioprinter as illustrated in Figure 7.1. If the first layer is parylene C, photolithography and oxygen plasma etching are required for patterning. On the other hand, the new colorless polyimide (CP) that can be patterned by organic solvents could be an interesting alternative candidate for the material base. In this case, the first layer of CP will be sprayed on a carrier substrate and then cured. Once the first layer is done, PEDOT:PSS can be printed to create the

electrode sites, pads and connecting traces. The last insulating layer could be achieved similar to the first layer. The alternative insulating material is spin-coatable or printable PVP polymer which can be etched or patterned by using solvent to dissolve unwanted area [de Gans et al. (2006)]. PVP will allow an increase in the density of interconnecting traces since multiple layers on the device can be achieved by printing multiple insulating PVP layers.

Integrated Optogenetic micro-ECoG electrode

Increasing interest toward optogenetics suggests that there is strong potential for the development of a micro-ECoG platform containing a fully integrated high density light source for two-way neural interfacing in awake animal. In this section, I propose two different approaches to fabricate such device. The first approach is to adopt the commercially available discrete LEDs from Rohm Semiconductor (SMLP12 Series, Pico LEDs) that provide high light intensity with small forward voltage (2.9V, for blue LED). Furthermore, this LED series also provides yellow LED that can inhibit the neurons action potential in Halorhodopsin mice. Combining blue and yellow LEDs in the same micro-ECoG array will enable activation and inactivation of the genetically modified neurons that have both Channelrhodopsin-2 and Halorhodopsin channels.

Second approach is developing fully organic flexible micro-ECoG arrays with integrated LEDs. This strategy involves the polymer LED (pLED) that have been extensively researched in printable electronic applications and photovoltaic communities [Reboud et al. (2012)], [Yao et al. (2012)], [Jin et al.

(2012)]. The existing pLED fabrication methods can be modified to suit the requirements of implanted BCI applications including long-term stability and biocompatibility.

Discrete LEDs approach

An achievable fabrication process for discrete LED integration with the micro-ECoG we developed is illustrated in Figure 7.2A. Since LEDs require forward voltage supply and ground, the LEDs embedded in parylene C insulating layers will be connected to the passive side of the PCB/headstage. The other side of the PCB/headstage is active in which micro-ECoG array will be connected to the headstage amplifier required for brain activity recording. The recommended discrete LEDs (Rohm Semiconductor) made from semiconductor materials is enclosed with a small package. Their compact size (0.2 mm thick) and 0.6 x 0.4 mm dimensions make the integration with the polymer feasible [Hu et al. (2011)] (Figure 7.2B). The power supply and ground pads can be bonded directly using antisotropic conductive film (ACF). The cross section view of the discrete LED integrated micro-ECoG array visualizes how this device will be fabricated and assembled (Figure 7.2C) where the LED array will be aligned and bonded on top of the micro-ECoG array. Alignment is a possible source of concern for the success of this approach. However, the challenge in alignment is surmountable and this approach could lead the first integrated LED-micro-ECoG array.

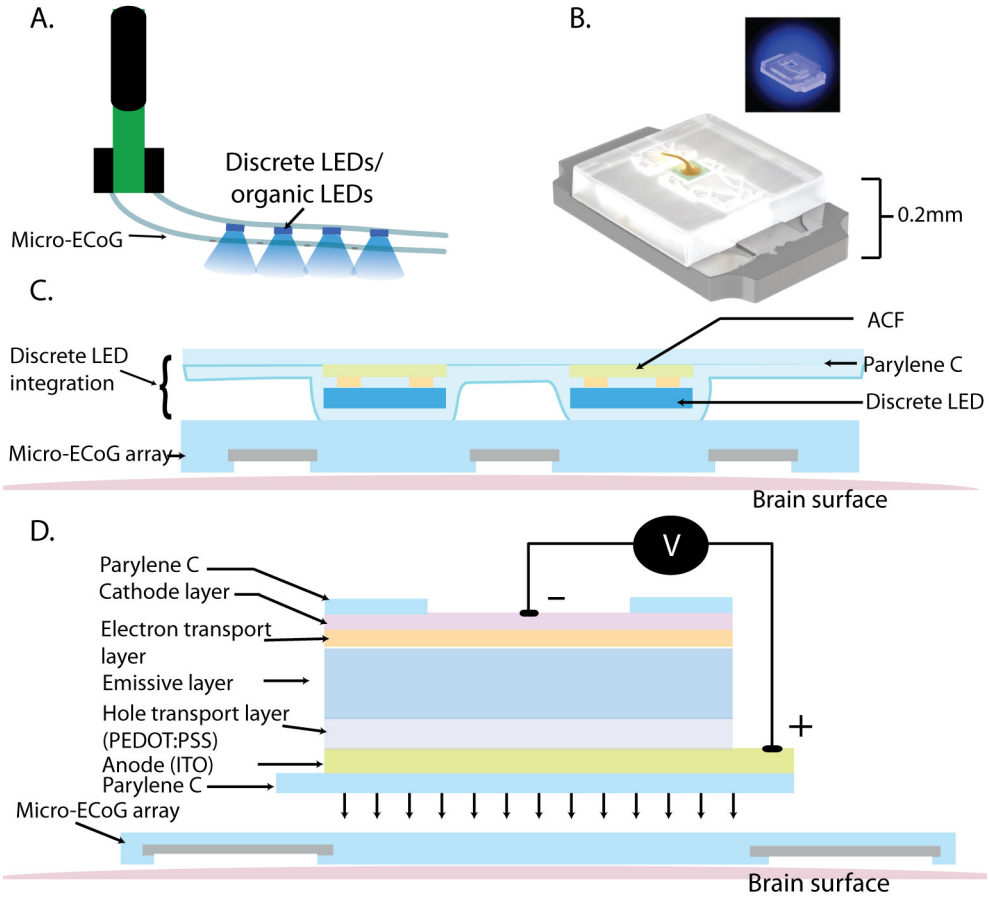

Figure 7.2: Integrated micro-ECoG electrode for optogenetic applications. A. Illustration of the micro-ECoG electrode with integrated LEDs. B. Example of discrete LEDs from Rohm Semiconductor. C. A cross section of the proposed micro-ECoG with discrete integrated LEDs. D. A pLED integrated micro-ECoG electrode.

Polymer LED approach

The simplest polymer Light Emitting Diode (pLED) consists of an organic semiconductor layer sandwiched between the two metal electrodes. pLEDs have attracted interest because all device layers can be processed in solution, which enable roll-to-roll processing capabilities for many flexible electronic applications. Moreover, the interface between different layers do not have to be structurally regular at atomic level. Using this technology it is envisageable to integrate pLED on a micro-ECoG array as shown in Figure 7.2D.

In this approach, the pLED anodes will be fabricated using an ITO layer (Approx. 100 nm) covered with a PEDOT:PSS hole-injection layer (high energy level). The light emitting layer can be selected for the desired neuron activating wavelength. Blue and yellow are commonly used wavelengths for channelrhodopsin-2 and halorhodopsin channel activations. A possible blue light pLED prototype can be based on commercially available products such as Poly(p-xylene tetrahydrothiophenium chloride) [Ding et al. (2003)] from Sigma Aldrich. A yellow light pLED can be fabricated using Poly(p-phenylene vinylene) (PPV). More polymers will become available for these pLED applications as improved materials and variation constantly emerge. Importantly, the light emitting polymer layer has to be carefully selected for the most efficient device as the micro-ECoG requires low forward voltage supply and high emitting light intensity. A very suitable material for the electron transport layer (ETL) is poly [(9,9-bis(3'-(N-N-dimethylamino)propyl)-2,7-fluorene)-*alt*-2,7-(9,9-dioctylfluorene)] (PFN) as it is compatible with a solution based fabrication scheme. In order to complete

the pLED a cathod material must be selected. It appears challenging to find a solution-based cathode metal that would be acceptable for an implantable device. A temporary alternative is to finish the pLED by a deposition of an aluminum or ITO layer.

A valid concern regarding a solution-based approach is the biocompatibility of the final device. An alternative approach is to place the integrated LED device on top of a cranial window while the micro-ECoG array can be seated on the brain surface under the glass window. This way, we can minimize the possible detrimental chemical interactions with the pLED materials and the brain.

7.2 Future directions for electroretinographic electrode

Transparent thin-film technology has also proven to be one of the practical choices for ERG electrode array because of its excellent light transmission and flexibility. Our prototypes presented in this dissertation have shown their potentials for retina mapping and retina function diagnosis because of the novel multi electrode array consisted of concentric rings of up to 57 electrodes. The basic ERG signals were recorded and proven to be comparable to the standard ERG electrode. However, there are some issues remaining with the ERG electrode designs described in this thesis, which could be improved in the future.

Existing ERG design improvement

The custom PMMA plano-concave ERG lens requires a conductive solution (artificial tears) filling in the holes at every electrode site prior to each recording session. The current method of filling the artificial tears requires a vacuum. If this process is not done carefully, the electrode surface could be damaged, resulting in a noisy signal due to high electrode impedance. In the worst case, the electrode surface may lose electrical connection and eventually loose the recording ability altogether. To avoid this issue, the custom PMMA lens can be filled with the hydrogel loaded with a conductive solution.

Currently, our collaborator (Dr. Hetling's lab) has managed to reuse the prototype design by peeling of the electrode array and strip off the medical grade adhesive layer. The new electrode array can be bonded to the cleaned custom PMMA planar lens and then sterilized prior to the next session.

The image-forming ERG also has issues concerning the parylene C electrode and the rigid clear contact lens bonding. Since parylene C is not easily bonded with other polymer unless high temperature (200 degree celsius) and high pressure are applied. With the high pressure applied, the neck of the electrode array where the electrode exits the contact lens may experience excessive pressure that could stretch the parylene C layers, resulting in possible broken connecting traces. This problem could be minimized by modifying the PDMS molds such that the thin line near neck of the electrode is not sandwiched by the mold and the sharp contact lens edge. Even with the high pressure and high temperature, the adhesion seems to

deteriorate after a few alcohol soaking sessions. To enhance the adhesion, plasma treatment could be done before bonding.

Moreover, the transparent conducting material, such as PEDOT:PSS and ITO can be deposited for electrode sites and traces. Transparent conductive polymers, especially PEDOT:PSS, have gained interest in the optical device community because of thier high conductivity and low electrical impedance. The visual acuity of the proposed image-forming lens can be greatly improved with the transparent metal traces.

New ERG designs

The image-forming ERG lens has shown reasonable ERG recording ability but for better visual acuity during wearing the ERG lens a modified design can be useful. This modified design should have all of the electrode sites outside of the pupil or even on the scleral area to avoid the visual obstruction. The other possibility is to have the electrode sites on both cornea and sclera. Through the use of transparent electrode sites and interconnecting traces using transparent conductive materials such as PEDOT:PSS and ITO, the visual acuity can be improved. The new ERG lens with electrode channels arranged outside the pupil area can be fabricated simply by removing the two or three inner most rings of electrode site array. Similar fabricating and assembled process can be applied for this case. A potential method is to design an electrode with the sites arranged in one ring on the scleral area as shown in Figure 7.3. Limitation of this design is the electrode-lens bonding difficulty, as it may be challenging to align and keep the electrode ring in the right position.

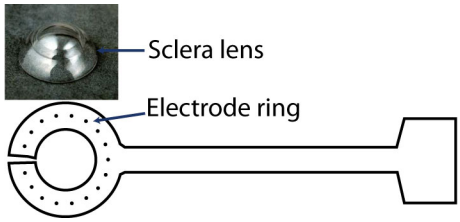

Figure 7.3: A scleral lens from Danker Labs and a proposed scleral lens based on the developed ERG designs.

7.3 Conclusions

Neural Engineering has gained a lot of interest and expanded rapidly in the past few years. The work acquired from this study has contributed to neural engineering field particularly in the neural interface device for Brain-Computer interface and electroretinography application through the use of flexible thin-film technology. The prototyped micro-ECoG devices have shown good mechanical, electrical, recorded signal quality and minimal biological response after long-term implantation in both rats and monkeys. These results have lead to further investigation in micro-ECoG electrode capability for controlling the virtual robotic arms, or eventually the neuro-prosthesis in monkeys. The results also expanded micro-ECoG outside the BCI application with newly emerged optogenetic toolboxes. By combining optogenetics and cranial window imaging, we have also created a minimally invasive two-way neural interface in which micro-ECoG can record the activated neuron signals in response to photostimulation in transgenic animal model. This combination also enables a new way to characterize and optimize the electrode spatial and temporal resolution, which are parameters

of significant importance for BCI application. Furthermore, an integrated optogenetic micro-ECoG array has set the direction toward two-way neural interface in awake animals which could be valuable for BCI, neuroprothesis, and basic neuroscience studies. In addition to BCI application, the development of ERG devices has demonstrated new avenues for the flexible thin-film electronic fabrication developed here. High density electrode array could potentially lead to image forming retinal mapping for multiple retinal related diseases. Ultimately, the work presented here may bring micro-ECoG for BCI applications and multi-electrode array for ERG applications closer to clinical trials and the patients.

A.1 General Information

The polyimide electrode arrays were fabricated by using photodefinable polyimide, photolithography, metal evaporation and lift off, and oxygen plasma. The resulting polyimide electrode arrays are 25 microns thick with metal electrode sites and traces sandwiched between the two polyimide layers.

A.2 Materials

- 4" Si wafers
- Polyimide (HD-4110, HD MicroSystems)
- Developer (PA-401D, HD MicroSystems)
- Rinser (PA-400R, HD MicroSystems)
- Acetone
- Isopropyl Alcohol (IPA)
- Gold (99.99%) for metal evaporation
- Platinum (99.99%) for metal evaporation
- Chromium (99.99%) for metal evaporation
- Aluminum (99.99%) for sacrificial layer

- Photoresist S1813 (Shipley)
- MIF-321 developer (MicroChemicals)
- Sodium Chloride solution, 2M
- DI water
- Platinum wire (0.5 mm in diameter)
- Cleanroom wipes (TexWipes)
- Polyimide adhesive sheet (Pyralux ® LF Coverlay, Bondply & Sheet Adhesive, Dupont)

A.3 Fabrication Protocols

1. Clean the 4" Si wafers with Acetone and IPA and dry with nitrogen gun.

2. Deposit 200 nm of Aluminum layer with the metal evaporator or sputterer.

3. Spin coat the first layer of polyimide film (HD 4110, HD MicroSystems) with the following spin steps.

- 500 rpm 5 second with 500 rpm/second ramp
- 2500 rpm 30 second with 3000 rpm/second ramp

4. Bake the coated wafer at 85, 95 and 105 °C for 90 seconds in each step on the hot plate.

5. Wait for 2 minutes and use transparency mask and the Mask Aligner (MA6/BA6 Karl Suss) to expose 40 seconds with i-line UV light (365 nm wavelength), hard contact.

6. Develop the exposed polyimide layer in a petri dish contains 100 ml of PA-401D developer for 2.5 minutes.

7. Immerse the wafer in the 1:1 PA-401D and PA-400R solution for 1 minute.

8. Rinse the wafer in PA-400R rinser for 30 seconds.

9. Blow dry with nitrogen gun.

10. Cure the polyimide coated wafer in nitrogen atmosphere vacuum oven (4-5 Torrs of nitrogen atmosphere) for approximately 5 hours (200 °C for 50 minutes, 300 °C for 120 minutes (allow 20 minutes of ramping up time) and ramp down to 20°C in 90 minutes).

11. Spin S1813 at 4000 rpm for 30 seconds.

12. Bake the coated wafer on the hot plate at 115 °C for 1 minute.

13. Expose the wafer for 18 seconds with i-line UV light (365 nm wavelength), vacuum hard contact.

14. Develop the wafer with MIF-321 developer for 1 minute, rinse with DI water for 1 minute and then blow dry with nitrogen gun.

15. Evaporate 10 nm of Chromium, 200 nm of Gold and 20 nm of Platinum layers on the wafer with CHA-600 E-beam Evaporator.

16. Soak in acetone and sonicate for 5-10 minutes for lift-off the undesired metal areas.

17. Repeat steps 3 - 10 for the second layer of polyimide

18. Clean the residue of polyimide film on the electrode sites by using oxygen plasma (Unaxis 790) at 250 W, 10mTorr for 2 minutes

19. Dissolve the sacrificial metal layer to release the polyimide electrode array from the Si wafer by applying 0.8 DC voltage to the aluminum layer with Pt wire as counter electrode until the electrode arrays are completely released (approximately 3-5 hours).

20. Clean and soak the polyimide electrode array in DI water for 2-3 hours to get rid of the sodium chloride residues.

21. Dry the electrode arrays by placing between the cleanroom wipes.

22. Cut out the polyimide adhesive sheet (175 microns thick) to fit the contact pad area with Cutting-plotter (Craft Robo Pro).

23. Align the polyimide adhesive sheet on the contact pad area between two aluminum foil wrapped transparency sheet and apply 230-250 kPa of pressure on the hot plate at 180 °C for 1.5 hours.

B.1 General Information

Through the use of chemical vapor deposition, metal evaporation, photolithography and lift-off process, and dry oxygen plasma etching process, parylene C electrode arrays were fabricated using Si wafer as carrier substrate. The resulting 25 μm thick parylene C electrode arrays have Cr/Au/Pt electrode sites and traces sandwiched between the two parylene C layers. This appendix describes the required materials and detail fabrication protocols for all of the parylene C electrode array used in this thesis.

B.2 Materials

- 4" Si wafers
- Parylene C dimers (SCS DPX-C dichloro-di-para-xylylene, Special Coating Systems)
- AZ P4620 photoresist (AZ Electronic MAterials)
- Developer AZ-400K (non dilution), MicroChemicals
- Acetone
- Isopropyl Alcohol (IPA)
- Gold (99.99%) for metal evaporation
- Platinum (99.99%) for metal evaporation

- Chromium (99.99%) for metal evaporation
- Aluminum (99.99%) for sacrificial layer
- Photoresist S1813 (Shipley)
- MIF-321 developer (MicroChemicals)
- DI water
- Polyimide adhesive sheet (Pyralux ® LF Coverlay, Bondply & Sheet Adhesive 175 microns thick, Dupont)

B.3 Fabrication Protocols

1. Clean the 4" Si wafers with Acetone and IPA and dry with nitrogen gun.
2. Deposit the first layer of 15 μm of parylene C layer with SCS PDS 2010 Labcoater ® using 25 grams of parylene C dimers.
3. Spin thin layer of positive photoresist S1813 at 4000 rpm for 30 seconds for metal lift-off process.
4. Bake the S1813 photoresist coated wafer on the hot plate at 115 °C for 1 minute.
5. Expose the wafer for 12 seconds with i-line UV light (365 nm wavelength), vacuum hard contact.
6. Develop the wafer with MIF-321 developer for 1 minute and rinse with DI water for 1 minute and then blow dry with nitrogen gun.

7. Evaporate 10 nm of Chromium, 200 nm of Gold and 20 nm of Platinum layers on the patterned wafer for electrode sites and interconnections with CHA-600 E-beam Evaporator.

8. Soak in acetone and sonicate for 5-10 minutes for lift-off the undesired metal areas.

9. Deposit the second layer of parylene C (10 μm) using 16.7 grams of parylene C dimers.

10. Clean wafers with acetone and IPA on the spinner.

11. Spin coat AZ 4620 photoresist at 2000 rpm for 30 seconds and bake at 110 °C for 190 seconds on the hot plate.

12. Repeat AZ 4620 coating for second layer of photoresist and bake for 190 seconds to achieve photomask of approximately 24 μm for oxygen plasma etching process. After each baking step, the wafer has to be cooled down slowly by picking the wafer 10 cm above the hot plate and cool down for 2 minutes to avoid the photoresist cracking.

13. Use transparency mask on soda lime glass panel that protects all the electrode layout areas on the Mask Aligner (MA6/BA6 Karl Suss) to expose 180 seconds with i-line UV light (365 nm wavelength), vacuum hard contact.

14. Develop the AZ 4620 layer with AZ-400K with 1: 2 ratio solution of developer: DI water for 3 minutes or until the photoresist is fully developed.

15. Rinse with DI water for 1 minute and dry with nitrogen gun.

16. Wait for 3-4 minutes before baking the wafer on the hot plate at 110 °C for 190 seconds to avoid photoresist cracking.

17. Etch 15 μm of parylene C layer for 53 minutes using oxygen plasma etching process (RIE Unaxis 790) with 80 sccm O2, 150 mTorr and 200W.

18. Remove the AZ 4620 photomask by soaking in acetone and rinse out with acetone and IPA.

19. Repeat step 11- 12

20. Expose the AZ 4620 layers using a transparency mask that has electrode sites, contact pad and area outside the electrode layout unprotected for 180 seconds with Karl Suss MA6/BA6 mask aligner, i-line UV light (365 nm wavelength), vacuum hard contact.

21. Repeat step 14-16

22. Etch 10 μm of parylene C layer using the same oxygen plasma conditions as in step 17 for 43 minutes.

23. Remove the AZ 4620 photomask by soaking in acetone and rinse out with acetone and IPA.

24. Soak and rinse the wafer in DI water for 1 hour.

25. Release the parylene C electrode devices by picking the corner of each device with sharp pointy tweezers. The device will lift off from Si wafer once the water can get under small area of the device.

26. Dry the electrode arrays by placing between the cleanroom wipes.

27. Cut out the polyimide adhesive sheet (175 microns thick) to fit the contact pad area with Cutting-plotter (Craft Robo Pro).

28. Align the polyimide adhesive sheet on the contact pad area between two aluminum foil wrapped transparency sheet and apply 230-250 kPa of pressure on the hot plate at 180 °C for 1.5 hours.

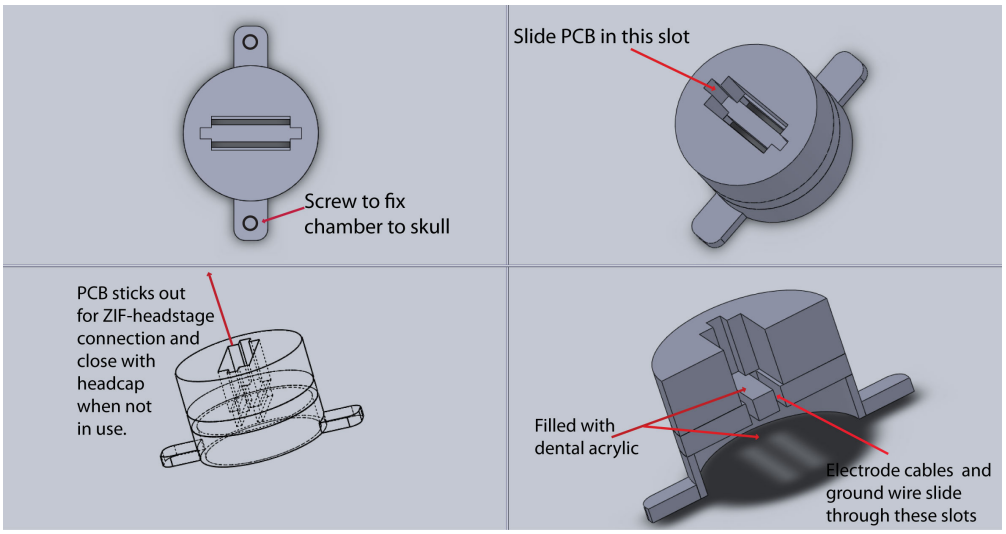

Figure C.1: A detail 3D design of a head chamber showing its features. (These 3D design is a working in collaboration with Jordan Williams, Washington University in St. Louis, St. Louis, MO)

Primary Antibodies	Dilution	Secondary Antibodies	Abs/Em (nm)	Dilution
GFAP (Sigma-Aldrich)	1:500	Alexaflour488 (A-11008, Invitrogen)	495/519	1:200
IBA-1(Wako)	1:800	Alexaflour568 (A-11036, Invitrogen)	578/603	1:200
GFAP (MAB360, Millipore)	1:500	Alexaflour488 (A-11008, Invitrogen)	495/519	1:200

Table D.1: Table of Immunohistochemical Antibodies

D.1 Materials

The materials required for immunohistochemical staining of the rat and monkey brain tissue slices are listed as below.

- Hank balance salt solution (H8264, Sigma-Aldrich)
- HEPES (H3375, Sigma-Aldrich)
- Sodium Azide (8032, Sigma-Aldrich)
- Phosphate Buffered Saline (1X solution, Fisher Scientific)
- Sodium Borohydride (NaBH4 452882, Sigma-Aldrich)
- Triton X100 (X100, Sigma-Aldrich)
- Tween 20 (P1379, Fisher Scienctific)

- Brovine Serum Albumin (BSA A9647, Sigma-Aldrich)
- GFAP (MAB360, Millipore)
- GFAP (anti-rabbit G3893, Sigma-Aldrich)
- IBA-1 (Wako)
- AlexaFluor568 anti-rabbit (A-11036, Invitrogen)
- AlexaFluor488 anti-mouse (A-11029, Invotrogen)
- Prolong Gold mounting solution (P36930, Invitrogen)
- Clear Nail polish

D.2 Procedures

Day 1:

1. Prepare 5.9575g/L of HEPES Buffered Hank Saline solution (HBHS)
2. Mix Sodium Azide (90mg/L) in HBHS solution (HBHS with Sodium Azide)
3. Wash 3X in HBHS with Sodium Azide solution, rapid rinse
4. Incubate in 5 mg/ml Sodium Borohydride in HBHS for 30 minutes
5. Wash 3X in HBHS with Sodium Azide solution, rapid rinse
6. Incubate in 1% Triton X-100 in HBHS with Sodium Azide for 30 minutes
7. Wash 3X in HBHS with Sodium Azide solution, rapid rinse

8. Incubate in 5 % BSA in HBHS overnight

Day 2:

1. Wash 4X in HBHS with Sodium Azide solution, 30 minutes between each wash
2. Incubate overnight with primary antibodies in HBHS with Sodium Azide

Day 3:

1. Wash 4X in HBHS with Sodium Azide and 0.5 % by weight of Tween solution, 30 mins. between each wash
2. Incubate in the dark atmosphere overnight with secondary antibodies in HBHS with Sodium Azide

Day 4:

1. Wash 4X in HBHS with Sodium Azide and 0.5 % by weight of Tween solution, 30 minutes between each wash
2. Change buffer to HBHS with Sodium Azide
3. Mount the samples with Prolong Gold mounting solution and cover with coverslip
4. Let the samples set overnight in a dark atmosphere
5. Seal slide with nail polish

Adamantidis, Antoine R, Feng Zhang, Alexander M Aravanis, Karl Deisseroth, and Luis de Lecea. 2007. Neural substrates of awakening probed with optogenetic control of hypocretin neurons. *Nature* 450(7168):420–4.

Agnew, W F, T G Yuen, D B McCreery, and L A Bullara. 1986. Histopathologic evaluation of prolonged intracortical electrical stimulation. *Exp Neurol* 92(1):162–85.

Allison, Brendan Z, Dennis J McFarland, Gerwin Schalk, Shi Dong Zheng, Melody Moore Jackson, and Jonathan R Wolpaw. 2008. Towards an independent brain-computer interface using steady state visual evoked potentials. *Clin Neurophysiol* 119(2):399–408.

Aravanis, Alexander M, Li-Ping Wang, Feng Zhang, Leslie A Meltzer, Murtaza Z Mogri, M Bret Schneider, and Karl Deisseroth. 2007. An optical neural interface: in vivo control of rodent motor cortex with integrated fiberoptic and optogenetic technology. *J Neural Eng* 4(3):S143–56.

Arden, G B, R M Carter, C Hogg, I M Siegel, and S Margolis. 1979. A gold foil electrode: extending the horizons for clinical electroretinography. *Invest Ophthalmol Vis Sci* 18(4):421–6.

Arenkiel, Benjamin R, Joao Peca, Ian G Davison, Catia Feliciano, Karl Deisseroth, George J Augustine, Michael D Ehlers, and Guoping Feng. 2007. In vivo light-induced activation of neural circuitry in transgenic mice expressing channelrhodopsin-2. *Neuron* 54(2):205–18.

Armington, J C. 1974. *The electroretinogram*. New York: Academic Press.

Bairati, A, Jr, and N Orzalesi. 1963. The ultrastructure of the pigment epithelium and of the photoreceptor-pigment epithelium junction in the human retina. *J Ultrastruct Res* 41:484–96.

Baker, S N, N Philbin, R Spinks, E M Pinches, D M Wolpert, D G MacManus, Q Pauluis, and R N Lemon. 1999. Multiple single unit recording in the cortex of monkeys using independently moveable microelectrodes. *J Neurosci Methods* 94(1):5–17.

Betelak, K F, E A Margiotti, M E Wohlford, and D A Suzuki. 2001. The use of titanium implants and prosthodontic techniques in the preparation of

non-human primates for long-term neuronal recording studies. *J Neurosci Methods* 112(1):9–20.

Blanco, Justin A, Matt Stead, Abba Krieger, Jonathan Viventi, W Richard Marsh, Kendall H Lee, Gregory A Worrell, and Brian Litt. 2010. Unsupervised classification of high-frequency oscillations in human neocortical epilepsy and control patients. *J Neurophysiol* 104(5):2900–12.

Blum, N A, B G Carkhuff, H K Charles, Jr, R L Edwards, and R A Meyer. 1991. Multisite microprobes for neural recordings. *IEEE Trans Biomed Eng* 38(1):68–74.

Bowmaker, J K, and H J Dartnall. 1980. Visual pigments of rods and cones in a human retina. *J Physiol* 298:501–11.

Boyden, Edward S, Feng Zhang, Ernst Bamberg, Georg Nagel, and Karl Deisseroth. 2005. Millisecond-timescale, genetically targeted optical control of neural activity. *Nat Neurosci* 8(9):1263–8.

Brown, K T, and M Murakami. 1964. A new receptor potential of the monkey retina with no detectable latency. *Nature* 201:626–8.

Brunner, Peter, Anthony L Ritaccio, Joseph F Emrich, Horst Bischof, and Gerwin Schalk. 2011. Rapid communication with a "p300" matrix speller using electrocorticographic signals (ecog). *Front Neurosci* 5:5.

C J Mitchell, J J Senkevich, G R Yang. 2006. Adhesion aspects of gamma-methacryloxypropyltrimethoxysilane to poly(p-xylylene). *Journal Adhesion Science Technology* 20(14):1637–1647.

Chang, Tracy Y, Vikramaditya G Yadav, Sarah De Leo, Agustin Mohedas, Bimal Rajalingam, Chia-Ling Chen, Selvapraba Selvarasah, Mehmet R Dokmeci, and Ali Khademhosseini. 2007. Cell and protein compatibility of parylene-c surfaces. *Langmuir* 23(23):11718–25.

Curcio, C A, and K A Allen. 1990. Topography of ganglion cells in human retina. *J Comp Neurol* 300(1):5–25.

Curcio, C A, K R Sloan, R E Kalina, and A E Hendrickson. 1990. Human photoreceptor topography. *J Comp Neurol* 292(4):497–523.

Deisseroth, Karl, Guoping Feng, Ania K Majewska, Gero Miesenböck, Alice Ting, and Mark J Schnitzer. 2006. Next-generation optical technologies for illuminating genetically targeted brain circuits. *J Neurosci* 26(41):10380–6.

Ding, L, F E. Karasz, Y Lin, Y Pang, and L Liao. 2003. Photoluminescence and electroluminescence study of violet-blue and green emitting polymers and their blend. *Macromolecules* 36:7301–7307.

Drury, C. J., C. M. J. Mutsaers, C. M. Hart, M. Matters, and D. M. de Leeuw. 1998. Low-cost all-polymer integrated circuits. *Appl Phys Lett* 73(1):108–110.

Ebrey, T, and Y Koutalos. 2001. Vertebrate photoreceptors. *Prog Retin Eye Res* 20(1):49–94.

Edwards, Erik, Srikantan S Nagarajan, Sarang S Dalal, Ryan T Canolty, Heidi E Kirsch, Nicholas M Barbaro, and Robert T Knight. 2010. Spatiotemporal imaging of cortical activation during verb generation and picture naming. *Neuroimage* 50(1):291–301.

Felton, E A, R G Radwin, J A Wilson, and J C Williams. 2009. Evaluation of a modified fitts law brain-computer interface target acquisition task in able and motor disabled individuals. *J Neural Eng* 6(5):056002.

Felton, Elizabeth A, J Adam Wilson, Justin C Williams, and P Charles Garell. 2007. Electrocorticographically controlled brain-computer interfaces using motor and sensory imagery in patients with temporary subdural electrode implants. report of four cases. *J Neurosurg* 106(3):495–500.

Forbes, HENRY S., and HAROLD G. Wolff. 1928. Cerebral circulation iii. the vasomotor control of cerebral vessels. *Arch Neurol Psychiatry* 19(6): 1057–1086.

Francois, J, and A D Rouck. 1976. Electroretinographical study of the hypoplasia of the optic nerve. *Ophthalmologica* 172(4):308–30.

Frontczak-Baniewicz, M, and M Walski. 2006. Glial scar instability after brain injury. *J Physiol Pharmacol* 57 Suppl 4:97–102.

de Gans, Berend-Jan, Stephanie Hoeppenerand, and Ulrich S. Schubert. 2006. Polymer-relief microstructures by inkjet etching. *Advanced Materials* 18:910–914.

Gehlbach, P L, and R L Purple. 1993. An electrical artifact associated with the erg-jet gold foil electrode. *Invest Ophthalmol Vis Sci* 34(8):2596–9.

Gouras, P. 1984. Progress in human visual evoked responses. *J Clin Neurophysiol* 1(1):77–82.

Gradinaru, Viviana, Kimberly R Thompson, Feng Zhang, Murtaza Mogri, Kenneth Kay, M Bret Schneider, and Karl Deisseroth. 2007. Targeting and readout strategies for fast optical neural control in vitro and in vivo. *J Neurosci* 27(52):14231–8.

Grand, László, Lucia Wittner, Stanislav Herwik, Emmanuelle Göthelid, Patrick Ruther, Sven Oscarsson, Hercules Neves, Balázs Dombovári, Richárd Csercsa, György Karmos, and István Ulbert. 2010. Short and long term biocompatibility of neuroprobes silicon probes. *J Neurosci Methods* 189(2): 216–29.

Guillaume, A, D Osmont, D Gaffie, J C Sarron, and P Quandieu. 1997. Effects of perfusion on the mechanical behavior of the brain-exposed to hypergravity. *J Biomech* 30(4):383–9.

Gunaydin, Lisa A, Ofer Yizhar, André Berndt, Vikaas S Sohal, Karl Deisseroth, and Peter Hegemann. 2010. Ultrafast optogenetic control. *Nat Neurosci* 13(3):387–92.

Hassler, Christina, Rene P von Metzen, Patrick Ruther, and Thomas Stieglitz. 2010. Characterization of parylene c as an encapsulation material for implanted neural prostheses. *J Biomed Mater Res B Appl Biomater* 93(1): 266–74.

Hee, Michael R, Joseph A Izatt, Eric A Swanson, David Huang, Joel S Schuman, Charles P Lin, Carmen A Puliafito, and James G Fujimoto. 1995. Optical coherence tomography of the human retina. *Arch Opthalmol* 113: 325–332.

Henle, C, M Raab, J G Cordeiro, S Doostkam, A Schulze-Bonhage, T Stieglitz, and J Rickert. 2011. First long term in vivo study on subdurally implanted micro-ecog electrodes, manufactured with a novel laser technology. *Biomed Microdevices* 13(1):59–68.

Hennig, A, K-J Eichhorn, U Staudinger, K Sahre, M Rogalli, M Stamm, A W Neumann, and K Grundke. 2004. Contact angle hysteresis: study by dynamic cycling contact angle measurements and variable angle spectroscopic ellipsometry on polyimide. *Langmuir* 20(16):6685–91.

Hinds, B K, J McCartney, and G Woods. 1991. Pattern development for 3d surfaces. *Computer-Aided Design* 23(8):583–592.

Hollenberg, Brian A, Cecilia D Richards, Robert Richards, David F Bahr, and David M Rector. 2006. A mems fabricated flexible electrode array for recording surface field potentials. *J Neurosci Methods* 153(1):147–53.

Hood, D C, and M A Finkelstein. 1979. Comparison of changes in sensitivity and sensation: implications for the response-intensity function of the human photopic system. *J Exp Psychol Hum Percept Perform* 5(3):391–405.

Hsu, J M, L Rieth, R A Normann, P Tathireddy, and F Solzbacher. 2009. Encapsulation of an integrated neural interface device with parylene c. *IEEE Trans Biomed Eng* 56(1):23–9.

Hu, Xiaolong, Peter Krull, Bassel de Graff, Kevin Dowling, John A Rogers, and William J Arora. 2011. Stretchable inorganic-semiconductor electronic systems. *Adv Mater* 23(26):2933–6.

Iida, Koji, Hiroshi Otsubo, Kazunori Arita, Frederick Andermann, and Andre Olivier. 2005. Cortical resection with electrocorticography for intractable porencephaly-related partial epilepsy. *Epilepsia* 46(1):76–83.

Ito, D, Y Imai, K Ohsawa, K Nakajima, Y Fukuuchi, and S Kohsaka. 1998. Microglia-specific localisation of a novel calcium binding protein, iba1. *Brain Res Mol Brain Res* 57(1):1–9.

Jackson, Andrew, Chet T Moritz, Jaideep Mavoori, Timothy H Lucas, and Eberhard E Fetz. 2006. The neurochip bci: towards a neural prosthesis for upper limb function. *IEEE Trans Neural Syst Rehabil Eng* 14(2):187–90.

Jasper, H H, and J Kershman. 1946. Electroencephalography. *Prog Neurol Psychiatry* 1:372–97.

Jin, Hui, Chen Tao, Marappan Velusamy, Muhsen Aljada, Yuliang Zhang, Mike Hambsch, Paul L Burn, and Paul Meredith. 2012. Efficient, large area ito-and-pedot-free organic solar cell sub-modules. *Adv Mater* 24(19):2572–7.

Jung, Inhwa, Jianliang Xiao, Viktor Malyarchuk, Chaofeng Lu, Ming Li, Zhuangjian Liu, Jongseung Yoon, Yonggang Huang, and John A Rogers. 2011. Dynamically tunable hemispherical electronic eye camera system with adjustable zoom capability. *Proc Natl Acad Sci U S A* 108(5):1788–93.

Kamińska, Marta, Wiesława Okrój, Witold Szymański, Witold Jakubowski, Piotr Komorowski, Andrzej Nosal, Hieronim Szymanowski, Maciej Gazicki-Lipman, Hanna Jerczyńska, Zofia Pawłowska, and Bogdan Walkowiak. 2009.

Interaction of parylene c with biological objects. *Acta Bioeng Biomech* 11(3): 19–25.

Kaplan, J, D Bonneau, J Frézal, A Munnich, and J L Dufier. 1990. Clinical and genetic heterogeneity in retinitis pigmentosa. *Hum Genet* 85(6):635–42.

Kellis, Spencer, Kai Miller, Kyle Thomson, Richard Brown, Paul House, and Bradley Greger. 2010. Decoding spoken words using local field potentials recorded from the cortical surface. *J Neural Eng* 7(5):056007.

Kellis, Spencer S, Paul A House, Kyle E Thomson, Richard Brown, and Bradley Greger. 2009. Human neocortical electrical activity recorded on non-penetrating microwire arrays: applicability for neuroprostheses. *Neurosurg Focus* 27(1):E9.

Kellner, U, and S Kellner. 2009. [clinical findings and diagnostics of cone dystrophy]. *Ophthalmologe* 106(2):99–108.

Kim, Dae-Hyeong, Jonathan Viventi, Jason J Amsden, Jianliang Xiao, Leif Vigeland, Yun-Soung Kim, Justin A Blanco, Bruce Panilaitis, Eric S Frechette, Diego Contreras, David L Kaplan, Fiorenzo G Omenetto, Yonggang Huang, Keh-Chih Hwang, Mitchell R Zakin, Brian Litt, and John A Rogers. 2010. Dissolvable films of silk fibroin for ultrathin conformal bio-integrated electronics. *Nat Mater* 9(6):511–7.

Kim, H., A. PiqueÂ´, J. S. Horwitz, H. Mattoussi, H. Murata, Z. H. Kafafi, and D. B. Chrisey. 1999. Indium tin oxide thin films for organic light-emitting devices. *Appl Phys Lett* 74(23):3444–3446.

Kim, Jiwan, J Adam Wilson, and Justin C Williams. 2007. A cortical recording platform utilizing microecog electrode arrays. *Conf Proc IEEE Eng Med Biol Soc* 2007:5353–7.

Kipke, Daryl R, Rio J Vetter, Justin C Williams, and Jamille F Hetke. 2003. Silicon-substrate intracortical microelectrode arrays for long-term recording of neuronal spike activity in cerebral cortex. *IEEE Trans Neural Syst Rehabil Eng* 11(2):151–5.

Krusienski, Dean J, and Jerry J Shih. 2011. Control of a visual keyboard using an electrocorticographic brain-computer interface. *Neurorehabil Neural Repair* 25(4):323–31.

Lawwill, T, and H M Burian. 1966. A modification of the burian-allen contact-lens electrode for human electroretinography. *Am J Ophthalmol* 61(6):1506–9.

Ledochowitsch, Peter, Elisa Olivero, Tim Blanche, and Michel M Maharbiz. 2011. A transparent Î¼ecog array for simultaneous recording and optogenetic stimulation. *Conf Proc IEEE Eng Med Biol Soc* 2011:2937–40.

Leuthardt, Eric C, Zac Freudenberg, David Bundy, and Jarod Roland. 2009. Microscale recording from human motor cortex: implications for minimally invasive electrocorticographic brain-computer interfaces. *Neurosurg Focus* 27(1):E10.

Leuthardt, Eric C, Kai Miller, Nicholas R Anderson, Gerwin Schalk, Joshua Dowling, John Miller, Daniel W Moran, and Jeff G Ojemann. 2007. Electrocorticographic frequency alteration mapping: a clinical technique for mapping the motor cortex. *Neurosurgery* 60(4 Suppl 2):260–70; discussion 270–1.

Leuthardt, Eric C, Kai J Miller, Gerwin Schalk, Rajesh P N Rao, and Jeffrey G Ojemann. 2006. Electrocorticography-based brain computer interface–the seattle experience. *IEEE Trans Neural Syst Rehabil Eng* 14(2):194–8.

Leuthardt, Eric C, Gerwin Schalk, Jonathan R Wolpaw, Jeffrey G Ojemann, and Daniel W Moran. 2004. A brain-computer interface using electrocorticographic signals in humans. *J Neural Eng* 1(2):63–71.

Levasseur, J E, E P Wei, A J Raper, A A Kontos, and J L Patterson. 1975. Detailed description of a cranial window technique for acute and chronic experiments. *Stroke* 6(3):308–17.

Lewicki, M S. 1998. A review of methods for spike sorting: the detection and classification of neural action potentials. *Network* 9(4):R53–78.

Li, Wen, Damien C Rodger, Ellis Meng, James D Weiland, Mark S Humayun, and Yu-Chong Tai. 2006. Flexible parylene packaged intraocular coil for retinal prostheses. *Microtechnologies in Medicine and Biology* 2006 International Conference:105–108.

Ling, E A, and W C Wong. 1993. The origin and nature of ramified and amoeboid microglia: a historical review and current concepts. *Glia* 7(1): 9–18.

van Lith, G. 1981. Quantitative evaluation of the electroretinogram. *Ophthalmologica* 182(4):218–23.

López, M. A., J. C. Sánchez, and M. Estrada. 2008. Characterization of pedot:pss dilutions for inkjet printing applied to oled fabrication. *Proceedings of the 7th International Caribbean Conference on Devices,Circuits and Systems, Mexico*.

Ludwig, Kip A, Nicholas B Langhals, Mike D Joseph, Sarah M Richardson-Burns, Jeffrey L Hendricks, and Daryl R Kipke. 2011. Poly(3,4-ethylenedioxythiophene) (pedot) polymer coatings facilitate smaller neural recording electrodes. *J Neural Eng* 8(1):014001.

Luther, Neal, Elayna Rubens, Nitin Sethi, Padmaja Kandula, Douglas R Labar, Cynthia Harden, Kenneth Perrine, Paul J Christos, J Bryan Iorgulescu, Guido Lancman, Neil S Schaul, Dmitriy V Kolesnik, Shahin Nouri, Andrew Dawson, Apostolos J Tsiouris, and Theodore H Schwartz. 2011. The value of intraoperative electrocorticography in surgical decision making for temporal lobe epilepsy with normal mri. *Epilepsia*.

Luttikhuizen, Daniël T, Martin C Harmsen, and Marja J A Van Luyn. 2006. Cellular and molecular dynamics in the foreign body reaction. *Tissue Eng* 12(7):1955–70.

Marmor, M F. 1980. Visual loss in retinitis pigmentosa. *Am J Ophthalmol* 89(5):692–8.

Marmor, M F, A B Fulton, G E Holder, Y Miyake, M Brigell, M Bach, and International Society for Clinical Electrophysiology of Vision. 2009. Iscev standard for full-field clinical electroretinography (2008 update). *Doc Ophthalmol* 118(1):69–77.

Mattis, Joanna, Kay M Tye, Emily A Ferenczi, Charu Ramakrishnan, Daniel J O'Shea, Rohit Prakash, Lisa A Gunaydin, Minsuk Hyun, Lief E Fenno, Viviana Gradinaru, Ofer Yizhar, and Karl Deisseroth. 2012. Principles for applying optogenetic tools derived from direct comparative analysis of microbial opsins. *Nat Methods* 9(2):159–72.

Maynard, E M, C T Nordhausen, and R A Normann. 1997. The utah intracortical electrode array: a recording structure for potential brain-computer interfaces. *Electroencephalogr Clin Neurophysiol* 102(3):228–39.

Miller, Kai J, Marcel denNijs, Pradeep Shenoy, John W Miller, Rajesh P N Rao, and Jeffrey G Ojemann. 2007a. Real-time functional brain mapping using electrocorticography. *Neuroimage* 37(2):504–7.

Miller, Kai J, Eric C Leuthardt, Gerwin Schalk, Rajesh P N Rao, Nicholas R Anderson, Daniel W Moran, John W Miller, and Jeffrey G Ojemann. 2007b. Spectral changes in cortical surface potentials during motor movement. *J Neurosci* 27(9):2424–32.

Miller, Kai J, Pradeep Shenoy, Marcel den Nijs, Larry B Sorensen, Rajesh N Rao, and Jeffrey G Ojemann. 2008. Beyond the gamma band: the role of high-frequency features in movement classification. *IEEE Trans Biomed Eng* 55(5):1634–7.

Mitsubayashi, Kohji, Yoshihiko Wakabayashi, Satoshi Tanimoto, Daisuke Murotomi, and Tatsuro Endo. 2003. Optical-transparent and flexible glucose sensor with ito electrode. *Biosens Bioelectron* 19(1):67–71.

Moiceanu, Claudia, and Benone Cârstocea. 2010. [electroretinography in monitoring of glaucoma (ii)]. *Oftalmologia* 54(4):45–8.

Morii, S, A C Ngai, and H R Winn. 1986. Reactivity of rat pial arterioles and venules to adenosine and carbon dioxide: with detailed description of the closed cranial window technique in rats. *J Cereb Blood Flow Metab* 6(1): 34–41.

Mostany, Ricardo, and Carlos Portera-Cailliau. 2008. A craniotomy surgery procedure for chronic brain imaging. *J Vis Exp* (12).

Mountcastle, V B. 1997. The columnar organization of the neocortex. *Brain* 120 (Pt 4):701–22.

Nagel, Georg, Martin Brauner, Jana F Liewald, Nona Adeishvili, Ernst Bamberg, and Alexander Gottschalk. 2005. Light activation of channelrhodopsin-2 in excitable cells of caenorhabditis elegans triggers rapid behavioral responses. *Curr Biol* 15(24):2279–84.

Nenadic, Zoran, and Joel W Burdick. 2005. Spike detection using the continuous wavelet transform. *IEEE Trans Biomed Eng* 52(1):74–87.

Nicholls, John G, A Robert Martin, Bruce G Wallace, and Pual A Fuchs. 2001. *From neuron to brain*. 4th ed. Sunderland, MA, USA: Sinauer Associates, Inc.

Nilsson, S E. 1971. Human retinal vascular obstructions. a quantitative correlation of angiographic and electroretinographic findings. *Acta Ophthalmol (Copenh)* 49(1):111–33.

Noell, W K. 1954. The origin of the electroretinogram. *Am J Ophthalmol* 38(1:2):78–90.

Ohara, S, A Ikeda, T Kunieda, S Yazawa, K Baba, T Nagamine, W Taki, N Hashimoto, T Mihara, and H Shibasaki. 2000. Movement-related change of electrocorticographic activity in human supplementary motor area proper. *Brain* 123 (Pt 6):1203–15.

Ouyang, Liangqi, Rylie Green, Kathleen E Feldman, and David C Martin. 2011. Direct local polymerization of poly(3,4-ethylenedioxythiophene) in rat cortex. *Prog Brain Res* 194:263–71.

Pan, Weihong, Hung Hsuchou, Changlei Xu, Xiaojun Wu, Sebastien G Bouret, and Abba J Kastin. 2011. Astrocytes modulate distribution and neuronal signaling of leptin in the hypothalamus of obese a vy mice. *J Mol Neurosci* 43(3):478–84.

Panagiotides, Heracles, Walter J Freeman, Mark D Holmes, and Dimitrios Pantazis. 2011. Behavioral states may be associated with distinct spatial patterns in electrocorticogram. *Cogn Neurodyn* 5(1):55–66.

Pangeni, Gobinda, Robert Lämmer, Ralf P Tornow, Folkert K Horn, and Jan Kremers. 2012. On- and off-response ergs elicited by sawtooth stimuli in normal subjects and glaucoma patients. *Doc Ophthalmol*.

Pei, Xiaomei, Eric C Leuthardt, Charles M Gaona, Peter Brunner, Jonathan R Wolpaw, and Gerwin Schalk. 2011. Spatiotemporal dynamics of electrocorticographic high gamma activity during overt and covert word repetition. *Neuroimage* 54(4):2960–72.

Pellinen, D, T Moon, R Vetter, R Miriani, and D Kipke. 2005. Multifunctional flexible parylene-based intracortical microelectrodes. *Conf Proc IEEE Eng Med Biol Soc* 5:5272–5.

Pepperberg, D R, and R H Masland. 1978. Retinal-induced sensitization of light-adapted rabbit photoreceptors. *Brain Res* 151(1):194–200.

Pistohl, Tobias, Tonio Ball, Andreas Schulze-Bonhage, Ad Aertsen, and Carsten Mehring. 2008. Prediction of arm movement trajectories from ecog-recordings in humans. *J Neurosci Methods* 167(1):105–14.

Polikov, Vadim S, Patrick A Tresco, and William M Reichert. 2005. Response of brain tissue to chronically implanted neural electrodes. *J Neurosci Methods* 148(1):1–18.

Poloschek, C M, and M Bach. 2012. [electrophysiological examination methods in glaucoma diagnostics]. *Ophthalmologe* 109(4):358–63.

Pruett, R C. 1983. Retinitis pigmentosa: clinical observations and correlations. *Trans Am Ophthalmol Soc* 81:693–735.

Quiroga, R Quian, Z Nadasdy, and Y Ben-Shaul. 2004. Unsupervised spike detection and sorting with wavelets and superparamagnetic clustering. *Neural Comput* 16(8):1661–87.

Reboud, Vincent, Ali Z Khokhar, Borja Sepúlveda, Damian Dudek, Tim Kehoe, John Cuffe, Nikolaos Kehagias, Mónica Lira-Cantu, Nikolaj Gadegaard, Valentina Grasso, Vito Lambertini, and Clivia M Sotomayor Torres. 2012. Enhanced light extraction in ito-free oleds using double-sided printed electrodes. *Nanoscale* 4(11):3495–500.

Richardson, R R, Jr, J A Miller, and W M Reichert. 1993. Polyimides as biomaterials: preliminary biocompatibility testing. *Biomaterials* 14(8):627–35.

del Rio-Hortega, P. 1932. *Microglia. in cytology and cellular pathology of the nervous system*, vol. 2. Harper (Hoeber), New York: W. Penfield.

Rousche, P J, and R A Normann. 1998. Chronic recording capability of the utah intracortical electrode array in cat sensory cortex. *J Neurosci Methods* 82(1):1–15.

Rousche, P J, D S Pellinen, D P Pivin, Jr, J C Williams, R J Vetter, and D R Kipke. 2001. Flexible polyimide-based intracortical electrode arrays with bioactive capability. *IEEE Trans Biomed Eng* 48(3):361–71.

Rubehn, Birthe, Conrado Bosman, Robert Oostenveld, Pascal Fries, and Thomas Stieglitz. 2009. A mems-based flexible multichannel ecog-electrode array. *J Neural Eng* 6(3):036003.

Rubehn, Birthe, and Thomas Stieglitz. 2010. In vitro evaluation of the long-term stability of polyimide as a material for neural implants. *Biomaterials* 31(13):3449–58.

Sanchez, Justin C, Aysegul Gunduz, Paul R Carney, and Jose C Principe. 2008. Extraction and localization of mesoscopic motor control signals for human ecog neuroprosthetics. *J Neurosci Methods* 167(1):63–81.

Schalk, G, J R Wolpaw, D J McFarland, and G Pfurtscheller. 2000. Eeg-based communication: presence of an error potential. *Clin Neurophysiol* 111(12): 2138–44.

Schalk, Gerwin, Dennis J McFarland, Thilo Hinterberger, Niels Birbaumer, and Jonathan R Wolpaw. 2004. Bci2000: a general-purpose brain-computer interface (bci) system. *IEEE Trans Biomed Eng* 51(6):1034–43.

Schevon, C A, J Cappell, R Emerson, J Isler, P Grieve, R Goodman, G McKhann, Jr, H Weiner, W Doyle, R Kuzniecky, O Devinsky, and F Gilliam. 2007. Cortical abnormalities in epilepsy revealed by local eeg synchrony. *Neuroimage* 35(1):140–8.

Schmidt, E M, M J Bak, and J S McIntosh. 1976. Long-term chronic recording from cortical neurons. *Exp Neurol* 52(3):496–506.

Schmied, A, C Ivarsson, and E E Fetz. 1993. Short-term synchronization of motor units in human extensor digitorum communis muscle: relation to contractile properties and voluntary control. *Exp Brain Res* 97(1):159–72.

Seymour, John P, and D R Kipke. 2007. Neural probe design for reduced tissue encapsulation in cns. *Biomaterials* 28(25):3594–3607.

Seymour, John P, and Daryl R Kipke. 2006. Fabrication of polymer neural probes with sub-cellular features for reduced tissue encapsulation. *Conf Proc IEEE Eng Med Biol Soc* 1:4606–9.

Sillman, A J, H Ito, and T Tomita. 1969. Studies on the mass receptor potential of the isolated frog retina. i. general properties of the response. *Vision Res* 9(12):1435–42.

Squire, Larry, Darwin Berg, Floyd Bloom, Sascha Du Lac, Anirvan Ghosh, and Nicholas Spitzer. 2008. *Fundamental neuroscience*. 3rd ed. San Diego, California 92101-4495 USA: Academic Press.

Srichan, Cahvis, Thitirat Saikrajang, Tanom Lomas, Apichai Jomphoak, Thitima Maturos, Disayut Phokaratkul, Teerakiat Kerdcharoen, and Adisom Tuantranont. 2009. Inkjet printing pedot:pss using desktop inkjet printer. *IEEE* 978(1).

Stieglitz, T, and J U Meyer. 1999. Implantable microsystems. polyimide-based neuroprostheses for interfacing nerves. *Med Device Technol* 10(6): 28–30.

Stodtmeister, R, L Pillunat, W Gaus, and J Schuster. 1988. [quantitative assessment of the clinical electroretinogram]. *Klin Monbl Augenheilkd* 193(4): 370–81.

Sun, Daniel, Ming Lye-Barthel, Richard H Masland, and Tatjana C Jakobs. 2010. Structural remodeling of fibrous astrocytes after axonal injury. *J Neurosci* 30(42):14008–19.

Takahashi, Hirokazu, Takayuki Ejiri, Masayuki Nakao, Naoya Nakamura, Kimitaka Kaga, and Thierry Hervé. 2003a. Microelectrode array on folding polyimide ribbon for epidural mapping of functional evoked potentials. *IEEE Trans Biomed Eng* 50(4):510–6.

Takahashi, Susumu, Yuichiro Anzai, and Yoshio Sakurai. 2003b. Automatic sorting for multi-neuronal activity recorded with tetrodes in the presence of overlapping spikes. *J Neurophysiol* 89(4):2245–58.

Takeuchi, Shoji, D Ziegler, Y Yoshida, K Mabuchi, and T Suzuki. 2005. Parylene flexible neural probes integrated with microfluidic channels. *Lab Chip* 5(5):519–23.

Tang, L, and J W Eaton. 1993. Fibrin(ogen) mediates acute inflammatory responses to biomaterials. *J Exp Med* 178(6):2147–56.

Terai, N, D Sandner, S Hadjiraftis, and L E Pillunat. 2011. [maculopathy with subretinal yellow deposits.]. *Ophthalmologe*.

Thongpang, Sanitta, Thomas J Richner, Sarah K Brodnick, Amelia Schendel, Jiwan Kim, J Adam Wilson, Joseph Hippensteel, Lisa Krugner-Higby, Dan Moran, Azam S Ahmed, David Neimann, Karl Sillay, and Justin C Williams. 2011. A micro-electrocorticography platform and deployment strategies for chronic bci applications. *Clin EEG Neurosci* 42(4):259–65.

Toda, Haruo, Takafumi Suzuki, Hirohito Sawahata, Kei Majima, Yukiyasu Kamitani, and Isao Hasegawa. 2011. Simultaneous recording of ecog and intracortical neuronal activity using a flexible multichannel electrode-mesh in visual cortex. *Neuroimage* 54(1):203–12.

Touwslager, F J., N P Willard, and D M. de Leeuw. 2002. I-line lithography of poly-3,4-ethylenedioxythiophene electrodes and application in all-polymer integrated circuits. *Appl Phys Lett* 81(24):4556– 558.

Towle, V L, S Cohen, N Alperin, K Hoffmann, P Cogen, J Milton, R Grzesczcuk, C Pelizzari, I Syed, and J P Spire. 1995. Displaying electrocorticographic findings on gyral anatomy. *Electroencephalogr Clin Neurophysiol* 94(4):221–8.

Uhlhaas, Peter J, and Wolf Singer. 2006. Neural synchrony in brain disorders: relevance for cognitive dysfunctions and pathophysiology. *Neuron* 52(1): 155–68.

Usui, Tomoaki, Naoyuki Tanimoto, Satoshi Ueki, Mineo Takagi, Shigeru Hasegawa, Haruki Abe, Keigo Sekiya, and Mitsuru Nakazawa. 2004. Erg rod a-wave in oguchi disease. *Vision Res* 44(5):535–40.

Vaughan, Theresa M, Dennis J McFarland, Gerwin Schalk, William A Sarnacki, Dean J Krusienski, Eric W Sellers, and Jonathan R Wolpaw. 2006. The wadsworth bci research and development program: at home with bci. *IEEE Trans Neural Syst Rehabil Eng* 14(2):229–33.

Viswanathan, S, L J Frishman, J G Robson, and J W Walters. 2001. The photopic negative response of the flash electroretinogram in primary open angle glaucoma. *Invest Ophthalmol Vis Sci* 42(2):514–22.

Viventi, Jonathan, Justin Blanco, and Brian Litt. 2010a. Mining terabytes of submillimeter-resolution ecog datasets for neurophysiologic biomarkers. *Conf Proc IEEE Eng Med Biol Soc* 1:3825–6.

Viventi, Jonathan, Dae-Hyeong Kim, Joshua D Moss, Yun-Soung Kim, Justin A Blanco, Nicholas Annetta, Andrew Hicks, Jianliang Xiao, Yonggang Huang, David J Callans, John A Rogers, and Brian Litt. 2010b. A conformal, bio-interfaced class of silicon electronics for mapping cardiac electrophysiology. *Sci Transl Med* 2(24):24ra22.

Voskuhl, Rhonda R, R Scott Peterson, Bingbing Song, Yan Ao, Laurie Beth J Morales, Seema Tiwari-Woodruff, and Michael V Sofroniew. 2009. Reactive astrocytes form scar-like perivascular barriers to leukocytes during adaptive immune inflammation of the cns. *J Neurosci* 29(37):11511–22.

Whitmore, G A, and F Schenkelberg. 1997. Modelling accelerated degradation data using wiener diffusion with a time scale transformation. *Lifetime Data Anal* 3(1):27–45.

Williams, J C, R L Rennaker, and D R Kipke. 1999. Long-term neural recording characteristics of wire microelectrode arrays implanted in cerebral cortex. *Brain Res Brain Res Protoc* 4(3):303–13.

Williams, Justin C, Joseph A Hippensteel, John Dilgen, William Shain, and Daryl R Kipke. 2007. Complex impedance spectroscopy for monitoring tissue responses to inserted neural implants. *J Neural Eng* 4(4):410–23.

Wilson, Cameron J, Richard E Clegg, David I Leavesley, and Mark J Pearcy. 2005. Mediation of biomaterial-cell interactions by adsorbed proteins: a review. *Tissue Eng* 11(1-2):1–18.

Wilson, J Adam, Elizabeth A Felton, P Charles Garell, Gerwin Schalk, and Justin C Williams. 2006. Ecog factors underlying multimodal control of a brain-computer interface. *IEEE Trans Neural Syst Rehabil Eng* 14(2):246–50.

Wilson, J Adam, Gerwin Schalk, Léo M Walton, and Justin C Williams. 2009. Using an eeg-based brain-computer interface for virtual cursor movement with bci2000. *J Vis Exp* (29).

Wirenfeldt, Martin, Alicia A Babcock, and Harry V Vinters. 2011. Microglia - insights into immune system structure, function, and reactivity in the central nervous system. *Histol Histopathol* 26(4):519–30.

Wolpaw, J R, D J McFarland, G W Neat, and C A Forneris. 1991. An eeg-based brain-computer interface for cursor control. *Electroencephalogr Clin Neurophysiol* 78(3):252–9.

Xu, X, and C Karwoski. 1995. Current source density analysis of the electroretinographic d wave of frog retina. *J Neurophysiol* 73(6):2459–69.

Yanagisawa, Takufumi, Masayuki Hirata, Youichi Saitoh, Amami Kato, Daisuke Shibuya, Yukiyasu Kamitani, and Toshiki Yoshimine. 2009. Neural decoding using gyral and intrasulcal electrocorticograms. *Neuroimage* 45(4): 1099–106.

Yang, Junyan, Dong Hwan Kim, Jeffrey L Hendricks, Michelle Leach, Rebecca Northey, and David C Martin. 2005. Ordered surfactant-templated poly(3,4-ethylenedioxythiophene) (pedot) conducting polymer on microfabricated neural probes. *Acta Biomater* 1(1):125–36.

Yao, Liang, Shanfeng Xue, Qi Wang, Wenyue Dong, Wei Yang, Hongbin Wu, Ming Zhang, Bing Yang, and Yuguang Ma. 2012. Rgb small molecules

based on a bipolar molecular design for highly efficient solution-processed single-layer oleds. *Chemistry* 18(9):2707–14.

Yizhar, Ofer, Lief E Fenno, Thomas J Davidson, Murtaza Mogri, and Karl Deisseroth. 2011. Optogenetics in neural systems. *Neuron* 71(1):9–34.

Yoo, Geonwook, Hojin Lee, Daniela Radtke, Marko Stumpf, Uwe Zeitner, and Jerzy Kanicki. 2009. A maskless laser-write lithography processing of thin-film transistors on a hemispherical surface. *Microelectronic Engineering*.

Zhang, Feng, Li-Ping Wang, Edward S Boyden, and Karl Deisseroth. 2006. Channelrhodopsin-2 and optical control of excitable cells. *Nat Methods* 3(10): 785–92.

Zhao, Shengli, Jonathan T Ting, Hisham E Atallah, Li Qiu, Jie Tan, Bernd Gloss, George J Augustine, Karl Deisseroth, Minmin Luo, Ann M Graybiel, and Guoping Feng. 2011. Cell type–specific channelrhodopsin-2 transgenic mice for optogenetic dissection of neural circuitry function. *Nat Methods* 8(9):745–52.